

HYDROTHERMAL SYNTHESIS & CHARACTERIZATION OF PURE AND DOPED BiVO₄ NANOPARTICLES

A. F. M. MONOWAR HOSSAIN

&

MOHAMMAD ABDULLAH AL MAMUN

Bachelor of Science in Materials and Metallurgical Engineering



Department of Materials and Metallurgical Engineering

Bangladesh University of Engineering and Technology

February, 2017

COPYRIGHT STATEMENTS

Copyright in text of this thesis rests with the author. Copies (by any process) either in full, or of extracts, may be made only in accordance with instructions given by the authors. This page must form part of any such copies made. Further copies (by any process) of copies made in accordance with such instructions may not be made without the permission (in writing) of the authors.

The ownership of any intellectual property rights which may be described in this thesis is vested in the Department of Materials and Metallurgical Engineering of Bangladesh University of Engineering and Technology, subject to any prior agreement to the contrary, and may not be made available for use by third parties without the written permission of the department, which will prescribe the terms and conditions of any such agreement.

The thesis titled “HYDROTHERMAL SYNTHESIS & CHARACTERIZATION OF PURE AND DOPED BiVO₄ NANOPARTICLES” submitted by A. F. M. Monowar Hossain, Student ID 201111045 and Mohammad Abdullah Al Mamun, Student ID 201111046 has been accepted for satisfactory submission in partial fulfillment of the requirement for the degree of Bachelor of Science in Materials and Metallurgical Engineering on 20XX term.

.....
Md. Miftaur Rahman

Assistant Professor

Department of MME

BUET, Dhaka – 1000.

Candidates' Declaration

It is hereby declared that no portion of the work referred to in the thesis has been submitted in support of an application for another degree or qualification of this or any other university or other institute of learning.

.....
A. F. M. Monowar Hossain

Student ID: 201111045

Department of MME

BUET, Dhaka – 1000

.....
Mohammad Abdullah Al Mamun

Student ID: 201111045

Department of MME

BUET, Dhaka – 1000

Acknowledgements

First and foremost, we would like to thank the Almighty for blessing us with the means courage and guidance to carry out this thesis work successfully and in due time.

We express our sincere gratitude to our supervisor, Assistant Prof. Md. Miftaur Rahman for providing us with this research topic in the first place, which we have come to thoroughly enjoy. Without his regular urging, direction and encouragement this research work would have been impossible. We thank him from the bottom of my heart for having faith in us, for motivating us, for providing all kinds of support and for allowing us to freely discuss our thoughts, understandings and ideas regarding the subject without having to give a second thought.

We pay our utmost gratitude to Mehedi Hasan Rizvi, Assistant Prof, Department of Glass and Ceramic Engineering (GCE) for his constant and priceless help with all the technical, theoretical and experimental aspects of this research project. He was the first guidance we would seek whenever any problem had arisen, and in each occasion he would prove to be wonderfully helpful.

We would like to thank Prof. Dr. Md. Fakhrul Islam, Professor and Head, GCE, for his continuous mentoring, guidance, support and encouragement to excel in research and academia, and for allowing us to use the various facilities and raw materials in GCE without hindrance. We also thank Dr. Abdul Hakim, GCE, for showing interest in this research, providing us with motivation and engaging us in thought-provoking discussions.

We profoundly thank Dr. M. A. Basith, Associate Professor, Department of Physics, BUET for letting us use the UV-Vis spectroscopy, giving us permission to use various facilities available and for the support and advice he continues to give us, without which the research work would have become unduly lengthened.

We are supremely grateful to Hasan Muhammad Usama, Lecturer, Department of Materials and Metallurgical Engineering (MME), for supporting the research work, sharing his experience about the topic and its various intricacies, and his immense help regarding the Rietveld analysis of the phase study of this research work.

Finally, we convey our regards to all the staffs and members of GCE, especially Mr. Rana and Mr. Shahjalal for their technical support throughout the endeavor, and to the staffs and members of MME for providing us assistance whenever it was required.

Abstract

Particulate photocatalyst for hydrogen production by water splitting and water purification has received a great attention because of their low cost and applicability in mass scale. Bismuth vanadate (BiVO_4) has recently emerged as one of the most promising photocatalysts for hydrogen production via water splitting and degradation of pollutants. Based on previous studies, it's well established that pure monoclinic (m) - BiVO_4 has showed the best photocatalytic performance so far. In this investigation, pure m- BiVO_4 nanoparticles have been synthesized in a hydrothermal synthesis process: $\text{Bi}(\text{NO}_3)_3 \cdot 5\text{H}_2\text{O}/\text{V}_2\text{O}_5/\text{K}_2\text{SO}_4$, 200 °C. The formation of pure m- BiVO_4 with a slight percentage tetragonal zircon type BiVO_4 phase and no impurity phases (Bi_2O_3) was happened by addition of an inorganic morphology controlling agent (K_2SO_4) and it was later confirmed by Rietveld refinement analysis. The cell parameters of synthesized BiVO_4 with K_2SO_4 ($\text{O}_1 - \text{O}_2 = 3.118 \text{ \AA}^\circ$, $\text{V} - \text{O}_1 = 1.771 \text{ \AA}^\circ$, $\text{V} - \text{O}_2 = 1.693 \text{ \AA}^\circ$, $\text{Bi} - \text{O}_1 = 2.372 \text{ \AA}^\circ$, $\text{Bi} - \text{O}_2 = 2.627 \text{ \AA}^\circ$, $\text{Bi} - \text{O}_1 = 2.518 \text{ \AA}^\circ$, $\text{Bi} - \text{O}_2 = 2.355 \text{ \AA}^\circ$) were perfectly matched with that of pure monoclinic BiVO_4 . $\text{Bi}_{(1-x)}\text{Nd}_x\text{VO}_4$ and $\text{BiMn}_x\text{V}_{(1-x)}\text{O}_4$ (where $x = 0.10$) nanoparticles have been synthesized to investigate the effects of doping on the structural formation, optical bandgap, particle size and morphology of particulate BiVO_4 . Since Nd has larger atomic radius (245 pm) than Bi (230 pm), the addition of Nd doping was supposed to create a lattice distortion; in reality, it rather suppressed the lattice distortion. The reason behind this phenomena was the creation of larger dodecahedral void which contains Bi. It was confirmed that 10% doping of Nd at Bi site was not enough for creating such lattice distortion. The percentage of tetragonal phase was increased due to Nd doping which was an indication that the formation of monoclinic – tetragonal zircon type hetero-structured BiVO_4 might increase with the increase of % Nd doping. Bismuth vanadate with 10% Mn doping at tetrahedral site (replacing V^{5+}) showed very promising result. The strong Mn – O interaction in tetrahedral site creates a stretch between $\text{O}_1 - \text{O}_2$ atoms which are shared by two dodecahedral site in BiVO_4 . Rietveld analysis confirmed the $\text{O}_1 - \text{O}_2$ stretching (3.743 \AA°) in Mn doped sample is larger than that of pure monoclinic BiVO_4 $\text{O}_1 - \text{O}_2$ distance (3.118 \AA°). As expected, for this sample, the band gap was found as the lowest (2.44 eV) in UV – Vis spectrometer analysis.

Table of Contents

COPYRIGHT STATEMENTS	2
Candidates' Declaration	4
Acknowledgements	5
Abstract	6
List of Figures	9
List of Tables.....	12
Chapter 1 Introduction.....	13
1. Backgrounds and Motivation of the Research	13
2. History of Research.....	13
3. Why Bismuth Vanadate	14
4. Current Research Work on BVO:	15
5. Targets and Challenges of this Research:	17
Chapter 2 Literature Review.....	18
1. Crystal Structure of BiVO ₄	18
2. Fabrication of nanostructured BiVO ₄ crystals	20
1. Metal and non – metal doping	20
2. Facet Engineering	24
3. Morphology Control	28
4. Macro / meso – porous structure	31
3. Rietveld Analysis	36
1. Least squares method - Curve fitting (Interpolation)	36
2. Linear Curve Fitting	36
3. Nonlinear Curve Fitting.....	37
4. Fitting considerations	38
5. Requirements for Rietveld Analysis	38
6. Principle of Rietveld analysis	38
7. Intensity of the Bragg reflections	39
8. Quality of refinement.....	40
9. Rietveld Analysis Procedure	41
Chapter 3 Experimental	42
1. Introduction	42
2. Raw Materials	42

3. Synthesis Process:	43
1. Measurements	43
2. Heating & Stirring	43
3. Heating in autoclave	45
4. Centrifugation	45
4. Characterization	46
1. Phase Study.....	46
2. UV – Vis Spectroscopy	48
3. Microstructure Study	48
Chapter 4 Results and discussions	50
1. Phase Study	50
2. Rietveld Analysis	52
1. Confirmation of dual phase	52
2. Reason of formation of tetragonal zircon type BVO.....	54
3. Rietveld refinement of BVO S1	54
4. Rietveld refinement of BVO S2	56
5. Rietveld refinement of BVO S3	57
6. Rietveld refinement of BVO S4	58
7. Effect of doping	61
3. Microstructure Study.....	63
4. UV – Vis Analysis:	70
Chapter 5 Conclusions.....	73
Chapter 6 Suggestions for future work.....	74
References:	75

List of Figures

Fig 1 (a) Maximum solar-to-hydrogen conversion efficiency (η STH) and solar photocurrent as a function of the top cell band gap energy in a tandem cell.

Fig 1 (b) Schematic illustration of the basic mechanism of the BiVO₄-based photocatalytic process.

Fig 2.1 Cell conversion of (a) I-centered monoclinic to (b) C-centered monoclinic. a, b, c, and β represent the unit cell parameters for the I-centered cell and a', b', c', and β' for the C-centered cell.

Fig 2.2 (a) Monoclinic scheelite type BVO structure

Fig 2.3 (a) Visible-light-induced photocatalytic O₂ evolution and photocurrent density versus potential curves for metal-doped BiVO₄.

Fig 2.3 (b) Nyquist EIS and M-S plots of W- and Mo-doped BiVO₄. (c) Computed DOS of pure W- and Mo-doped BiVO₄ (d) Supercell of H-BiVO₄ formed by $2 \times 2 \times 2$ repetitions of the primitive cell (The white, red, green and blue circles represent vanadium, oxygen, bismuth and hydrogen atoms, respectively.). (e) & (f) M-S plots and photocurrent density versus potential curves collected on BiVO₄ and H-BiVO₄

Fig 2.4 (a) EIS measured at 0.7 V (vs. Ag/AgCl) in 0.5 M Na₂SO₄ solution of pristine BiVO₄, and 0.5, 1, and 5% PO₄-doped BiVO₄ under visible-light (>420 nm) irradiation. (b) Total and local partial DOS of BiVO₄ and PO₄-doped BiVO₄. (c) Calculated isosurface (0.04 eV Å⁻¹) of integrated charge density from -0.7 eV to Ef for PO₄-doped BiVO₄. (d) Photocurrent-potential curves. (e) Photocatalytic water oxidation of pristine BiVO₄, and 0.5, 1, and 5% PO₄-doped BiVO₄ under visible-light irradiation. (f) Up conversion emission spectra of Yb³⁺ and Er³⁺ co-doped BiVO₄ upon 980 nm excitation.

Fig 2.4 (g) Schematic illustration of the NIR-response resulting from lanthanide ions promoting an up-conversion luminescence.

Fig 2.5 Typical crystal of BiVO₄ exposed with the {010}, {011}, {110} and {111} facets.

Fig 2.6 (a) SEM and HRTEM images of BiVO₄ nanoplates exposed with the {001} facets.

Fig 2.6 (b) Facet (010/110)-dependent photoactivity of oxygen evolution on BiVO₄.

Fig 2.6 (c) Computed mechanism of facet-dependent photocatalytic oxygen evolution on BiVO₄.

Fig 2.7 (a) Charge separation between the {010} and {110} facets confirmed by Pt and PbO₂ photo deposition on BiVO₄ (b) Selective deposition of dual redox co-catalysts on specific facets of BiVO₄ (c, d) Photo electrocatalytic and photocatalytic water

oxidation activity of BiVO₄ with selectively deposited co-catalysts on specific facets and randomly distributed co-catalysts.

Fig 2.8 (a) Mechanism for the formation of BiVO₄ quantum tubes. (b) Optical absorption edge of BiVO₄ quantum tubes (top and bottom insets: photodegradation of RhB vs. irradiation time under visible light). (c) TEM image of BiVO₄ quantum tubes after the photodegradation.

Fig 2.9 (a) Formation mechanism, UV-Vis absorption, and RhB photodegradation of hollow BiVO₄ microspheres.

Fig 2.9 (b) Morphology evolution of BiVO₄ hollow spheres via a hydrothermal method using urea as the guiding surfactant (I: 2 h; II: 4 h; III: 8 h; IV: 12 h; V: 24 h; scale bar is 2 μm)

Fig 2.9 (c) Morphology evolution of hyper branched BiVO₄ at intervals of 10 min (I), 20 min (II), 30 min (III), 45 min (IV), 1 h (V), and 3 h (VI), respectively (the scale bars are 100, 200, 200, 200, 400 and 500 nm, respectively).

Fig 2.10 (a) Proposed process for the fabrication of ordered mesoporous BiVO₄

Fig 2.10 (b) (i) Schematic representation of dual porosity in periodically ordered porous BiVO₄

Fig 2.10: (b) (ii) typical SEM images of corresponding BiVO₄ (iii) relationship between PEC performance and dual porosity.

Fig 2.11 Interpolation

Fig 2.12 (a) Linear curve fitting or regression

Fig 2.11 Interpolation

Fig 3.1 Electronic mass balance (CSC Balance, model: JF2204)

Fig 3.2 Nabertherm High Temperature Furnace (model: HT 16/18).

Fig 3.3 Teflon lined stainless steel autoclave

Fig 3.4 Laboratory centrifuge machine

Fig 3.5 X – Ray Diffractometer

Fig 3.6 UV-Vis spectrometer (UV/Vis/NIR – Lambda 1050, PerkinElmer, USA).

Fig 3.7 Schematic of a single beam UV – Vis Spectrophotometer

Fig 3.8 Field Emission Scanning Electron Microscope [FESEM: JEOL JSM 7600F].

Fig 4.1(a) PXRD patters of BVO S1 and BVO S2 at room temperature.

Fig 4.1(b) PXRD patters of BVO S2, BVO S3 and BVO S4 at room temperature.

Fig 4.2 (a) Bragg reflections for pure monoclinic BVO

Fig 4.2 (b) Bragg reflections for pure tetragonal scheelite BVO

- Fig 4.2 (c) Bragg reflections for pure tetragonal zircon type BVO
- Fig 4.2 (d) Bragg reflections for pure monoclinic Bi₂O₃
- Fig 4.3 Transformation of phases of BVO with temperature
- Fig 4.4 Identification of Bi₂O₃ phase which has been found in BVO S1
- Fig 4.5 (a) Rietveld refinement of BVO S1 with pure m-BVO pattern (Green circles indicate the unmatched Bragg reflections) (b) PXRD pattern of pure tetragonal zircon type BVO
- Fig 4.6 (a) Rietveld refinement of BVO S2 with pure monoclinic BVO pattern (Green circle indicates the unmatched Bragg reflection which is identified as tetragonal zircon BVO) (b) Pure tetragonal zircon type BVO pattern
- Fig 4.7 (a) Rietveld refinement of BVO S3 with pure monoclinic BVO pattern (Green circles are the unmatched Bragg reflections) (b) PXRD pattern of pure tetragonal zircon type BVO (Green circles show the unmatched reflections match with tetragonal zircon type BVO)
- Fig 4.8 (a) Rietveld refinement of BVO S4 with pure monoclinic BVO (Green circles show unmatched Bragg reflection) (b) PXRD pattern of pure tetragonal zircon type BVO
- Fig 4.9 Crystal structure of pure monoclinic BVO
- Fig 4.10 Schematic diagram explaining the bandgap reduction in m – BVO
- Fig 4.11 (a) Typical crystal of BiVO₄ exposed with the {010}, {110}, {011} and {111} facets. (b) Schematic illustration of different morphologies of BiVO₄
- Fig 4.12 FESEM of BVO S1 in (a) & (b) x 50,000
- Fig 4.13 FESEM of BVO S1 in (a) x 100000 & (b) x 150000
- Fig 4.14 FESEM of BVO S2 in (a) & (b) x 30,000
- Fig 4.15 FESEM of BVO S2 in (a) & (b) x 50,000
- Fig 4.16 FESEM of BVO S3 in (a) x 50,000 & (b) x 10,000
- Fig 4.17 FESEM of BVO S4 in (a) x 15,000 & (b) x 30,000
- Fig 4.18 UV – Vis absorption spectra of BVO S2, BVO S3 & BVO S4
- Fig 4.19 [hvF(R)] 2vs photon energy (hv) plots to calculate band gap energy of BVO S2
- Fig 4.20 [hvF(R)] 2vs photon energy (hv) plots to calculate band gap energy of (a) BVO S3 & (b) BVO S4

List of Tables

Table 1	Information of raw materials
Table 2	Preparative parameters of synthesized samples of BiVO ₄
Table 3	Rietveld refinement outputs
Table 4	Cell parameters obtained by refinement
Table 5	Bond lengths obtained after refinement

Chapter 1 Introduction

1. Backgrounds and Motivation of the Research

Due to rapid growth rate of population, the need of more energy is rising higher day by day along with the environmental pollution (i.e. CO₂ emission, water pollution). New industries are set up and expanded to fulfill the requirements of this rapid growing population all over the world. Though greenhouse effect is making sure of increasing water level but scarcity of pure water has become an alarming issue nowadays. To make our earth sustainable, there are mainly two focuses in researchers' hands:

- Water purification
- Minimize CO₂ emission rate

Thus water oxidation mechanism has become one of the most important concerns to the researchers. Unfortunately the percentage of energy we can store from solar energy is inadequate for natural water oxidation. Again performing water purification in laboratory with the help of external sources of energy cannot help us to make a sustainable world in near future. So, the need of a very special material has been appeared which will enhance the water oxidation process naturally in open environment with the help of solar energy only and here comes the artificial photosynthesis mechanism. Researchers are desperate to find a suitable photocatalyst as well as an oxide based semiconductor for this purpose but such kind of material hasn't been discovered yet.

2. History of Research

Ever since the decomposition of water on a TiO₂ electrode under UV light irradiation was first reported in 1972 by Honda & Fujishima [1], photocatalytic processes based on semiconductors have offered the most promising solutions. They can both be used for water splitting to produce hydrogen and oxygen and for the degradation of toxic pollutants in wastewater treatment. TiO₂ is by far the most widely used and investigated photocatalyst due to its high efficiency and photo stability [2, 3]. In addition, it is non-toxic and commercially available at a low price. However, TiO₂ has a major drawback that has not been overcome till date. As its band gap is rather wide (3.2 eV), TiO₂ needs to be activated through UV irradiation that represents only 4% of the energy of the sunlight arriving on the earth's surface. Recent progress in the field has demonstrated that the development of functionalized ternary and higher oxides is an efficient strategy to overcome the intrinsic limitations of binary metal oxides [4]. A wide variety of ternary oxides, e.g. CaBi₂O₄ [5], Bi₂WO₆ [6], BiSbO₄ [7] or AgNbO₃ [8], has been found to exhibit high photocatalytic performance under visible light irradiation. As the process of water splitting on oxide surfaces involves a very complex interplay of defect chemistry, grain boundaries and other detailed solid-state features, the performance of oxide

photocatalysts furthermore depends on their morphology and their “preparative history”. This calls for sophisticated synthetic approaches to homogeneous and phase-pure nano scale photocatalysts with high surface area, uniform morphology and a high degree of crystallinity.

Layered compounds, such as K₄Nb₆O₁₇ [9], Bi₂InNbO₇ [10], Sr₂Nb₂O₇ [11], Bi₂WO₆ [12] etc., have been attracting attention recently since they are much more active than the generally used TiO₂ or SrTiO₃, TiO₂-SiO₂, ZnO, La₂Ti₂O₇, Sr₃Ti₂O₇, Sm₂Ti₂O₇, La₄ CaTi₅O₁₇ [13-15]. Bismuth based compounds such as BiVO₄, Bi₂WO₆, Bi₂MoO₆, CaBi₂O₄, BiNbO₄ and BiTaO₄ Ba₂YbZrO_{5.5} have been reported as new photocatalytic materials [16, 17]. Many Bi³⁺ containing oxides exhibit photocatalytic properties due to the hybridized O (2p) and Bi (6s) valence bands [18].

3. Why Bismuth Vanadate

The layered vanadate BiVO₄ has attracted increasing research interest as a photocatalyst and it exists in three modifications: the monoclinic scheelite type and the tetragonal zircon and scheelite types, respectively. Monoclinic BiVO₄ is one of the most promising visible-light-driven photocatalysts due to

- Proper VB edge located at ca. 2.4 eV vs. RHE [8p]
- The narrow bandgap [19] so that it has been synthesized with a variety of methods, such as solid-state reactions [20], co-precipitation [21], metal-organic decomposition [22], sonochemical [23] and hydrothermal reactions [24].
- Plentiful abundance, low cost, and good stability (as demonstrated in test of several tens of hours) [25-28]
- Theoretical solar-to-hydrogen conversion efficiency (η_{STH}) approaches 9.2% with a maximum photocurrent of 7.5 mA cm⁻² under standard AM 1.5 solar light irradiation (Fig. 1a) [26-27].

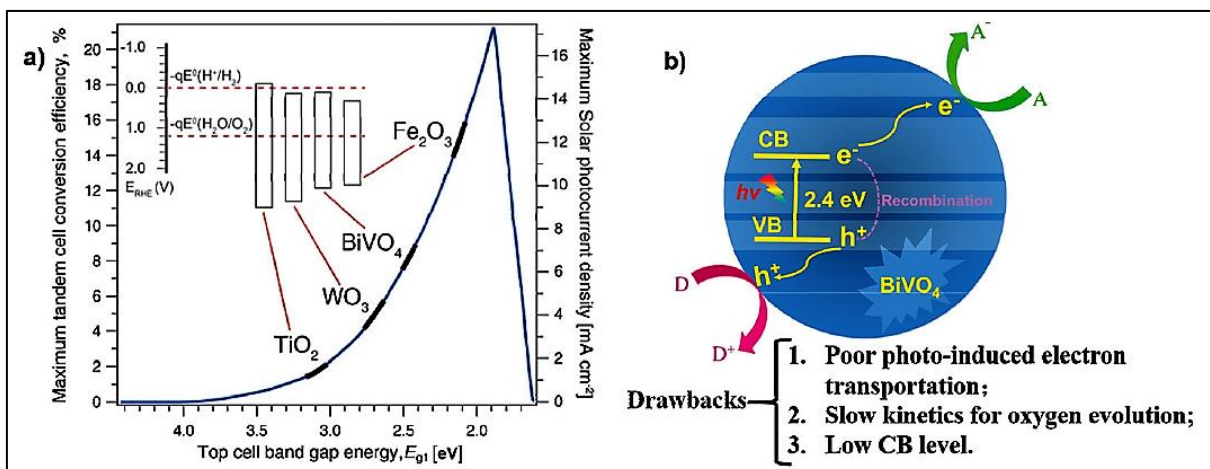


Fig 1: (a) Maximum solar-to-hydrogen conversion efficiency (η_{STH}) and solar photocurrent as a function of the top cell band gap energy in a tandem cell (reproduced from ref. 26. Copyright 2013, American Chemistry Society). (b) Schematic illustration of the basic mechanism of the BiVO₄-based photocatalytic process.

To date, however, the actual conversion efficiency achieved with BiVO₄-based materials is far below what is expected, because it suffers from some drawbacks (Fig. 1b).

- Slow charge transportation, especially electron transportation, leading to approximately 60%–80% of the electron–hole pairs recombining before they reach the interfaces [28].
- The localization of photo-induced electrons, together with the polar nature of BiVO₄, suggests that self-trapping and small electron polaron formation could retard the charge separation [29]
- Slow kinetics of water oxidation [30]
- Conduction band (CB) edge is located below the reversible hydrogen electrode (RHE) level, and therefore it requires an external bias potential for photo electrochemical (PEC) hydrogen evolution (Fig. 1a) [26]

4. Current Research Work on BVO:

- ❖ **Y. Zhou et al, 2010** have performed an extensive parameter screening of the hydrothermal synthesis of BiVO₄ and reported that facile morphology control of BiVO₄ particles in Bi (NO₃)₃.5H₂O/V₂O₅/K₂SO₄ hydrothermal system can be achieved through K₂SO₄ as an inorganic additive that enhances the photocatalytic activity. They have also found that addition of K₂SO₄ produces potassium vanadate fibers as second phase which has also its own photocatalytic effect along with the BiVO₄. Addition of inorganic additives as morphology controlling agent has been found helpful [39].
- ❖ **S. Obregon et al, 2012** have studied different morphologies of crystalline m-BiVO₄ produced by surfactant free hydrothermal route by changing pH, directing agent, temperature and time. The best performance was clearly not associated to the surface area values, and is strongly affected by the crystallite size and morphology. For the different series obtained, better photocatalytic performances have been achieved for m-BiVO₄ with needle-like morphology. It is worthy to note that upon illumination with a low intensity lamp (35 W), the conversion rate for such system is about 60% degradation after 2 h of irradiation [40]
- ❖ **Zhang et al, 2014** prepared an Al-doped ZnO inverse opal (io-AZO) structure modified BiVO₄ photo anode via an opal template by evaporation- induced self-assembly of polystyrene spheres (PS). Al-doped ZnO inverse opal (io-AZO) were used to facilitate the charge transport system. Scheelite monoclinic phase was obtained in XRD. Inverse opal reduces the diffusion length of charge carriers and serves as electron collector. A photocurrent of 1.5 mAcm⁻² at 1.23 V vs. RHE under AM 1.5G illumination was obtained which was three times higher than unmodified BiVO₄ photo anode [31].
- ❖ **Ding et al, 2014** using DFT computations electronic structures and optical properties of BiMO₄ (M = V, Nb, Ta) performed to get information about their photocatalytic activities. They compared the relative ratio of effective mass and the study showed that BiVO₄ has superior mobility of carriers and

excellent separation of photo excited electron–hole pairs in the [010] direction due to its layered structure and the preferred distribution of electrostatic potential [32].

- ❖ **Qin et al, 2014** prepared monoclinic BiVO₄ film on a transparent conducting substrate for photo electrochemical oxidation of water and films were modified further by reduction with NaBH₄. Photo electrochemical performance was studied by electrochemical impedance and the Mott–Schottky. The FE-SEM images showed BiVO₄ crystals with diameters below 500 nm with no obvious change in morphology after reduction. Photocurrent of 2.3 mA/cm² was obtained under visible light due to increased donor density and effective charge carrier separation and transportation [33]
- ❖ **Luo et al, 2013** have done doping studies with Mo⁶⁺, W⁶⁺ and Sn⁴⁺ on BiVO₄ system to see the photo electrochemical water splitting performance. The pure/modified BiVO₄ were prepared by modified metal organic decomposition method. The films were characterized by XRD, Raman, UV-Vis transmission spectroscopy, XPS and SEM. Raman and XPS were used to reveal information about the doping site in crystal lattice of BiVO₄. All peaks in XRD shows the monoclinic phase of BiVO₄. Theoretical calculations were used to obtain formation energy of dopant ions which in turn gave the suitability of the dopant as impurity for semiconductor photo electrodes. Poor performance of Sn-doped BiVO₄ is due to higher formation energy and lower solubility of impurity ions in comparison to Mo or W substituted V sites [34].
- ❖ **Yang et al, 2013** have performed theoretical calculations on visible light responsive monoclinic scheelite BiVO₄ which is known for its effective oxygen evolution reaction. For exploring photocatalytic water oxidation properties of different facets of BiVO₄ (such as (010), (110), and (011) facets), DFT calculations were used to reveal the geometric structure, optical properties, electronic structure, water adsorption, and the whole OER free-energy profiles on BiVO₄ (010) and (011) facets. Both favorable and unfavorable factors for OER on both facets were calculated through obtained results [35].
- ❖ **Tokunaga et al, 2001** have studied photocatalytic activity of BiVO₄ which is a ferroelectric and ion conductive material and crystal form rules its properties .The three main crystal forms of BiVO₄ are 1. Zircon structure with tetragonal system (z-t) 2. Scheelite structure with monoclinic (s-m) system 3. Scheelite structure with tetragonal (s-t) system under visible light irradiation, the photocatalytic activity of monoclinic BiVO₄ is found to be higher due to presence of a 6s² lone pair of Bi³⁺ which causes distortion of a Bi-O polyhedron [36].
- ❖ **Usai et al, 2013** have studied the effect of Y³⁺ doping in monoclinic-tetragonal heterostructured BiVO₄ and observed the photocatalytic activities. They performed a hydrothermal synthesis which led to mixed phase system as yttrium is incorporated in the structure. They showed that tetragonal phase is stabilized as Y³⁺ amount increases, being almost the unique phase present for doping content higher than 3 at. %. From Rietveld refinement it's clearly stated that dopant inclusions takes place in both crystalline phases. While

yttrium produces a cell expansion in monoclinic but a progressive contraction in tetragonal phase was also observed. The final enhanced photo activity for 3 at. % Y₃⁺ might be attributed to the formation of a monoclinic–tetragonal structure and a lower crystallite size of the heterostructured catalysts which directly affect the transport and diffusion of the charge carriers. [37]

- ❖ **G. P. Nagabhushana et al, 2012** demonstrated a novel synthetic strategy to produce highly effective visible-light-driven photocatalyst m- BiVO₄ and investigated its activity for H₂ evolution under UV light in water–ethanol systems. They showed that the important steps involved in the synthesis of BiVO₄ are to control the solution preparation, amalgamation and the quantity of precursor used for the reaction. They noticed that the amount of precursor solution used for the combustion reaction plays an important role in achieving the impurity free product that depends upon the availability of required oxygen in the reaction chamber. The significant outcome of the entire study is H₂ evolution in water–ethanol system by BiVO₄ under UV light. They suggested a structural investigation needs to be carried out to identify the reason behind the H₂ evolution under UV light [38].

5. Targets and Challenges of this Research:

Synthesis of monoclinic BiVO₄ depends completely on the synthesis parameters. Enhanced photocatalytic activity of both pure monoclinic BiVO₄ and monoclinic – tetragonal heterostructured BiVO₄ have been reported in recent researches. The main focus of this research is to investigate the synthesis process of formation of these two nanoparticles mentioned above in a straightforward hydrothermal process. The targets can be summarized as below:

- Effect of the addition of K₂SO₄ as morphology controlling agent on formation of monoclinic – tetragonal heterostructured BiVO₄
- Effect of Nb doping at Bi ³⁺ sites on structural formation, optical bandgap and particle morphology
- Effect of Mn doping at V ⁵⁺ sites on structural formation, optical bandgap and particle morphology

Though BiVO₄ has been recently known as the most promising photocatalyst, no work based on BiVO₄ photocatalyst has been conducted in our department or even in our university. This is the first work on BiVO₄ photocatalyst in Bangladesh to the best of our knowledge. In addition, effects of the Nb doping at Bi ³⁺ sites in BiVO₄ has not been studied anywhere in the world yet. On this point of view, this work imposes an entirely new challenge to us along with the limitation of technical facilities which confines the scope of working. However this work, if carried out successfully, has the potential to provide better insights to the study of photocatalytic activities in future.

Chapter 2 Literature Review

1. Crystal Structure of BiVO₄

BiVO₄ occurs naturally as the mineral pucherite with an orthorhombic crystal structure [18]. However, BiVO₄ prepared in the laboratory does not adopt the pucherite structure but crystallizes either in a scheelite or a zircon-type structure.



BVO crystalizes in 2 form:

- Scheelite type structure
 - i) Monoclinic (space group $I2/b$ with $a = 5.1935 \text{ \AA}^\circ$, $b = 5.0898 \text{ \AA}^\circ$, $c = 11.6972 \text{ \AA}^\circ$, $\beta = 90.387^\circ$)
 - ii) Tetragonal (space group $I4_1/a$ with $a = b = 5.1470 \text{ \AA}^\circ$, $c = 11.7216 \text{ \AA}^\circ$)
- Zircon type structure
 - i) Tetragonal (space group $I4_1/a$ with $a = b = 7.303 \text{ \AA}^\circ$, $c = 6.584 \text{ \AA}^\circ$)

Difference between scheelite type tetragonal and zircon type tetragonal structure:

Lattice parameter

Difference between scheelite type tetragonal and scheelite type monoclinic structure:
Distortion

Monoclinic scheelite structure:

- I -centered (body centered) monoclinic cell (space group $I2/b$): $a = 5.1935 \text{ \AA}^\circ$, $b = 5.0898 \text{ \AA}^\circ$, $c = 11.6972 \text{ \AA}^\circ$, $\beta = 90.387^\circ$
- C -centered monoclinic cell (space group $C2/c$): $a = 7.2472 \text{ \AA}^\circ$, $b = 11.6972 \text{ \AA}^\circ$, $c = 5.0898 \text{ \AA}^\circ$, $\beta = 134.225^\circ$

When referring space groups, it is necessary to mention which one. In the scheelite structure, each V ion is coordinated by four O atoms in a tetrahedral site and each Bi ion is coordinated by eight O atoms from eight different VO₄ tetrahedral units [20]. Fig 2.2 (a) shows the four-coordinated V center and the eight coordinated Bi center alternating along the [001] direction. Each O atom in this structure is coordinated to two Bi centers and one V center, holding the Bi and V centers together forming a three dimensional structure. The only difference between the tetragonal and monoclinic

scheelite structure is that the local environments of V and Bi ions are more significantly distorted in the monoclinic structure, which removes the four-fold symmetry necessary for a tetragonal system.

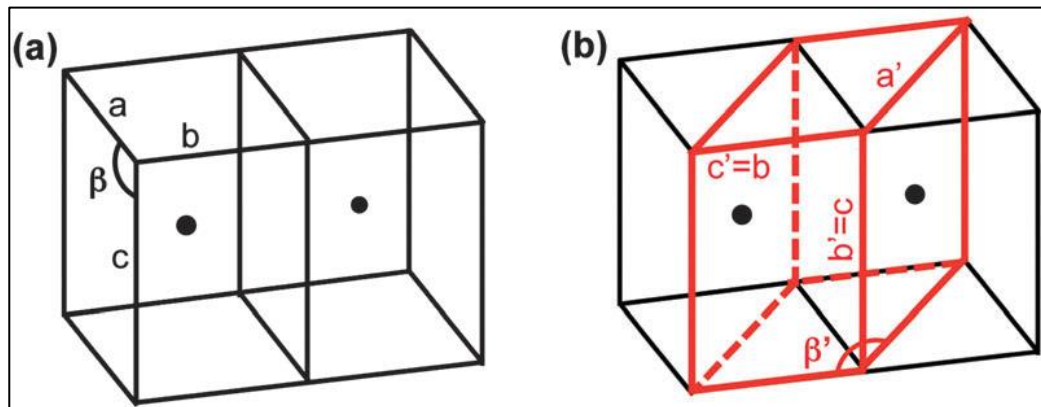


Fig 2.1: Cell conversion of (a) I-centered monoclinic to (b) C-centered monoclinic. a , b , c , and β represent the unit cell parameters for the I-centered cell and a' , b' , c' , and β' for the C-centered cell.

For example, while all four V–O bond lengths were equal in tetragonal scheelite (1.72 \AA), two different V–O bond lengths exist in a monoclinic scheelite structure (1.77 \AA and 1.69 \AA). In the same manner, while only two very similar Bi–Odistancess exist in the tetragonal scheelite structure (2.453 \AA and 2.499 \AA), the Bi–O distances in the monoclinic scheelite structure vary significantly (2.354 \AA , 2.372 \AA , 2.516 \AA and 2.628 \AA) [20].

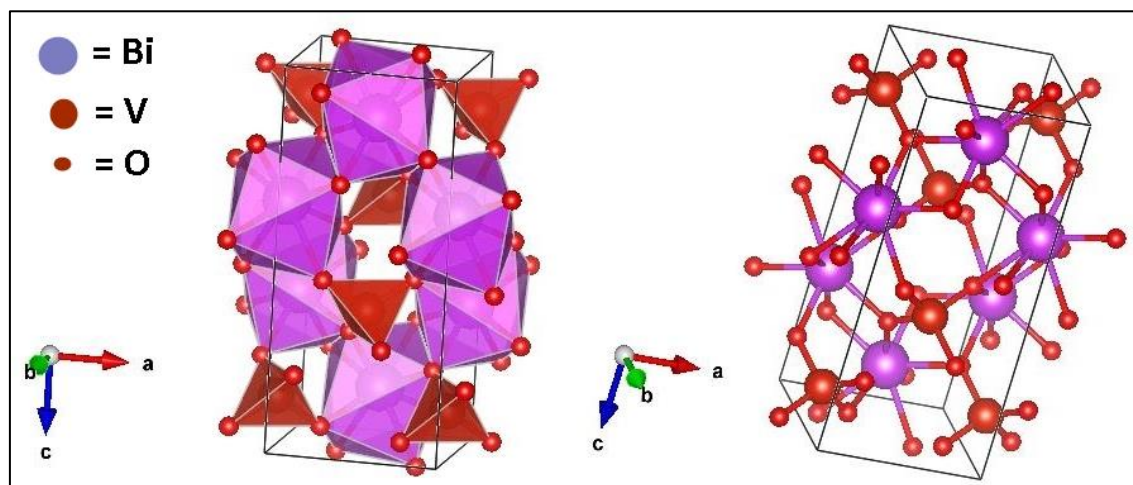


Fig 2.2 (a): Monoclinic scheelite type BVO structure

The significant distortion of the Bi-polyhedral indicates that the Bi 6s alone is more sterically expressed in the monoclinic scheelite structure. It should be noted that the space

group, I2/b, with which the monoclinic scheelite structure of BiVO₄ was originally reported is a non-standard space group.²⁰ It can be converted to a standard space group, C2/c, which is used in some recent studies of BiVO₄. Changes in the crystallographic axes via the conversion of a monoclinic I-centered (body-centered) cell to a monoclinic C-centered cell are shown in Fig 2.1 (a). With this cell conversion, the new cell parameters for C2/c are $a' = 7.2472 \text{ \AA}$, $b' = 11.6972 \text{ \AA}$, $c' = 5.0898 \text{ \AA}$, and $\beta = 134.2251$. The choice of the I-centered monoclinic cell has the advantage of easily showing its structural relationship to the tetragonal scheelite structure that was reported in a body centered space group, I41/a, using the identical unit cell choice and crystallographic axes. Since both I2/b and C2/c space groups, which have different unit cell choices and crystallographic axes, are commonly used to describe the monoclinic scheelite structure of BiVO₄, it is necessary to clarify the space group used when referring to specific atomic planes or crystal directions as well as the hkl indices of X-ray diffraction peaks in order to prevent any possible confusion.

2. Fabrication of nanostructured BiVO₄ crystals

1. Metal and non – metal doping

The doping of impurities of metal and nonmetal into BiVO₄ is a commonly adopted technique to modify its optoelectronic properties [41-50]. Depending on the impurity type (shallow or deep) and the nature of the valence (inert lattice mismatching, donor, acceptor) of the dopants, the following possibilities are most likely to occur:

- ❖ Extension of optical absorption toward longer wavelengths
- ❖ Improvement in the surface adsorption for chemical species
- ❖ enhancement in electrical conductivity through modified charge-carrier properties (mobility, diffusion, or concentration)
- ❖ Efficient separation of photo-induced charge carriers [43]

For the specific case of BiVO₄ however, **doping mainly improves the charge separation instead of extending the absorption edge**. In various studies, the incorporation of tungsten or molybdenum into BiVO₄ has been shown to be very promising for enhancing the electronic conductivity and thus preventing electrons from accumulating in the bulk [41-43]. As shown in Fig2.3 (a) compared with pristine BiVO₄, doped BiVO₄ shows a positive flat band shifting at about 30 mV, probably resulting from the shifting of the bulk Fermi level via doping. Furthermore, a 1.6–2 times higher carrier concentration and a 3–4 times suppressed charge-transportation resistance are observed, although the absorption edge wavelength representing the optical band gap energy is basically unchanged [43]. First-principles electronic structure calculations {Fig2.3 (b)} show that Mo and W replacing V sites act as shallow electron donors [43]. The density of states (DOSs) of Mo is not only much higher than those of W, but is also directionally coupled with those of V sites near the bottom of CB, indicating that Mo serves as a more efficient electron donor than W and other dopants. Therefore, Mo is more effective in improving photocatalytic oxygen evolution {Fig2.3 (c) top}. Under standard AM 1.5 solar light and at 1.23 V versus RHE, a photocurrent density of about 2.38 mA cm⁻² is

achieved for Mo doping, followed by W doping (1.98 mA cm^{-2}), whereas the photocurrent is only 0.42 mA cm^{-2} for undoped BiVO₄ {Fig 2.3 (c) bottom} [43]. Interestingly, Li et al. demonstrated hydrogenation as a facile method to significantly enhance the photo electrochemical water oxidation performance of BiVO₄ films by introducing oxygen vacancies, as well as hydrogen impurities {Fig2.3 (d)} [46]. DFT calculations predict that both oxygen vacancies and hydrogen impurities are shallow donors for BiVO₄ with low formation energies.

These defects could increase the donor densities of BiVO₄ without introducing deep trap states. EIS and M-S measurements show that the donor densities of BiVO₄ films were significantly enhanced upon hydrogenation {Fig2.3 (e)}. As a result, hydrogen-treated BiVO₄ (H-BiVO₄) photo anodes achieve a photocurrent density of 3.5 mA cm^{-2} at $1.0 \text{ V vs. Ag/AgCl}$, which is one order of magnitude higher than that of pure BiVO₄ obtained at the same potential {Fig(3f)}.

In addition, Lee et al. reported a new concept of oxoanion doping, using PO₄ oxoanions to replace VO₄ oxoanions in BiVO₄ [50]. Similar to Mo/W doping, PO₄ oxoanion doping also does not bring significant changes to the optical absorption and crystal structure of BiVO₄.

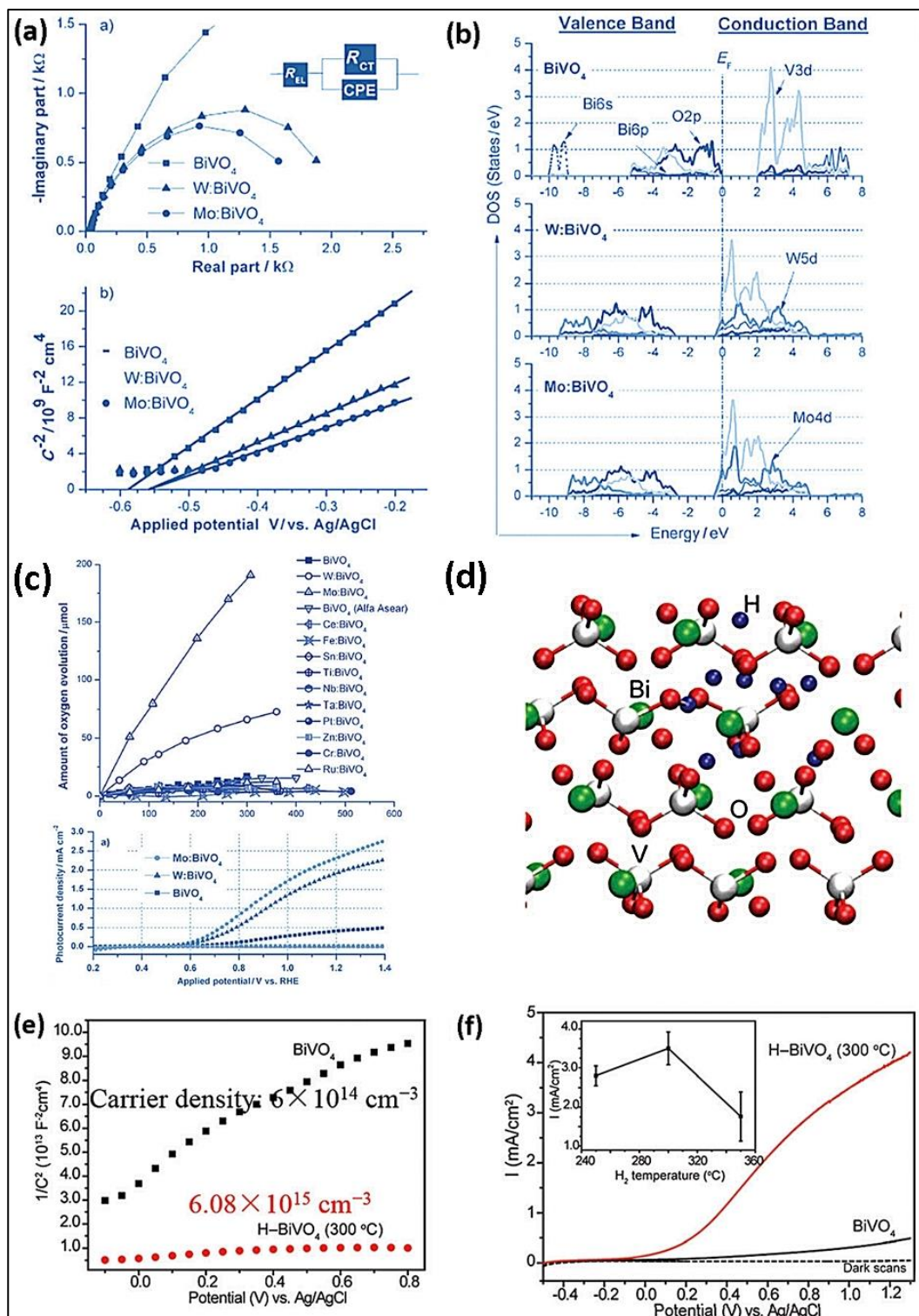


Fig 2.3: (a) Visible-light-induced photocatalytic O₂ evolution and photocurrent density versus potential curves for metal-doped BiVO₄. (b) Nyquist EIS and M-S plots of W- and Mo-doped BiVO₄. (c) Computed DOS of pure W- and Mo-doped BiVO₄ (a-c reproduced from ref 43. Copyright 2013, John Wiley & Sons). (d) Supercell of H-BiVO₄ formed by 2 × 2 × 2 repetitions of the primitive cell (The white, red, green and blue circles represent vanadium, oxygen, bismuth and hydrogen atoms, respectively.). (e) & (f) M-S plots and photocurrent density versus potential curves collected on BiVO₄ and H-BiVO₄ (d-f reproduced from ref 78. Copyright 2013, American Chemistry Society).

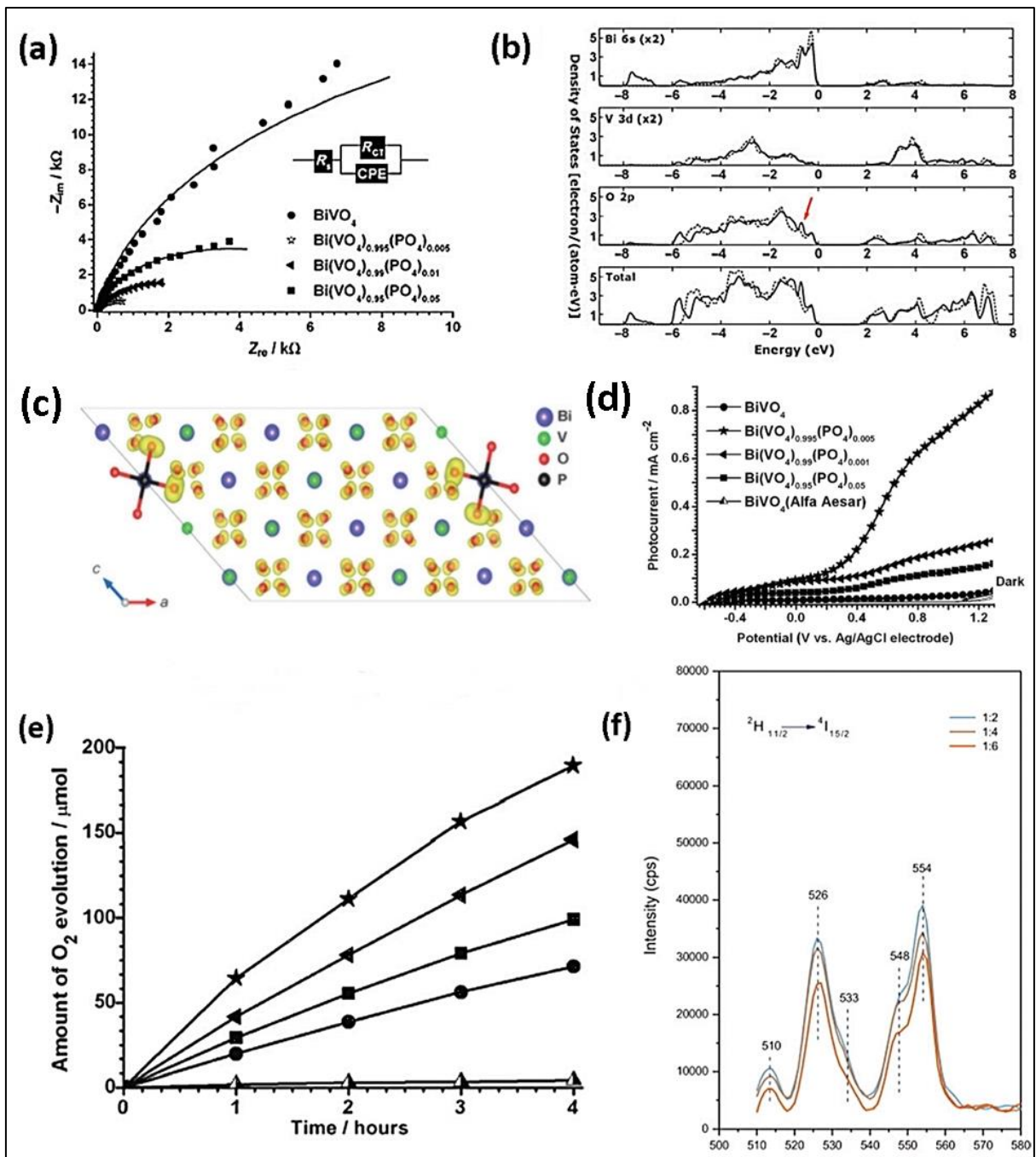


Fig 2.4: (a) EIS measured at 0.7 V (vs. Ag/AgCl) in 0.5 M Na₂SO₄ solution of pristine BiVO₄, and 0.5, 1, and 5% PO₄-doped BiVO₄ under visible-light (>420 nm) irradiation. (b) Total and local partial DOS of BiVO₄ and PO₄-doped BiVO₄. (c) Calculated isosurface (0.04 el Å⁻¹) of integrated charge density from -0.7 eV to E_f for PO₄-doped BiVO₄. (d) Photocurrent-potential curves. (e) Photocatalytic water oxidation of pristine BiVO₄, and 0.5, 1, and 5% PO₄-doped BiVO₄ under visible-light irradiation (a-e reproduced from ref 50. Copyright 2012, John Wiley & Sons). (f) Up conversion emission spectra of Yb³⁺ and Er³⁺ co-doped BiVO₄ upon 980 nm excitation (reproduced from ref 51. Copyright 2014, Elsevier).

However, it can lower the charge transportation resistance, as confirmed by the increased charge carrier's concentration via the DFT calculations {Fig2.4 (a) – (c)}. As a result, PEC and photocatalytic water oxidation are promoted significantly by a factor of about 30 with respect to pure BiVO₄ {Fig2.4 (d) &(e)}. Recently, Colón et al. synthesized Yb³⁺ and Er³⁺ co-doped BiVO₄ with good NIR photo activity [51] resulting from the lanthanide ions promoting an up-conversion luminescence {Fig 2.4 (f) & (g)} [51-52]. This provides a possibility to greatly extend the wavelength range that can be used in photo catalysis.

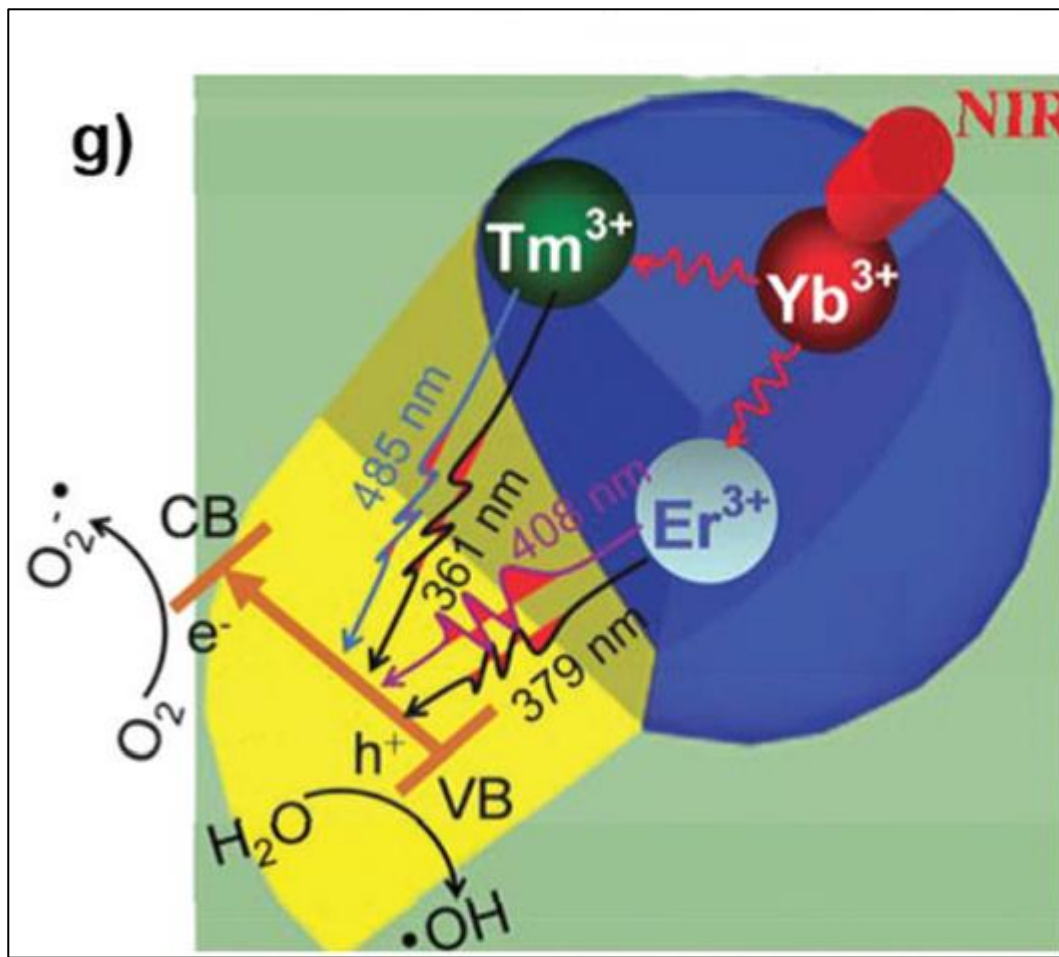


Fig 2.4: (g) Schematic illustration of the NIR-response resulting from lanthanide ions promoting an up-conversion luminescence (g reproduced from ref 52. Copyright 2014, RSC Society of Chemistry).

2. Facet Engineering

Crystal facets play a critical role in photo catalysis because surface active sites and even the electronic structure is dependent on the specific crystal facets [53] and consequently, the synthesis of crystals exposed with highly reactive facets has attracted much interest [53-59]. Xi et al. synthesized well-defined BiVO₄ Nano sheets exposed with {001} facets using a straightforward hydrothermal route without any template or organic surfactant {Fig2.6 (a)} [54]. Typically, BiVO₄ crystals show a regular decahedron shape

with controllable exposed facets of {010}, {011}, {110} and {111}, as shown in Fig2.5. Li et al. synthesized BiVO₄ with a highly exposed (010) facet using TiCl₃ as a directing agent, and correlated this to the high activity in O₂ evolution on BiVO₄ {Fig2.6 (b)} [55] subsequently, facet-dependent photocatalytic activity for water oxidation on BiVO₄ was investigated by DFT calculations, particularly between the (010) and (011) facets {Fig 2.6 (c)} [56].

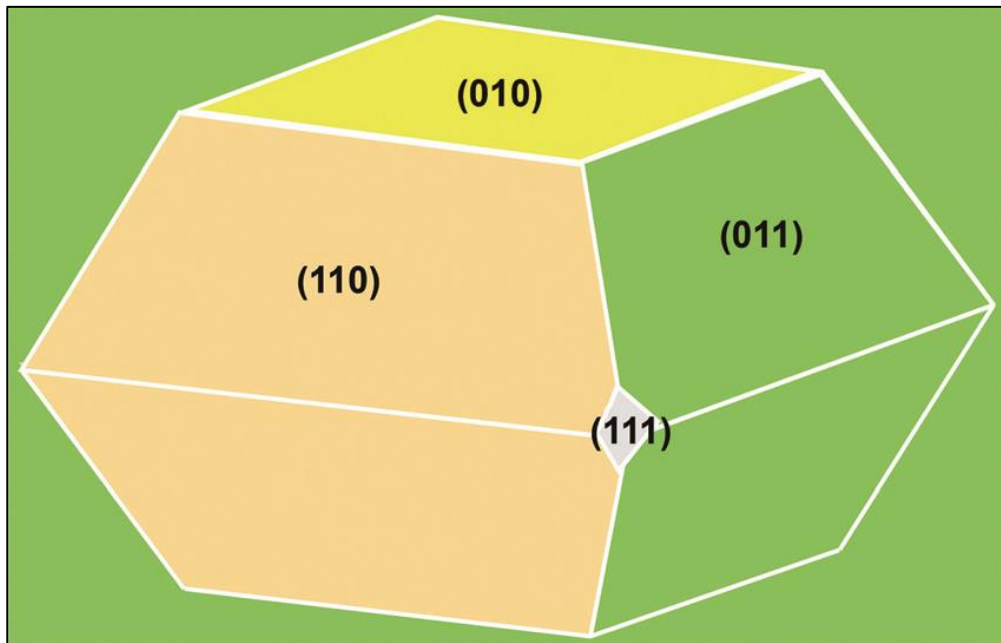


Fig 2.5: Typical crystal of BiVO₄ exposed with the {010}, {011}, {110} and {111} facets.

Compared with the (011) facet, the (010) facet has a high activity because of the following advantages: higher charge carriers mobility, easier adsorption of water, and lower overall potential-energy of O₂ evolution. Notably, recent investigations have demonstrated that photo-induced electrons and holes may be driven to different crystal facets [57-59]. Thus, photo-reduction and oxidation can occur preferentially over different facets, which hints at the cooperation of different facets being very important to obtain high quantum efficiency. Using photochemical labeling, Li et al. demonstrated that, the reduction reaction (Pt-photo deposition) caused by photo-induced electrons and the oxidation reaction (MnO_x-photodeposition) by photo-induced holes take place on the {010} and {110} facets, respectively {Fig2.7 (a)} [58] which suggests that the photo-induced electrons and electrons move to the {010} and {110} facets, respectively. Moreover, it provides a very useful way to selectively deposited co-catalyst on specific facets via photo deposition {Fig2.7 (b)} [59]. With Pt on the {010} facets and MN Ox on the {110} facets, the photocatalyst shows much a higher activity in both photocatalytic and PEC water oxidation, compared with the counterparts with randomly distributed Pt and PbO₂ co-catalysts {Fig2.7 (c) &(d)}. The coupling of co-catalysts with semiconductor facets may represent a new strategy for developing highly efficient photocatalysts.

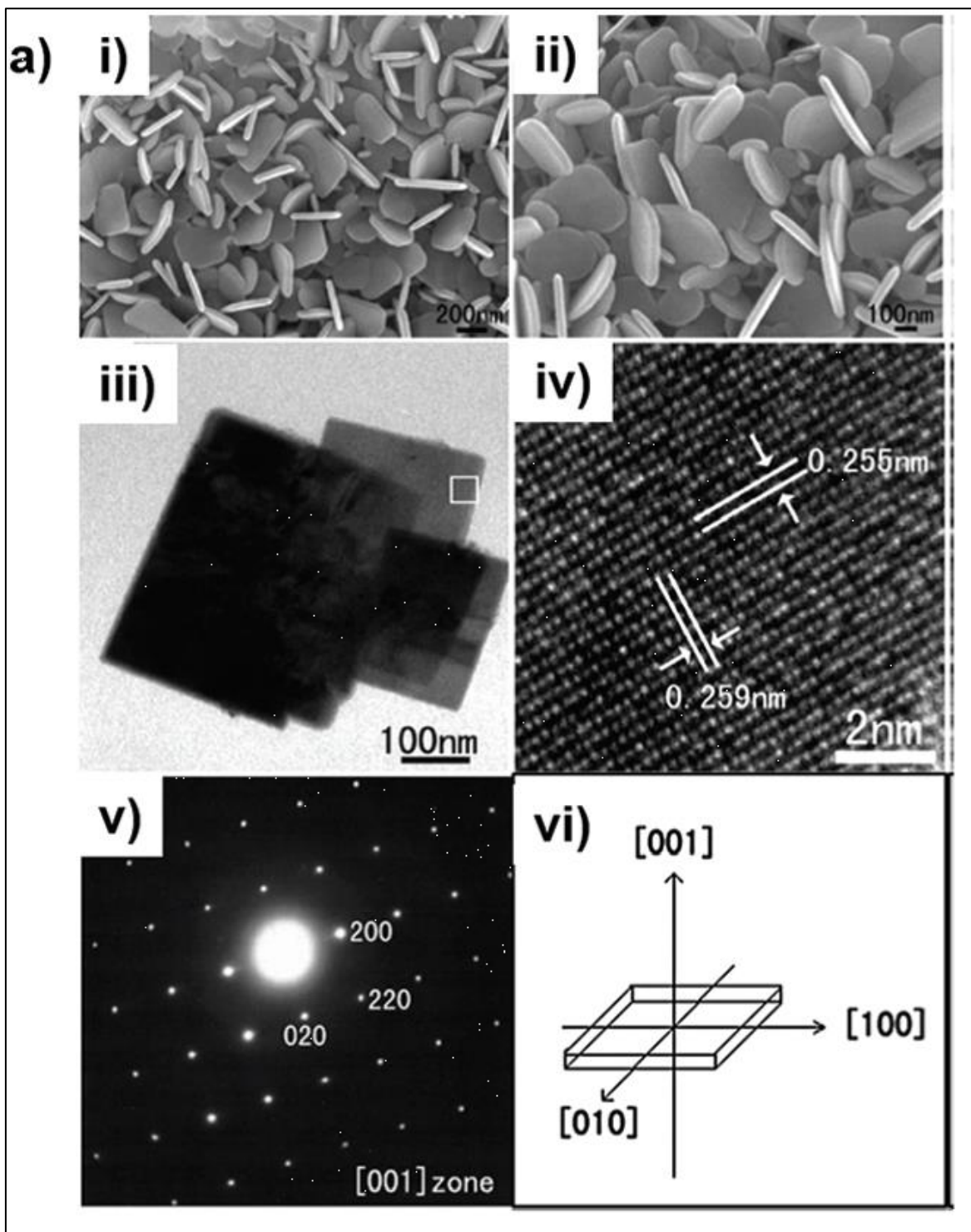


Fig 2.6: (a) SEM and HRTEM images of BiVO_4 nanoplates exposed with the $\{001\}$ facets (reproduced from ref 54. Copyright 2010, Royal Society of Chemistry).

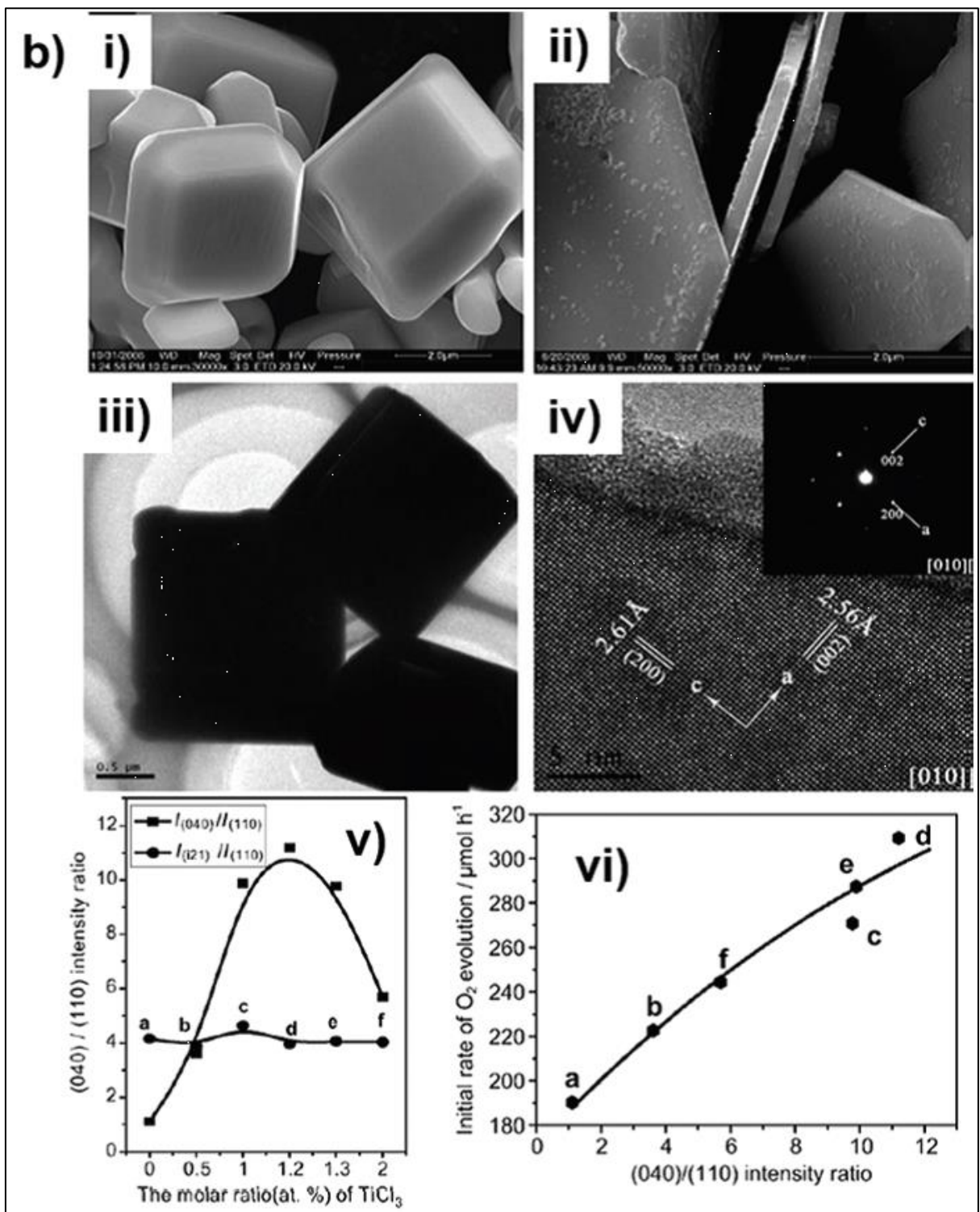


Fig 2.6: (b) Facet (010/110)-dependent photoactivity of oxygen evolution on BiVO_4 (reproduced from ref 55. Copyright 2011, John Wiley & Sons).

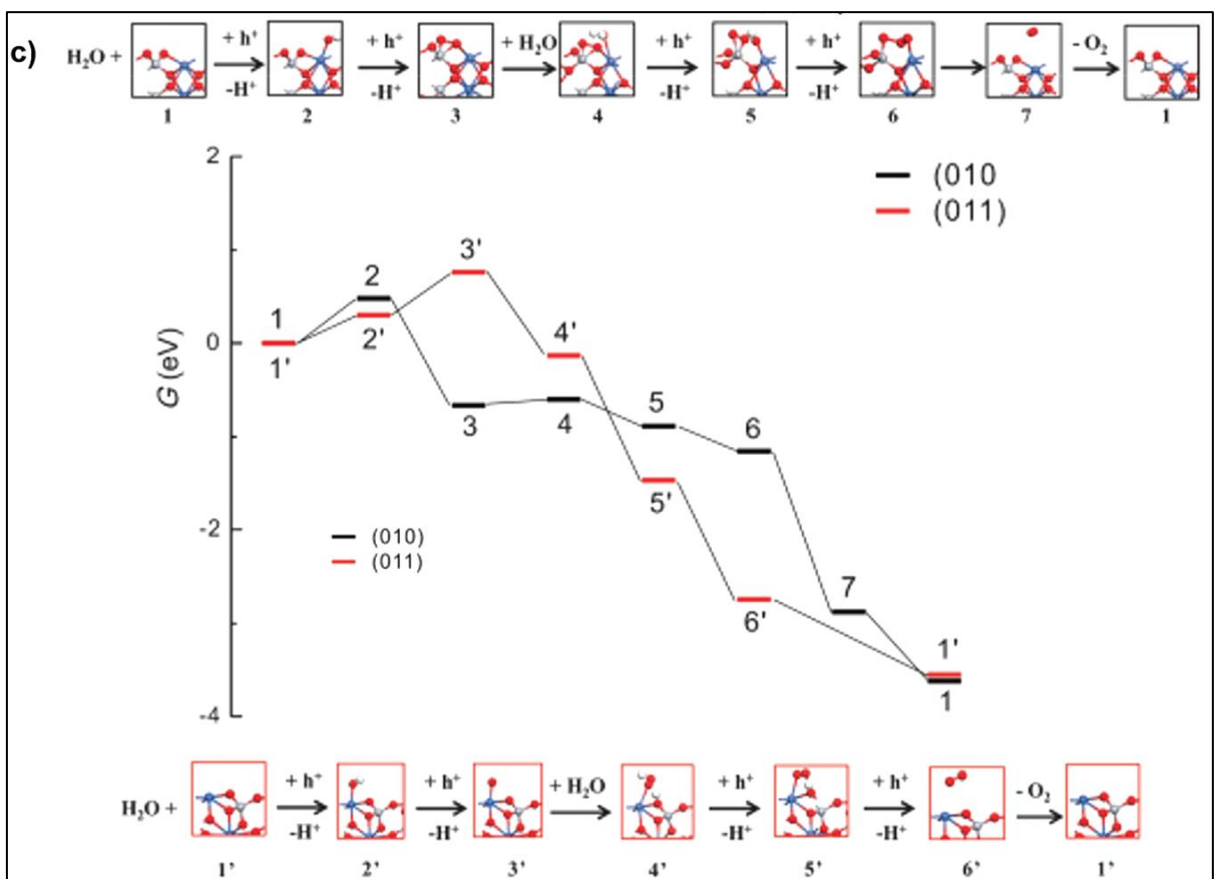


Fig 2.6: (c) Computed mechanism of facet-dependent photocatalytic oxygen evolution on BiVO_4 (reproduced from ref 56. Copyright 2013, John Wiley & Sons).

3. Morphology Control

Morphology control can not only facilitate mass transportation and light harvesting, but can also accelerate charge movement and assist the collection and separation of electron–hole pairs at the material interface [60-63]. Notable progress has been made in the synthesis of BiVO_4 with controlled morphologies (like nanorods, nanowires, nanotubes, nanobelts, nanoellipsoids, hollow spheres, and even some hierarchical architectures) and in investigations on the morphology dependent photocatalytic properties [64-71]. Tada et al. first fabricated BiVO_4 Nano rods (NRs) using polyethylene glycol (PEG) as a shape-directing agent [64]. Yu et al. applied a template-free solvothermal method to synthesize BiVO_4 nanotubes (NTs) [64]. Xie et al. reported a novel assembly-fusion strategy for the synthesis of BiVO_4 quantum tubes with an ultra-narrow diameter of 5 nm, ultrathin wall thickness down to 1 nm, and exposed {010} facets {Fig 2.8 (a) & (c)} [67] whose optical absorption edge and band energy are significantly blue-shifted with respect to bulk BiVO_4 , due to the quantum size confinement effect {Fig 2.8 (b)}. The self-assembly of nanosized building blocks, including nanowires, nanobelts, nanosheets, and nanotubes into hierarchical architectures has attracted great attention [60]. Liu et al. and Chen et al. synthesized BiVO_4 porous hollow microspheres composed of single-

crystalline nanosheets using a solvothermal- induced self-assembly {Fig2.9 (a) &(b)} [68-69].

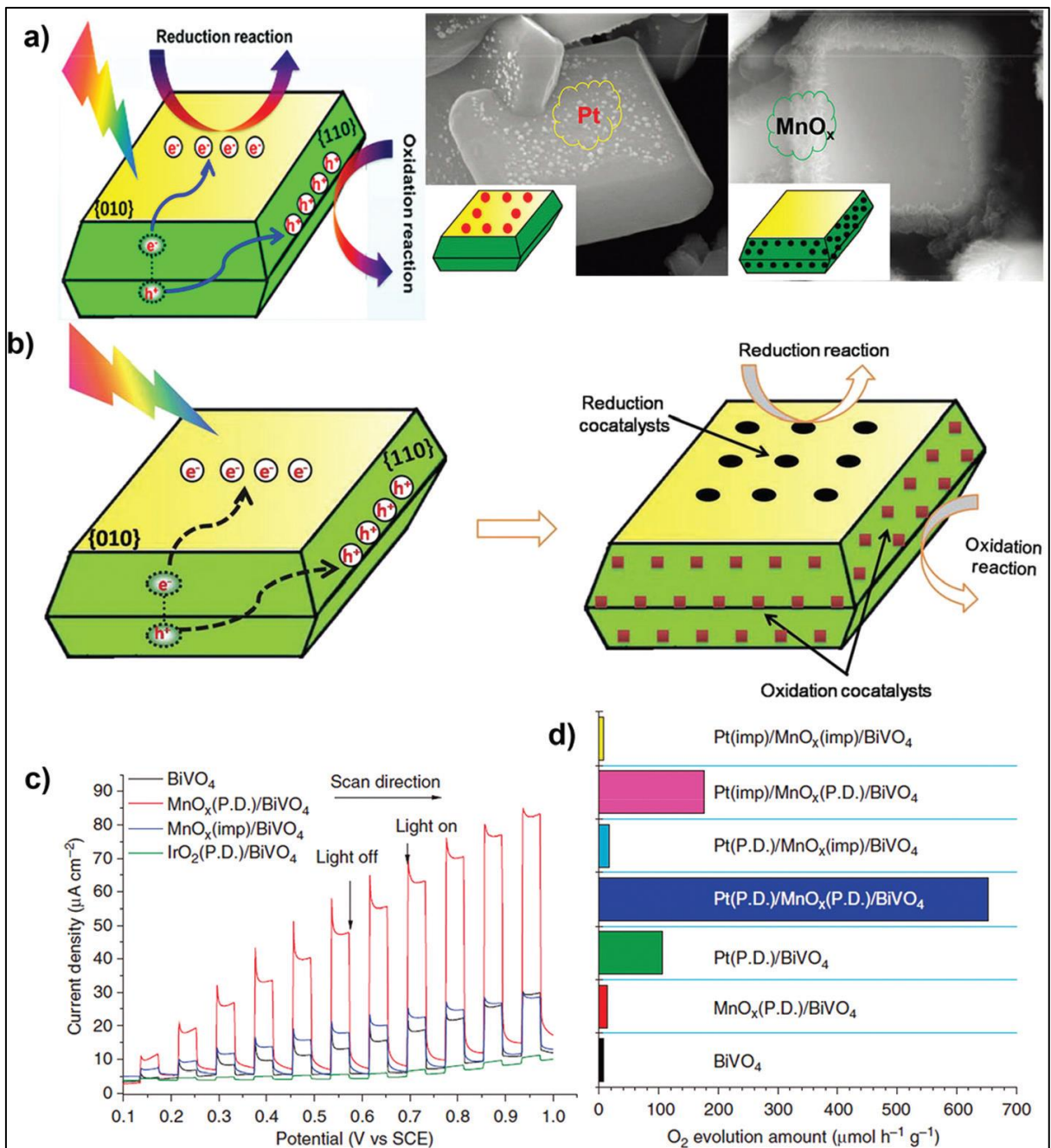


Fig 2.7: (a) Charge separation between the {010} and {110} facets confirmed by Pt and PbO₂ photo deposition on BiVO₄ (a, c, d reproduced from ref 58. Copyright 2013, Nature Publishing Group). (b) Selective deposition of dual redox co-catalysts on specific facets of BiVO₄ (reproduced from ref 59. Copyright 2014, Royal Society of Chemistry) (c, d) Photo electrocatalytic and photocatalytic water oxidation activity of BiVO₄ with selectively deposited co-catalysts on specific facets and randomly distributed co-catalysts.

These hollow microspheres exhibited excellent photocatalytic activity, due to the increase in specific surface area and light harvesting. Xie et al. also reported the multi-responsive function of ellipsoidal BiVO₄ assembled from many small nanoparticles exposed with {101} facets [70]. Similarly, Zhao et al. synthesized uniform hyper branched BiVO₄ via a surfactant-free hydrothermal route {Fig 2.9 (c)} [71]. The crystal consists of four trunks with branches distributed on opposite sides caused by the different growth rates along a, b, and c axes: preferentially along the [100] direction at the beginning, and subsequently along the [010] and [001] directions. The hyperbranched structure exhibits excellent photocatalytic activity, ascribed to its loosely packed building units because:

- ❖ The small crystal size allows for more efficient transportation of the electron–hole pairs generated inside the crystal to the surface
- ❖ The large surface area provides abundant active sites for the photocatalytic reaction and promotes light harvesting and reactant adsorption.

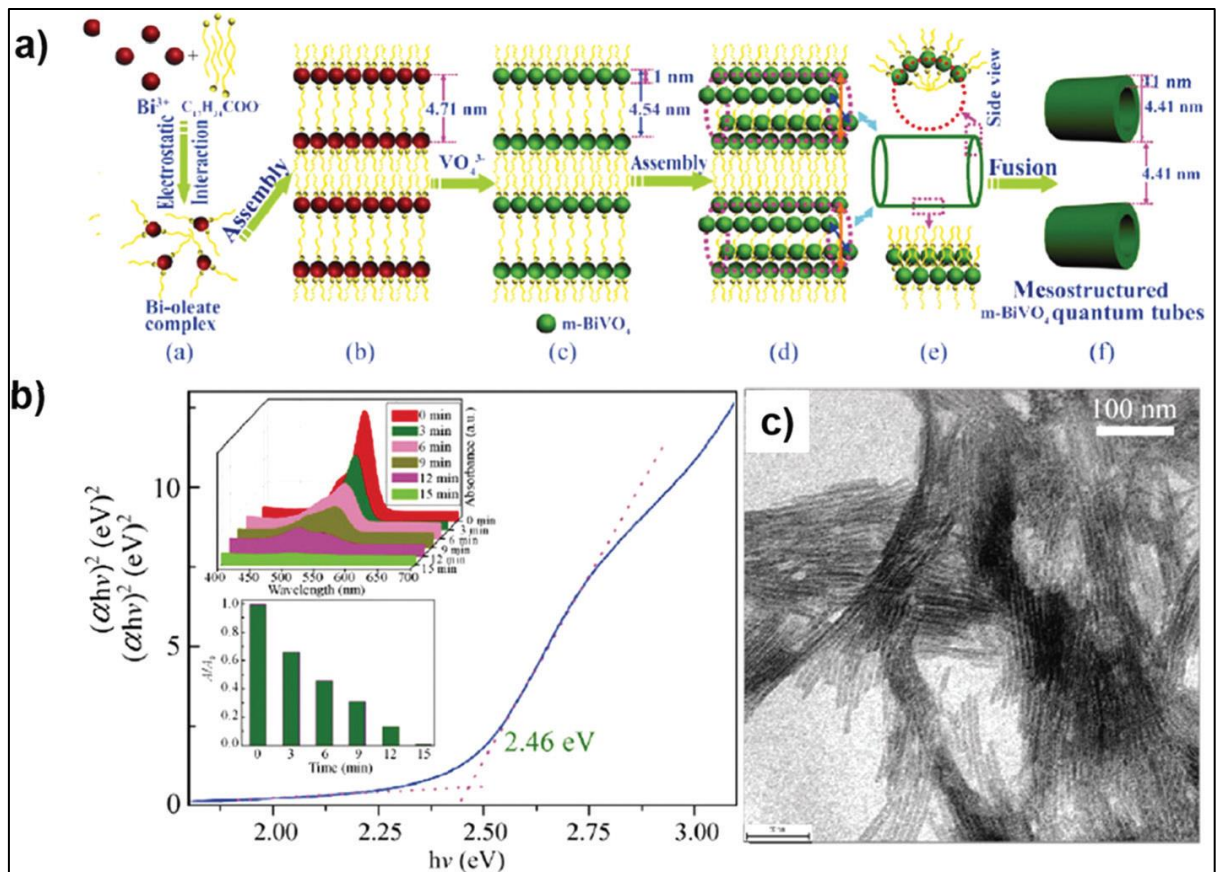


Fig 2.8: (a) Mechanism for the formation of BiVO₄ quantum tubes. (b) Optical absorption edge of BiVO₄ quantum tubes (top and bottom insets: photodegradation of RhB vs. irradiation time under visible light). (c) TEM image of BiVO₄ quantum tubes after the photodegradation (a-c reproduced from ref 67. Copyright 2010, Springer).

4. Macro / meso – porous structure

One of the main reasons for the charge recombination in BiVO₄ is the long diffusion length of the photo-induced electrons [72-74]. Tailoring porous BiVO₄, especially ordered porous structures, can shorten the diffusion length and thus facilitate charge migration, providing a readily access channel and increasing the adsorption of reactants and the supply of more surface active sites [74, 71].

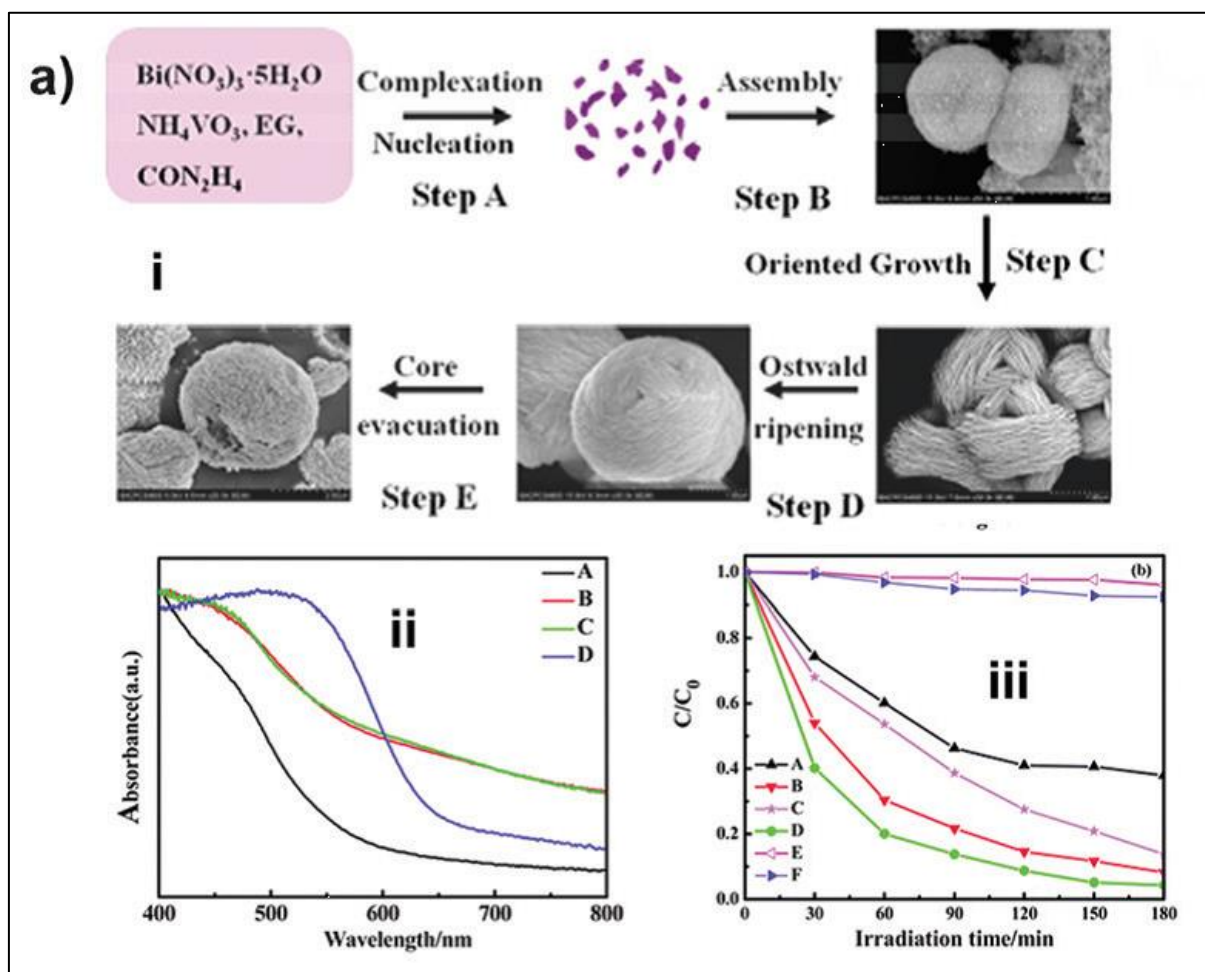


Fig 2.9: (a) Formation mechanism, UV-Vis absorption, and RhB photodegradation of hollow BiVO₄ microspheres (reproduced from ref 68. Copyright 2013, Royal Society of Chemistry).

Yu et al. reported that ordered mesoporous BiVO₄ fabricated by nanocasting using mesoporous silica KIT-6 as the replica parent template exhibited a higher photo activity than conventional BiVO₄ {Fig2.10 (a)} [71]. Xie et al. synthesized ordered macroporous BiVO₄ with controllable dualporosity for efficient solar water splitting and illustrated the relationship between the geometrical characteristics and the charge migration {Fig 2.10 (b)} [72]. The geometrical characteristics of periodically ordered macroporous structures are determined by two parameters {Fig2.10 (b) – i: the diameter of the macropores surrounded by the final skeletal walls (denoted as D₁), and second, the diameter of the pores between neighboring macropores (denoted as D₂)}. Previously, Lee et al. mentioned that the proper D₁ size leads to an efficient photo-induced charge drift mobility [75]. Xie et al. further synthesized ordered macroporous BiVO₄ architectures

with controllable dual porosity (aforementioned as D1 and D2) via a modified colloidal crystal templating method {Fig2.10 (b) –i and ii}, and verified that charge migration in periodically ordered macroporous architectures has a strong dependence on D1 and D2 {Fig2.10 (b) – iii} [76]. A smaller D2 is beneficial for charge migration, both in the bulk and on the surface; moreover, a smaller D1 facilitates only surface charge migration and hinders bulk charge migration.

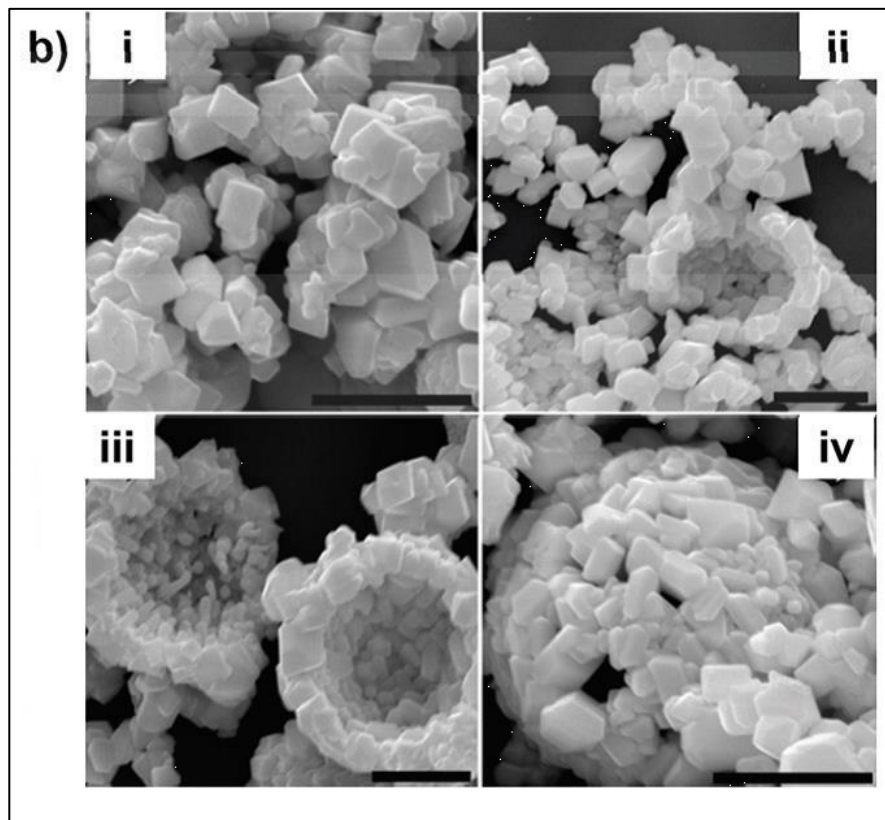


Fig 2.9: (b) Morphology evolution of BiVO₄ hollow spheres via a hydrothermal method using urea as the guiding surfactant (I: 2 h; II: 4 h; III: 8 h; IV: 12 h; V: 24 h; scale bar is 2 μ m) (reproduced from ref 78. Copyright 2013, Elsevier).

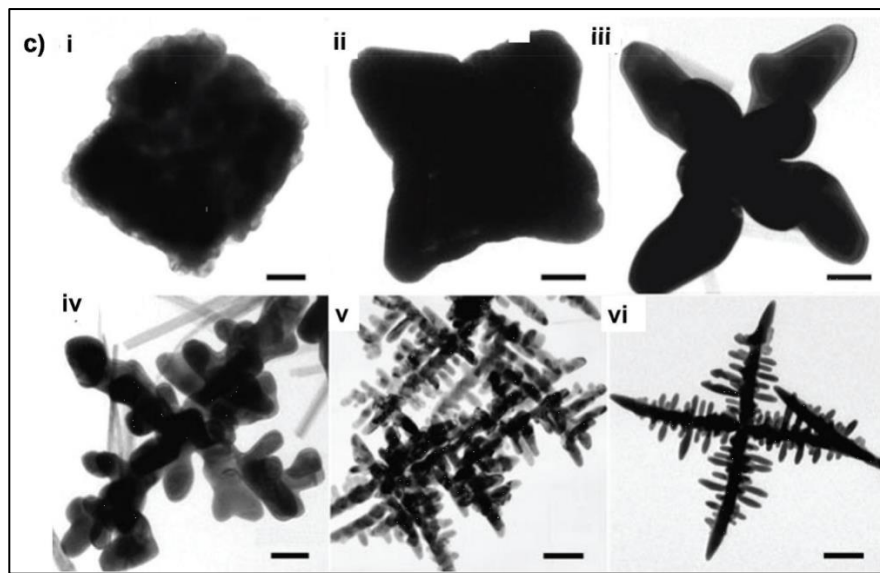


Fig 2.9: (c) Morphology evolution of hyperbranched BiVO₄ at intervals of 10 min (I), 20 min (II), 30 min (III), 45 min (IV), 1 h (V), and 3 h (VI), respectively (the scale bars are 100, 200, 200, 200, 400 and 500 nm, respectively) (reproduced from ref 79. Copyright 2008, John Wiley & Sons).

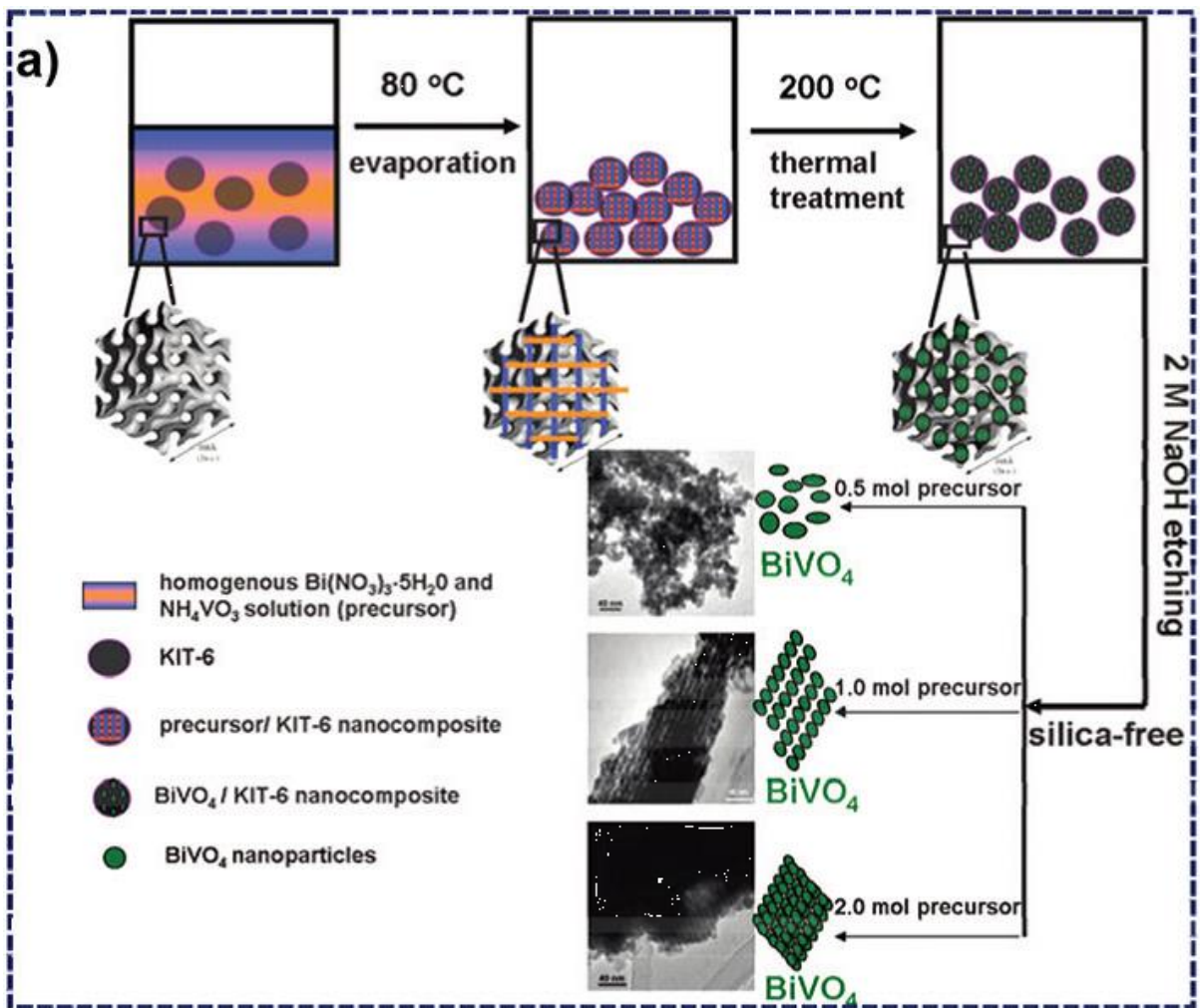


Fig 2.10: (a) Proposed process for the fabrication of ordered mesoporous BiVO_4 (reproduced from ref 81. Copyright 2008, American Chemical Society).

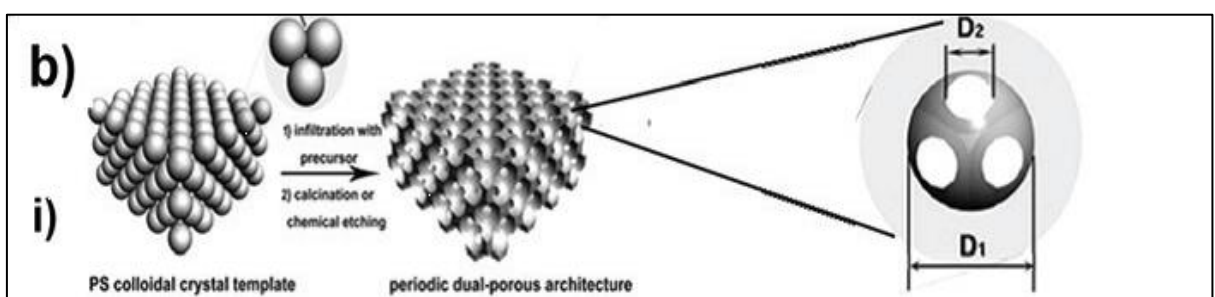


Fig 2.10: (b) (i) Schematic representation of dual porosity in periodically ordered porous BiVO_4

Diameter of PS sphere	Time of post-heating treatment for the template						
	S	M	L				
ii)	a	b	c				
	200 nm	200 nm	200 nm				
	d	e	f				
	420 nm	400 nm	400 nm				
	g	h	i				
	1000 nm	1000 nm	1000 nm				
	Sample	D1 [nm]	D2 [nm]	J @ 0.4 V/ mAcm ⁻² ^[a]	J @ 1.2 V/ mAcm ⁻² ^[a]	R _{ct} [Ω]	Photoelectron life- time @ 0.6 V/s ^[b]
	S-200	180	35 ± 5	0.38	1.35	268.7	2.01
iii)	M-200	170	85 ± 5	0.30	0.84	350.0	1.82
	L-200	155	105 ± 5	0.29	0.64	762.3	1.62
	S-1000	850	105 ± 5	0.25	0.80	1187	1.70
	M-1000	780	150 ± 5	0.22	0.65	1621	1.54
	L-1000	710	560 ± 5	0.13	0.55	2815	1.31

[a] The voltage is referenced to Ag/AgCl. [b] The voltage is referenced to RHE.

Fig 2.10: (b) (ii) typical SEM images of corresponding BiVO₄ (iii) relationship between PEC performance and dual porosity (reproduced from ref 80. Copyright 2013, John Wiley & Sons).

3. Rietveld Analysis

The Rietveld method refines user-selected parameters to minimize the difference between an experimental pattern (observed data) and a model based on the hypothesized crystal structure and instrumental parameters (calculated pattern). A full profile fitting system using crystallographic constraints (i.e. Lattice parameters and space group to constrain peak positions, Crystal structure to constrain peak intensities).

1. Least squares method - Curve fitting (Interpolation)

If data is reliable, it connects the dots piece – wise. Depicting the trend in the data variation by assigning a single function to represent the data across its entire range. A straight line function $f(x) = ax + b$ where the goal is to identify the coefficients ‘a’ and ‘b’ such that $f(x)$ ‘fits’ the data well.

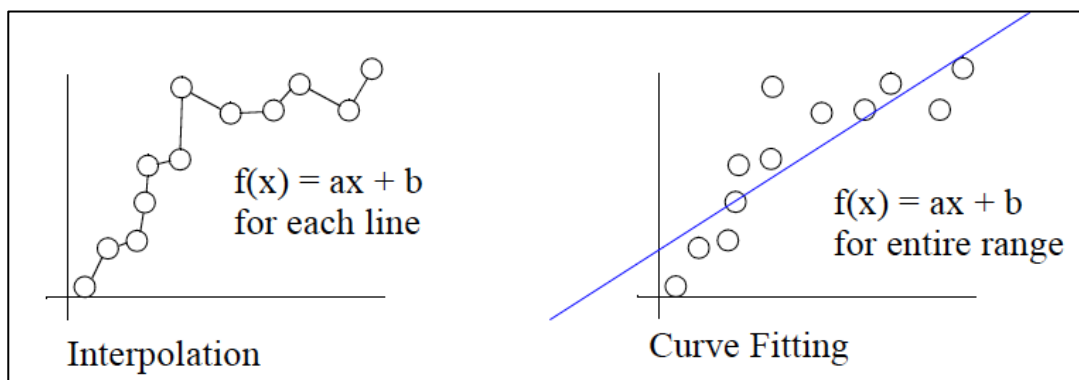


Fig 2.11: Interpolation

2. Linear Curve Fitting

A straight line function $f(x) = ax + b$. In order to pick the coefficients that best fits the line to the data, at first it has to be understood what makes a particular straight line a ‘good’ fit.

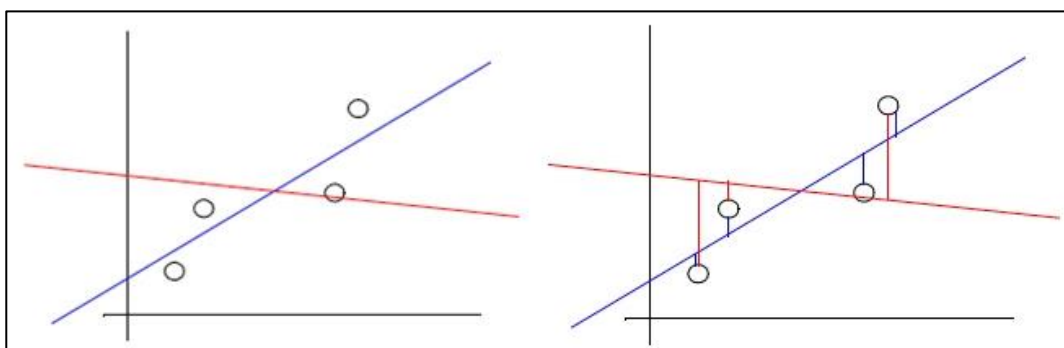


Fig 2.12: (a) Linear curve fitting or regression

Assumptions:

- Positive or negative error have the same value (data point is above or below the line)
- Weight greater errors more heavily

By squaring the distance and denote data values as (x, y) and points on the fitted line as $(x, f(x))$, sum the error at the four data points are calculated.

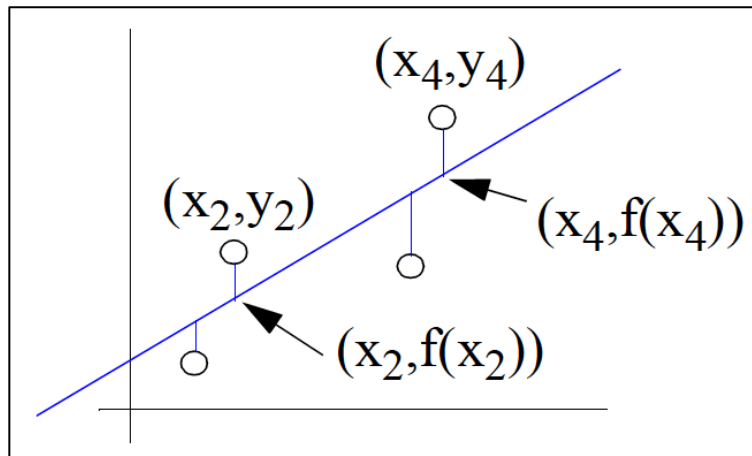


Fig 2.12: (b) Qualifying error in a curve fitting

$$\begin{aligned} \text{Error} &= \sum (d_i^2) = (y_1 - f(x_1))^2 + (y_2 - f(x_2))^2 + (y_3 - f(x_3))^2 + (y_4 - f(x_4))^2 \\ &= \sum_{i=1}^n (y_i - a(x_i) - b_i)^2 \end{aligned}$$

The ‘best’ line has minimum error between line and data points. This is called the least squares approach, since the square of the error has been minimized.

3. Nonlinear Curve Fitting

$$f(x) = a_0 + a_1 x + a_2 x^2 + a_3 x^3 + \dots + a_j x^j = a_0 + \sum_{k=1}^j a_k x^k$$

Just as was the case for linear regression, the coefficients that best fit the curve to the data have to be calculated. The curve that gives minimum error between data and the fit is ‘best’.

4. Fitting considerations

At first, a polynomial form at least several orders lower than the number of data points has to be selected. Then after starting with linear, orders are to be added until trends are matched.

Rietveld analysis is helpful for some reasons:

- Analysis of the whole diffraction pattern
 - Profile fitting is included
 - Not only the integrated intensities
- Refinement of the structure parameters from diffraction data
 - Quantitative phase analysis (crystalline and amorphous)
 - Lattice parameters
 - Atomic positions and occupancies
 - Temperature vibrations (isotropic and anisotropic)
- Other information
 - Grain size and micro micro-strain (isotropic and anisotropic)
 - Stacking and twin faults
 - Magnetic moments (neutrons)
- Not intended for the structure solution
 - The structure model must be known before starting the Rietveld refinement

5. Requirements for Rietveld Analysis

- ❖ High quality experimental diffraction pattern
- ❖ A structure model that makes physical and chemical sense
- ❖ Suitable peak and background functions

6. Principle of Rietveld analysis

The main principle is to calculate intensity at point i of the diagram:

$$y_{ic} = y_{ib} + \sum_{\Phi} S_{\Phi} \sum_k G_{\Phi}(2\theta_i - 2\theta_k) I_k$$

Where,

G = normalized profile shape function

I = intensity of the kth reflection

S = scale factor of phase Φ Summation performed over all phases Φ , and over all reflections k contributing to the respective point

Y_{ib} = background

7. Intensity of the Bragg reflections

$$I_k = m_k L_k |F_k|^2 P_k A_k$$

Where,

m_k = multiplicity of k

L_k = Lorentz-polarization factor

$|F_k|^2$ = structure factor

P_k = preferred orientation factor

A_k = absorption factor

The goal is the minimization of the residual function.

$$\sum_i w_i (y_i^{obs} - y_i^{calc})^2$$

where $w_i = 1/y_i^{obs}$

y_i^{obs} : observed intensity at the i^{th} step

y_i^{calc} : calculated intensity at the i^{th} step

$$I_i^{calc} = S_F \sum_{j=1}^{N\text{phases}} \frac{f_j}{V_j^2} \sum_{k=1}^{M\text{peaks}} L_k |F_{k,j}|^2 S_j (2\theta_i - 2\theta_{k,j}) P_{k,j} A_j + bkg_i$$

Scale Factor
 S_F : beam intensity
 f_j : volume fraction
 V_j : cell volume

Structure Factor
 Multiplicity of k-th reflection (m_k)
 Temperature factor

Lorentz-Polarization factor
 • Geometry
 • monochromator (angle θ)
 • Detector
 • beam size/sample volume
 • sample positioning (angular)

Preferred orientation
 i : steps
 j : number of phases
 k : k^{th} reflection

8. Quality of refinement

Quality of refinement strongly depends on some parameters which are:

- Weighted sum of squares

$$WSS = \sum_{i=1}^N \left[w_i (I_i^{\exp} - I_i^{calc}) \right]^2 \quad \text{where } w_i = \frac{1}{\sqrt{I_i^{\exp}}}$$

- R-structure factor

$$R_F = \frac{\sum \left| \left(I_K^{obs} \right)^{1/2} - \left(I_K^{calc} \right)^{1/2} \right|}{\sum \left(I_K^{obs} \right)^{1/2}}$$

- R-Bragg factor

$$R_B = \frac{\sum \left| I_K^{obs} - I_K^{calc} \right|}{\sum I_K^{obs}}$$

I_K : intensity of K^{th} reflection at the end of refinement cycles

- R - weighted pattern (R_{wp})

$$R_{wp} = \left[\frac{\sum w_i (y_i^{obs} - y_i^{calc})^2}{\sum w_i (y_i^{obs})^2} \right]^{1/2}$$

y_i : gross intensity at ith step

- Goodness of Fit (GoF) or χ^2

$$\chi^2 = \frac{R_{wp}}{R_{exp}}$$

$$R_{exp} = \left[(N - P) / \sum w_i (y_i^{obs})^2 \right]^{1/2}$$

N=number of points
P=number of parameters

9. Rietveld Analysis Procedure

- ❖ Gathering Information
 - The XRD pattern with which refinement will be compared. Basically it is the database file which are available in crystallographic open database website. (The .cif files have been downloaded from ref 82)
 - Preparing .dat file of Bragg reflection of the sample (.dat files were prepared for all four BVO samples in “2thetaI – Step – 2thetaF” format)
- ❖ Choosing appropriate program (Fullprof software was used in this research)
- ❖ Loading cif files or giving manually input the phases in the sample (direct cif file was loaded)
- ❖ Adjusting cell parameters manually (cell, intensities, background)
- ❖ Refining overall intensities and background
- ❖ Refining peaks positions
- ❖ Refining peaks shapes
- ❖ Refining structures
- ❖ Assessing the results (χ^2 value)

Chapter 3 Experimental

1. Introduction

BiVO₄ samples were prepared by a straight forward hydrothermal route. Since the formation of monoclinic BVO completely depends on the synthesis parameters and perfection, it is very important to use high purity raw materials. It is one of the most important facts to be careful always so that no impurity gets mixed with the raw materials, otherwise no better synthesis process and perfection of synthesis can achieve the desired values. Accurate weight calculation and sample measurements are also some major important issues. After sample preparation, characterization and property measurements were carried out and finally some conclusions can be drawn. During all measurements, from sample preparation to property measurements, all parameters must be maintained for getting good results.

2. Raw Materials

Table 1 Information of raw materials

Elements	Atomic Number	Atomic Weight	Molecular Weight	Density (gm/cm ³)
Bi	83	208.98	-	9.79
V	23	50.9515	-	6
O	8	15.999	-	1.429
K	19	39.09	-	0.856
S	16	32.065	-	1.96
N	7	14.006	-	1.251
Mn	25	54.938	-	7.47
Nd	60	144.24	-	7.01
Bi(NO ₃) ₃ .5H ₂ O	-	-	484.98	2.90
V ₂ O ₅	-	-	181.9	3.36
K ₂ SO ₄	-	-	174	2.66
Nd ₂ O ₅	-	-	368.48	4.6
Mn(NO ₃) ₂ .4H ₂ O	-	-	250.938	1.82

Table 2: Preparative parameters of synthesized samples of BiVO₄

Sample No	Sample	Precursor	Molar Amount	Weight	Temperature
BVO S1	BiVO ₄	Bi(NO ₃) ₃ .5H ₂ O V ₂ O ₅ H ₂ O	0.2 mmol 0.2 mmol	97 mg 36.38 mg 10 mL	200 °C
BVO S2	BiVO ₄	Bi(NO ₃) ₃ .5H ₂ O V ₂ O ₅ K ₂ SO ₄ H ₂ O	0.2 mmol 0.2 mmol 5.7 mmol	97 mg 36.38 mg 1 gm 10 mL	200 °C
BVO S3	Bi _{0.9} Nd _{0.1} VO ₄	Bi(NO ₃) ₃ .5H ₂ O Nd ₂ O ₅ V ₂ O ₅ K ₂ SO ₄ H ₂ O	0.18 mmol 0.01 mmol 0.2 mmol 5.7 mmol	87.3 mg 3.68 mg 36.38 mg 1 gm 10 mL	200 °C
BVO S4	BiV _{0.9} Mn _{0.1} O ₄	Bi(NO ₃) ₃ .5H ₂ O V ₂ O ₅ Mn(NO ₃) ₂ .4H ₂ O K ₂ SO ₄ H ₂ O	0.2 mmol 0.18 mmol 0.01 mmol 5.7 mmol	97 mg 32.742 mg 25.101 mg 1 gm 10 mL	200 °C

3. Synthesis Process:

1. Measurements

At first, raw materials were weighed and taken carefully without any contamination of the raw materials by electronic mass balance (CSC Balance, model: JF2204).

2. Heating & Stirring

In a typical procedure, Bismuth nitrate pentahydrate and V₂O₅ were carefully measured and taken in beaker with 10 mL deionized water. Bismuth precursor are soluble in water at room temperature but V₂O₅ is insoluble in water at room temperature.

For this reason the beaker were placed on a heating plate (model: CORNING PC-420D). The beaker is kept on the plate for around 5 – 10 minutes at 50°C and magnetic stirring was done at 350 rpm. The heating was stopped just before the solution started to volatilize. This must be done with extreme caution because a slight amount of volatilization may cause unrecoverable loss of raw materials from the solution. This heating was done only to dissolve V₂O₅ in water. Initially the solution was brownish.

This is the typical initial process in which BVO S1 was prepared. For other samples, K₂SO₄ was also measured along with the bismuth and vanadium precursors and mixed in to water. For BVO S3 and BVO S4 the calculation of % doping materials' precursors have to be done precisely.

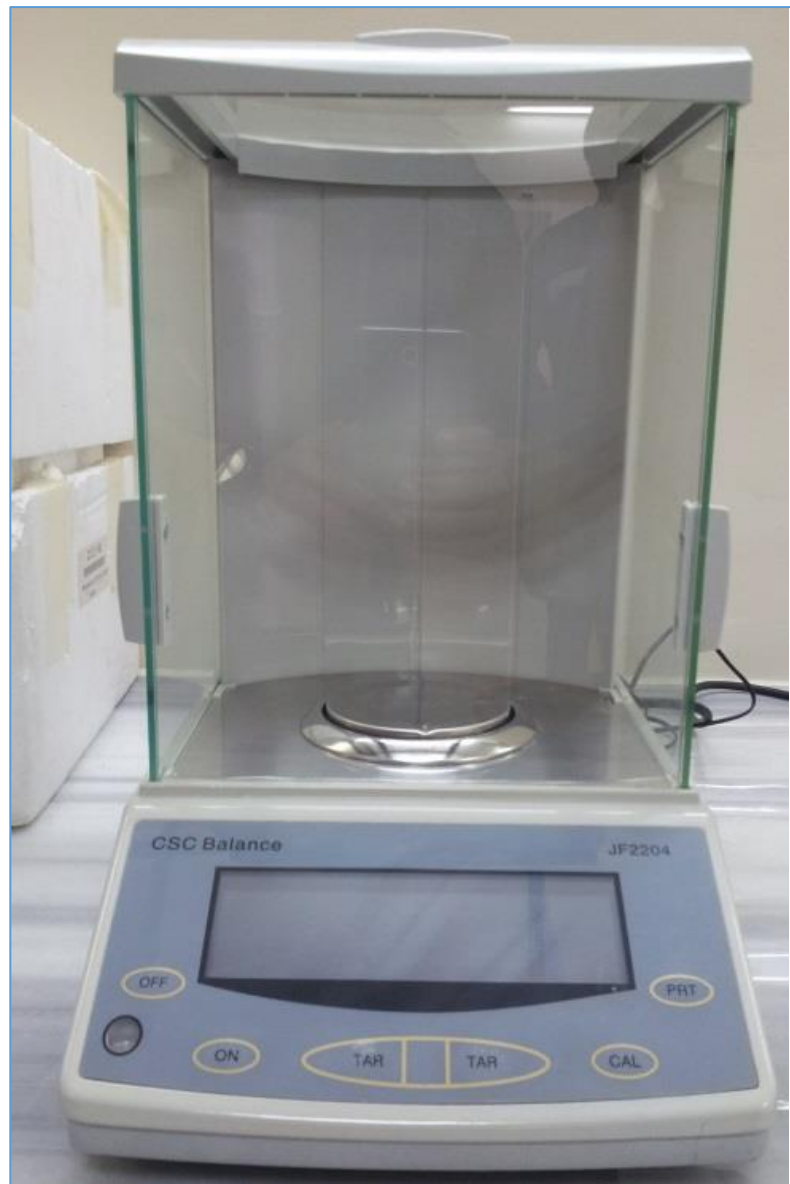


Fig 3.1: Electronic mass balance (CSC Balance, model: JF2204)



Fig 3.2: Nabertherm High Temperature Furnace (model: HT 16/18).

3. Heating in autoclave

After the heating and stirring the solution was then placed in stainless steel protected Teflon-lined autoclave to perform hydrothermal synthesis. Before putting the autoclave in to the furnace, several checking have to be done to ensure its locking. Then the autoclave was kept inside the furnace for 24 hour at 200 °C.



Fig 3.3: Teflon lined stainless steel autoclave

4. Centrifugation

After 24 hour heating at 200 °C, the solution was collected from autoclave. The synthesized nanoparticles were almost differentiable from the water. But for good results and noiseless XRD pattern, the particles should be washed in order to remove the nano level impurity from particle surface. So, centrifugation was used at 3500 – 4000 rpm.



Fig 3.4: Laboratory centrifuge machine

After centrifugation nanoparticles were collected and dried for 5 minutes in heating oven. Then these powders were kept for characterization.

4. Characterization

1. Phase Study

The phases were identified by powder X-ray diffraction (XRD) using Cu-K α radiation (model D8 Advance, Burker AXS). The high-intensity X-ray beam was focused on the sample in the scanning range from 10° to 70°. Cu-K α 1 radiation with wavelength of 0.154060 nm was used for the inspection.



Fig 3.5: X – Ray Diffractometer

X – Rays are type of electromagnetic radiation. The wavelength of X – Rays is approximately 1 \AA° which has the same size equivalent to that of an atom. X – Ray diffraction is a non – destructive analytical method mainly used for the phase identification and structural characterization of crystalline materials. X – Ray diffraction combined with Rietveld analysis, provides detailed information regarding unit cell dimensions, bond lengths, bond angles and the site ordering of crystallites.

$$2 d_{hkl} \sin q = n \lambda \quad \text{--- --- --- --- (1)}$$

After characterization by X – Ray diffraction, a number of peaks are seen in diffraction patterns. These patterns are identified by Rietveld analysis compared with pure monoclinic scheelite BVO, pure tetragonal scheelite BVO, pure tetragonal zircon type BVO and pure monoclinic Bi_2O_3 phases.

2. UV – Vis Spectroscopy

The optical bandgap energies of the synthesized samples were measured from diffused reflectance spectra using a UV-Vis spectrometer (UV/Vis/NIR – Lambda 1050, PerkinElmer, USA).



Fig 3.6: UV-Vis spectrometer (UV/Vis/NIR – Lambda 1050, PerkinElmer, USA).

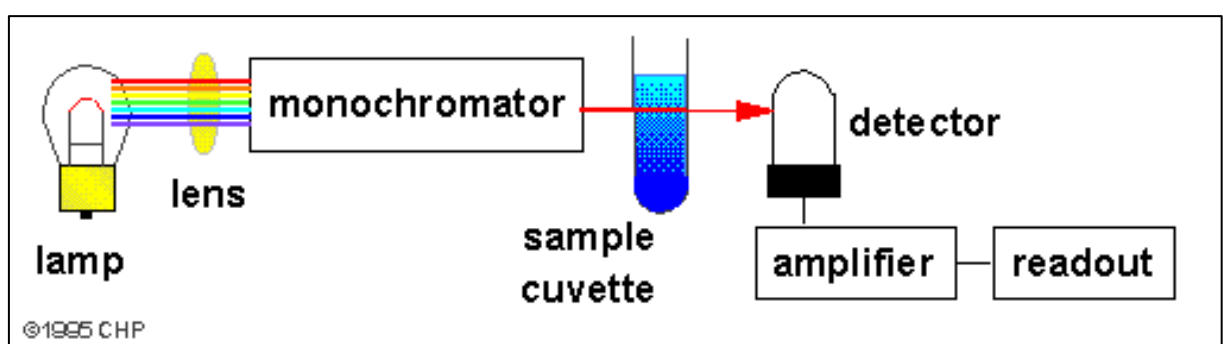


Fig 3.7: Schematic of a single beam UV – Vis Spectrophotometer

3. Microstructure Study

To observe the grain size and morphology of the samples, Field Emission Scanning Electron Microscope [FESEM: JEOL JSM 7600F] was used, with accelerating voltage of 5 kV. The microscopies were carried out on annealed powder sample. Prior to insertion in the FESEM, the samples were dispersed in ethanol by an ultrasonic probe.



Fig 3.8: Field Emission Scanning Electron Microscope [FESEM: JEOL JSM 7600F].

Chapter 4 Results and discussions

1. Phase Study

Fig 4.1 (a) shows the XRD patterns of BiVO₄ samples (Sample ID: BVO S1 & BVO S2) at room temperature. In BVO S1, significant amount of tetragonal zircon type BiVO₄ phase and some monoclinic Bi₂O₃ phase are present along with monoclinic BiVO₄ phase. Addition of K₂SO₄ has reduced this % tetragonal zircon type BiVO₄ phase and impurity (Bi₂O₃) in BVO S2.

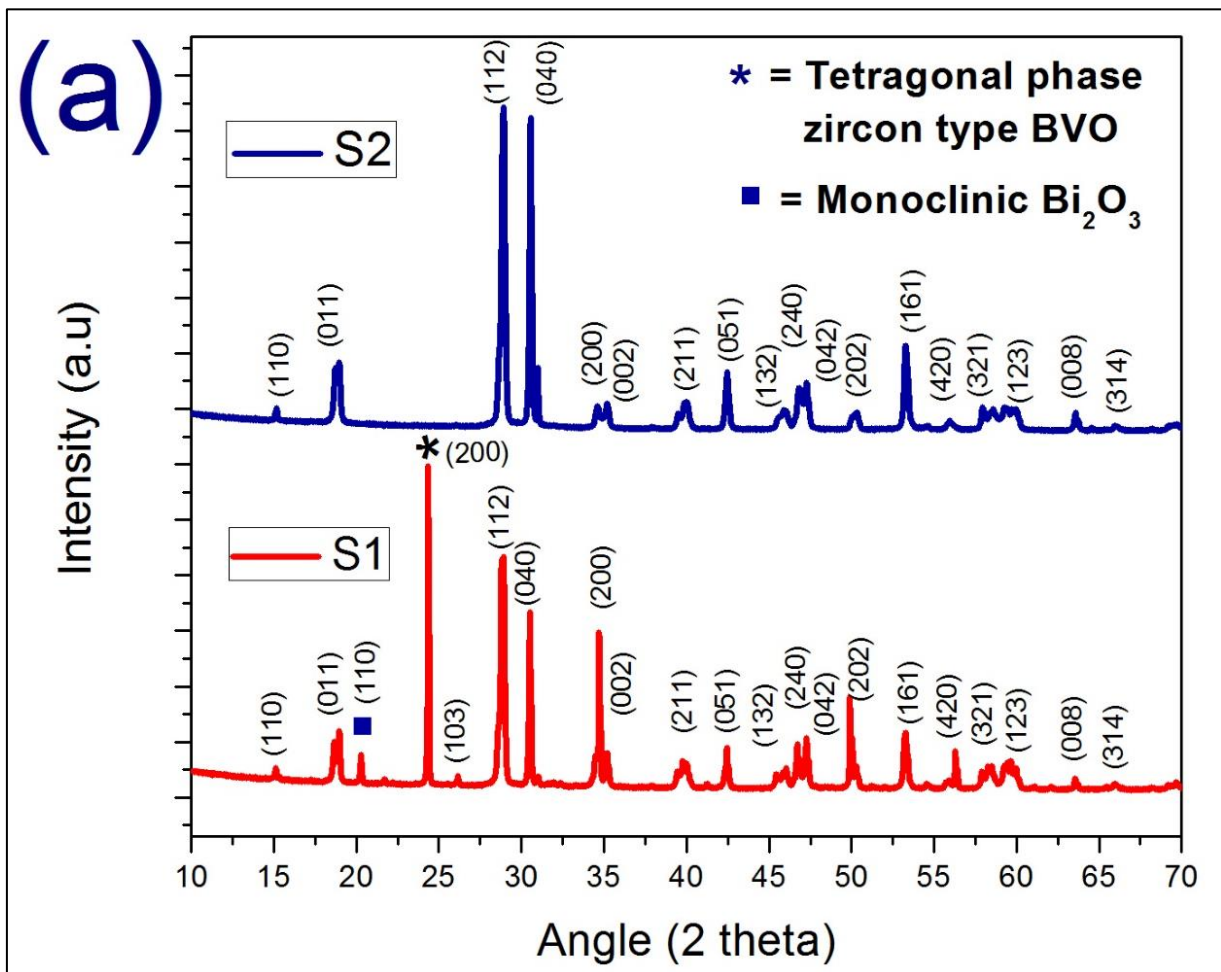


Fig 4.1(a): PXRD patters of BVO S1 and BVO S2 at room temperature.

Peak positions at 2 theta = 24.5, 35 and 46.5 degrees indicates the formation of BVO S1. Again, splitting of peaks at 18.5, 35 and 46.5 degrees are the confirmation of the presence of monoclinic BiVO₄ phase. In BVO S1, it can be seen that, splitting has been slightly occurred at 18.5 and 35 degrees but at 46.5 degree splitting is strong. Again, Bragg

reflection at 24.5 degree strongly shows the presence of tetragonal zircon type BiVO_4 phase in BVO S1. However, splitting of Bragg reflections at the above three mentioned positions is the characteristic identification of the formation of monoclinic BiVO_4 phase. So, it can be said that, in BVO S1 both monoclinic and tetragonal zircon type BiVO_4 phases are present. But, how much dominant are the two phases over each other cannot be concluded from here. Rietveld analysis [A1] answers this curiosity in a well-defined manner which will be discussed later in this section.

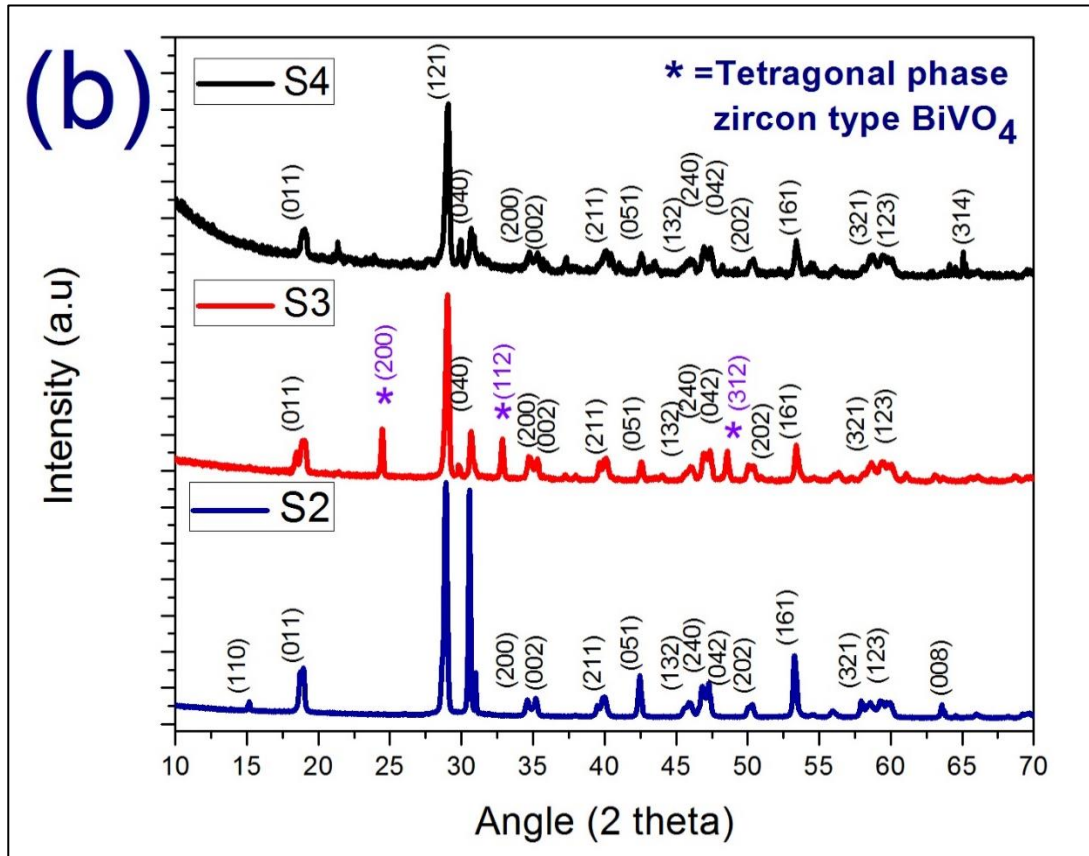


Fig 4.1(b): PXRD patters of BVO S2, BVO S3 and BVO S4 at room temperature.

Similarly, from Fig 4.1 (a) it can easily detectable that formation of tetragonal BiVO_4 phase has been suppressed by the monoclinic phase. Strong splitting of Bragg reflection at 18.5, 35 and 46.5 degrees and the absence of characteristic Bragg reflection of tetragonal zircon type BiVO_4 phase at 24.5 degree are the clear identification in BVO S2 PXRD pattern.

2. Rietveld Analysis

1. Confirmation of dual phase

Fig 4.2 (a), (b), (c) & (d) show the Bragg reflections for pure monoclinic, pure tetragonal (scheelite), pure tetragonal (zircon type) BVO and pure monoclinic Bi_2O_3 phases respectively.

From Fig 4.1, only the presence of dual phase of BVO (monoclinic and tetragonal zircon type) and impurity can be confirmed. But detailed confirmation cannot be concluded from here. So, in Rietveld refinement, comparison between pure phase of monoclinic BVO and samples' PXRD pattern will be sketched in details so that the Bragg reflections for each phase can be identified easily.

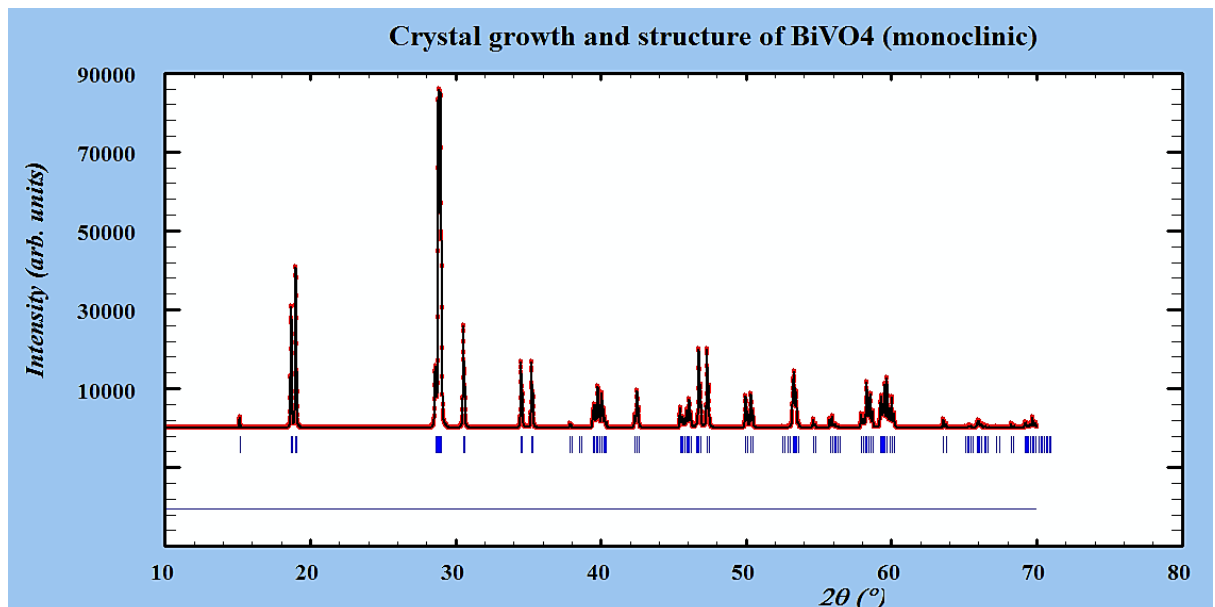


Fig 4.2 (a): Bragg reflections for pure monoclinic BVO

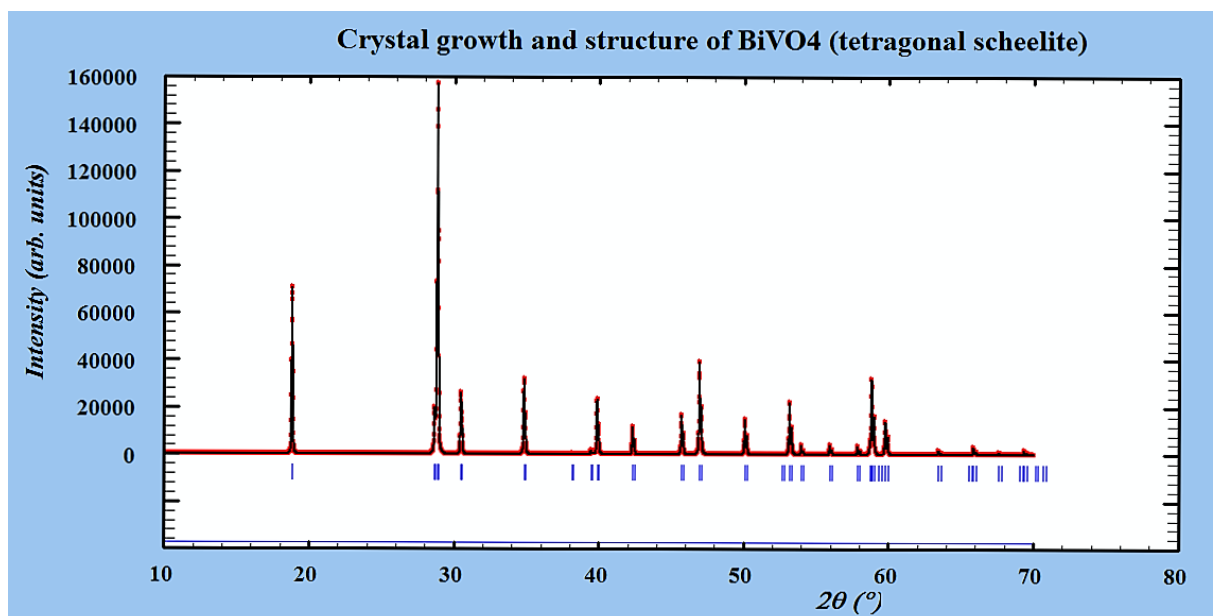


Fig 4.2 (b): Bragg reflections for pure tetragonal scheelite BVO

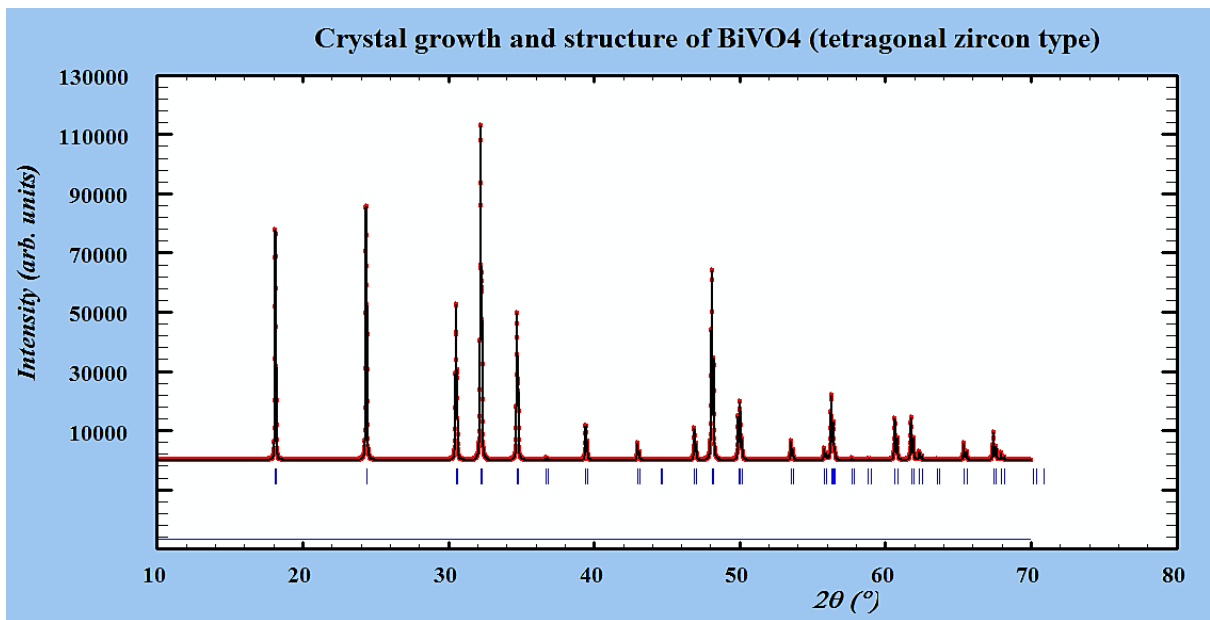


Fig 4.2 (c): Bragg reflections for pure tetragonal zircon type BVO

From Fig 4.2 (b) and (c) it is clear that, the tetragonal phase formed in sample BVO S1 and BVO S2 is **tetragonal zircon type**.

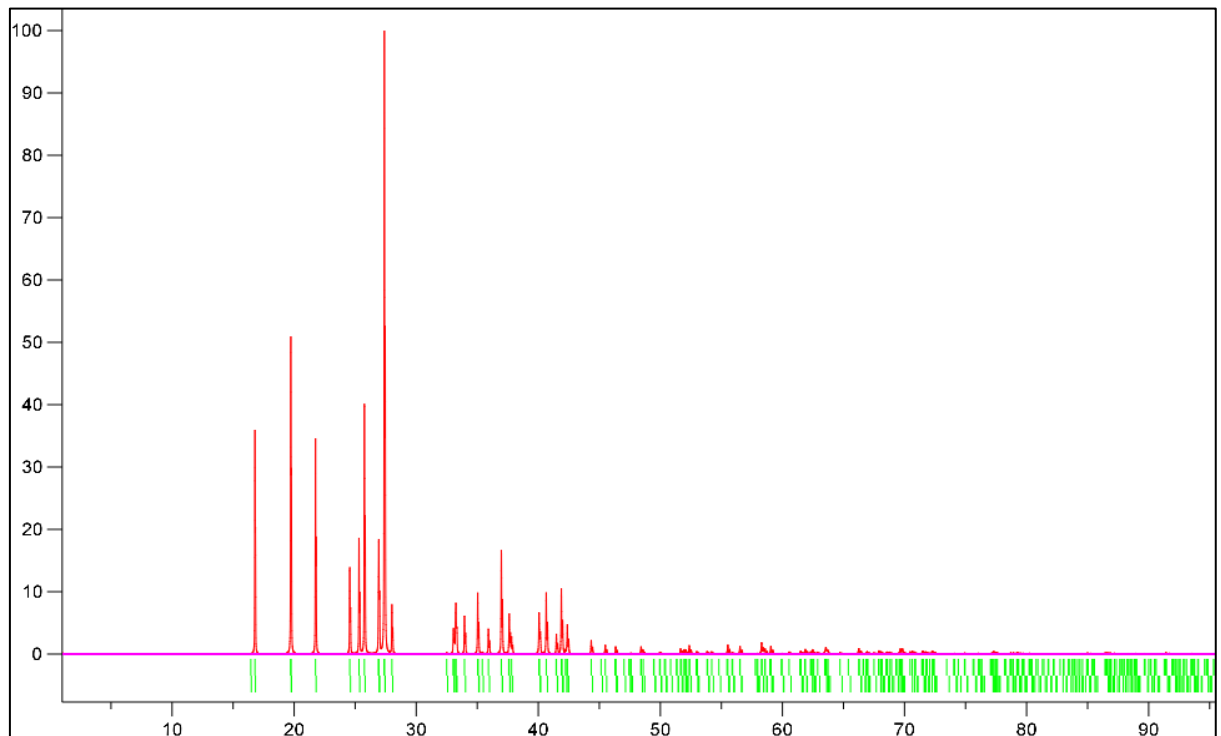


Fig 4.2 (d): Bragg reflections for pure monoclinic Bi₂O₃

2. Reason of formation of tetragonal zircon type BVO

Previous studies say that low temperature synthesis always tends to form zircon type BVO [13-22 chemical review]. If temperature is raised more, irreversible transformation of phases from zircon type tetragonal to monoclinic scheelite BVO will take place at 670-770 K. However, if temperature is kept increasing, reversible transformation of monoclinic scheelite BVO to tetragonal scheelite BVO will take place. Hydrothermal synthesis process plays an interesting role here. Because in hydrothermal synthesis pressure is increased by a greater value in autoclave which is well protected. So, due to increase in the pressure, that irreversible transformation of zircon type BVO to monoclinic scheelite BVO takes place at comparatively low temperature. In our hydrothermal synthesis process, temperature was 373K for all four samples and this low temperature synthesis is one of the most important features of hydrothermal synthesis route. So, it is clear that in our samples, zircon type tetragonal phase has been formed due to low temperature synthesis (373 K) and this is confirmed by the comparison of their pure PXRD pattern which has been shown in Fig 4.2 (b) and (c).

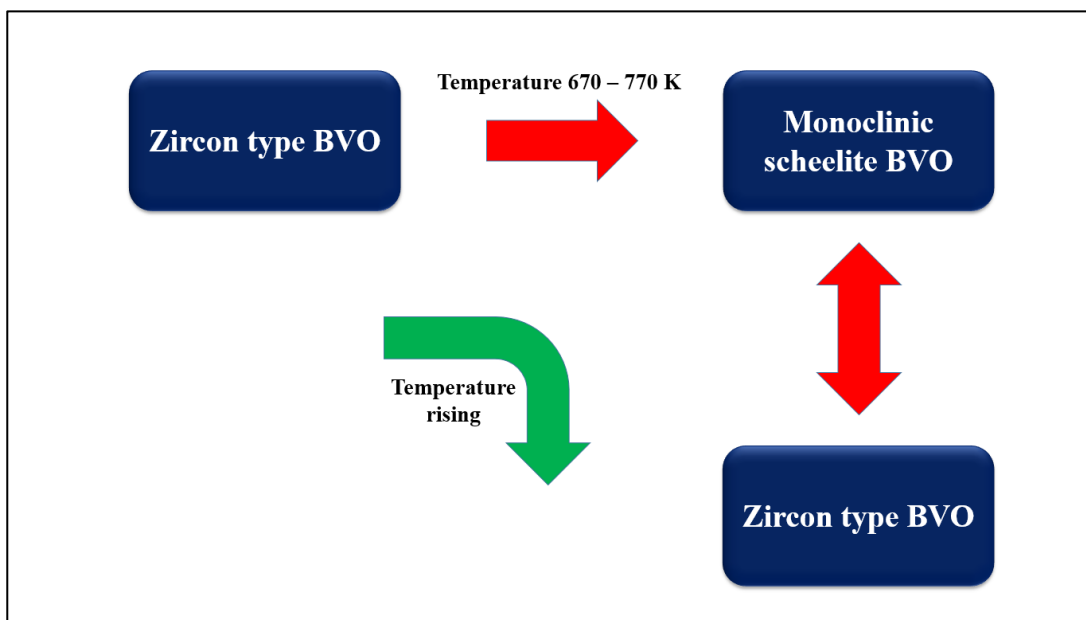


Fig 4.3: Transformation of phases of BVO with temperature

3. Rietveld refinement of BVO S1

From Fig 4.1 and 4.2, it can be seen that monoclinic BVO phase is strongly dominating in BVO S2 & BVO S4 and less dominating in BVO S1 & BVO S3. So, rietveld refinement has been done with only with the monoclinic BVO phase so that after refinement the unmatched Bragg reflections can be identified accurately. If so, comparing with these unmatched Bragg reflections with pure tetragonal phase we can identify any remaining phases like impurities along with the presence of tetragonal zircon type BVO.

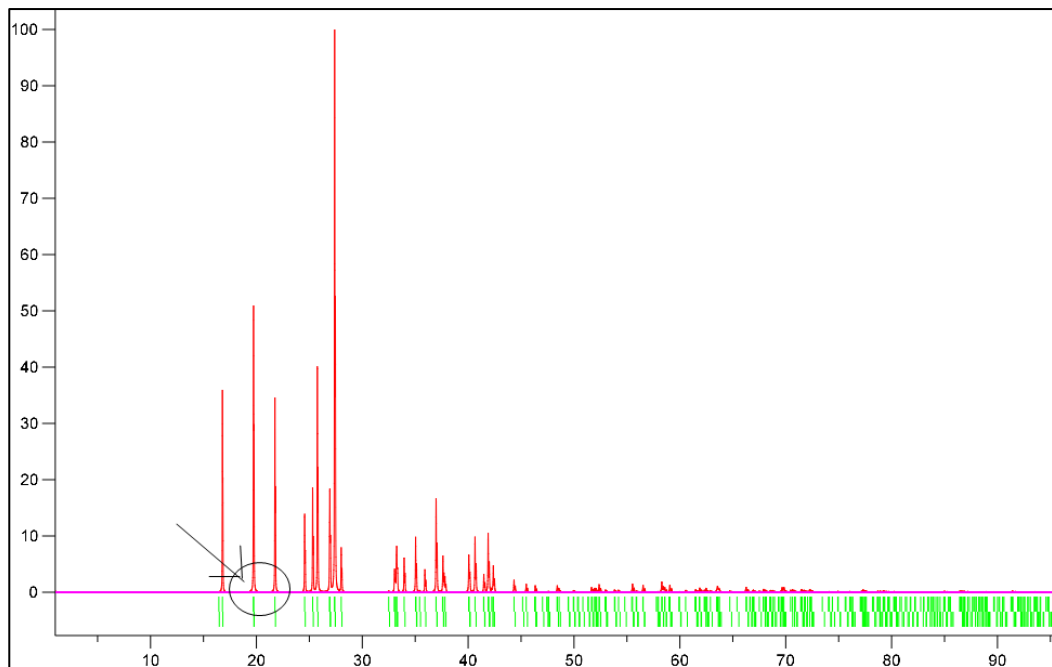


Fig 4.4: Identification of Bi_2O_3 phase which has been found in BVO S1

So, in our first refinement, Chi square goodness of fit test gives $\chi^2 = 16.6$ which is acceptable as the refinement has been performed for only pure monoclinic BVO phase. In fig 4.5 (a), Bragg reflections marked by green circles are the unmatched reflections with pure monoclinic BVO. In fig 4.5 (b), the unmatched Bragg reflections are accurately matched with reflections at 24.5, 31, 35, 50 and 57 degrees. Only the Bragg reflection at 20.5 remained unmatched with both monoclinic and tetragonal zircon type BVO phases which has been shown in fig 4.4.

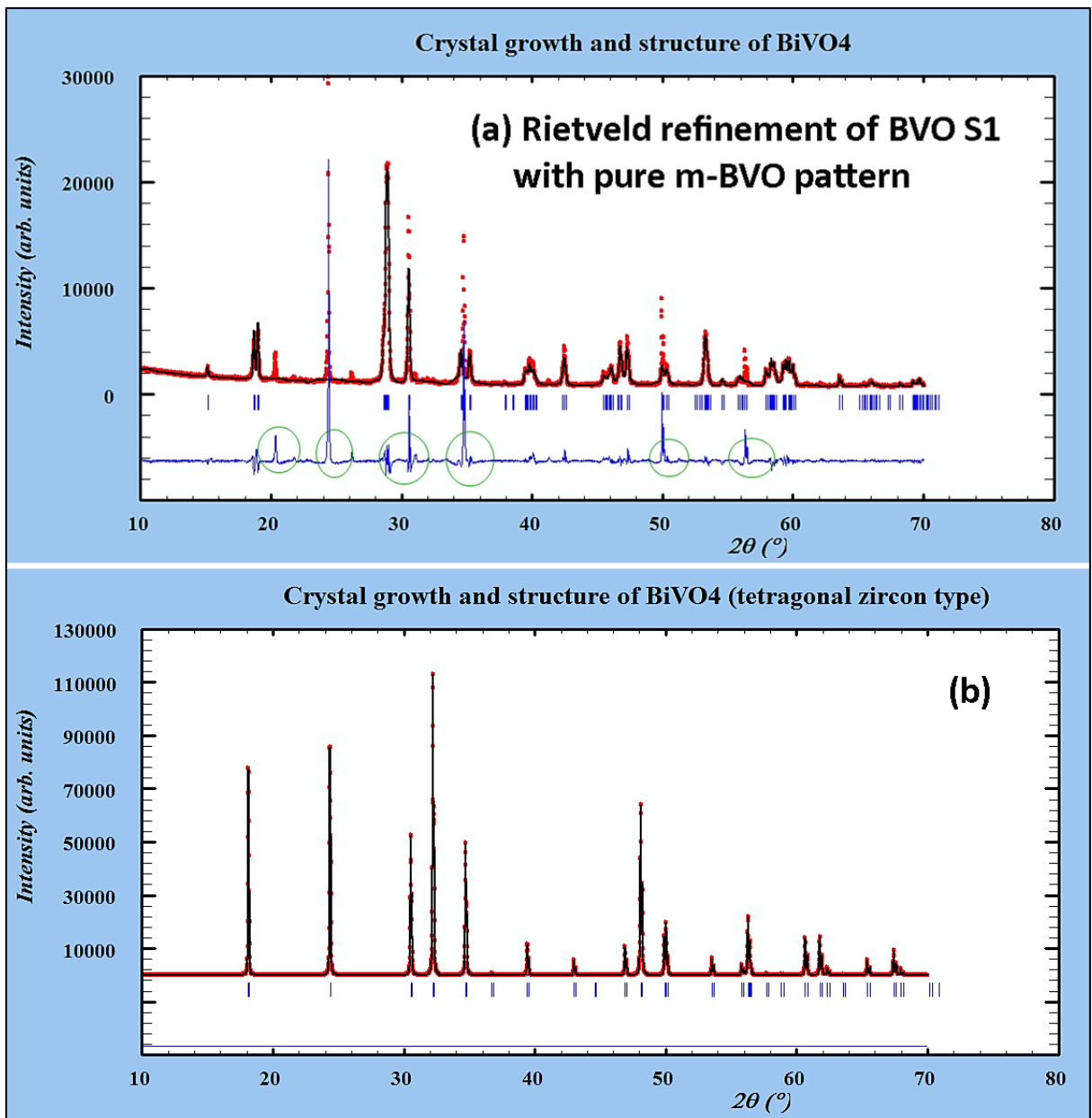


Fig 4.5 (a): Rietveld refinement of BVO S1 with pure m-BVO pattern (Green circles indicate the unmatched Bragg reflections) (b) PXRD pattern of pure tetragonal zircon type BVO

Refinement values and cell parameter values have been given in Table 1 and Table 2 respectively.

4. Rietveld refinement of BVO S2

In fig 4.6 (a) rietveld refinement shows us that dominance of monoclinic BVO phase over tetragonal zircon type BVO is true for the addition of K₂SO₄. The absence of characteristic peak of zircon type BVO at 24.5 is clearly detectable after refining with the pure monoclinic BVO phase. The χ^2 value is 16 which acceptable. There are no single unmatched Bragg reflections but slight mismatching at 31 degree confirms a small % of tetragonal zircon type BVO has been formed in BVO S2.

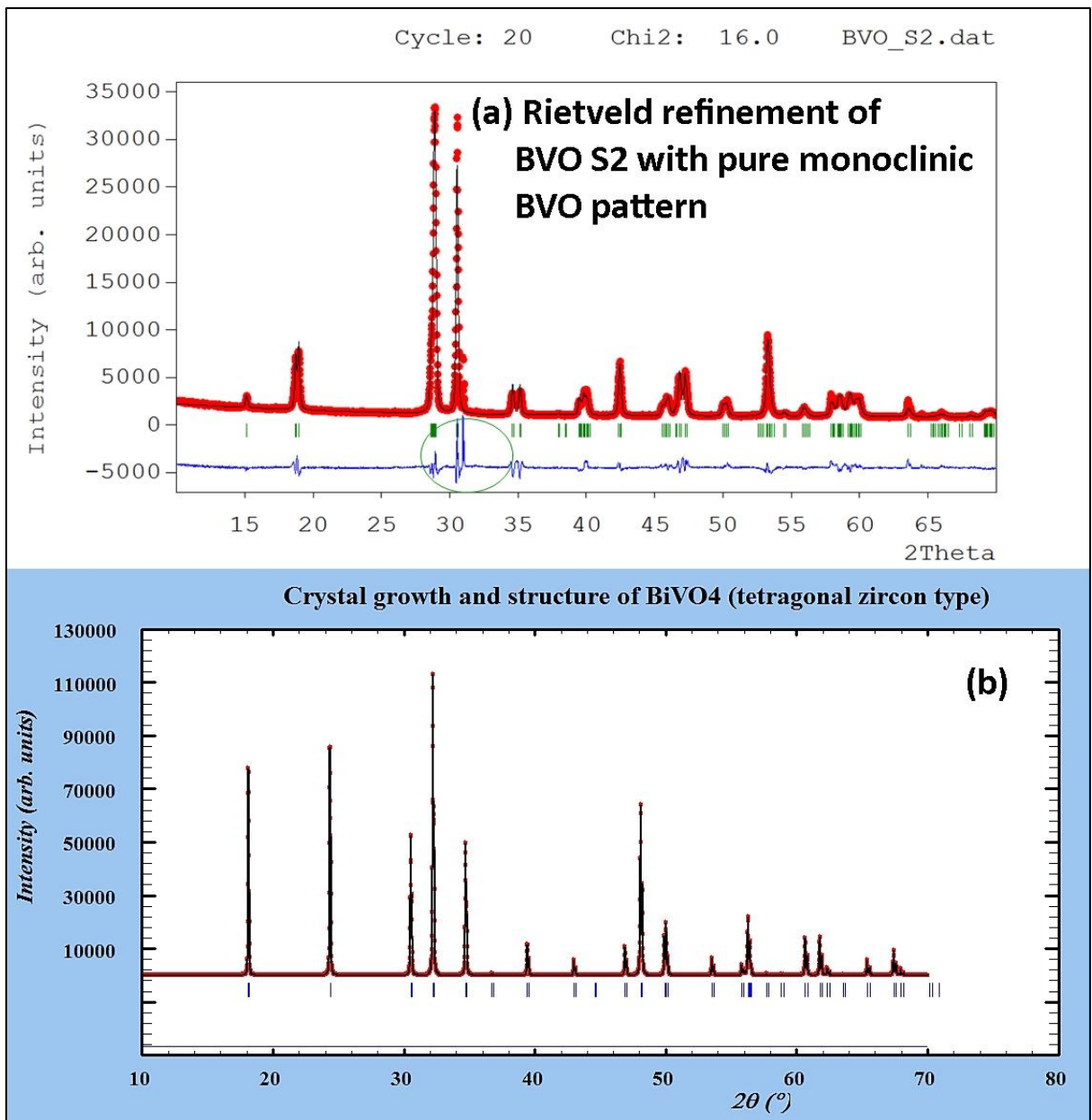


Fig 4.6 (a): Rietveld refinement of BVO S2 with pure monoclinic BVO pattern (Green circle indicates the unmatched Bragg reflection which is identified as tetragonal zircon BVO)

(b) Pure tetragonal zircon type BVO pattern

5. Rietveld refinement of BVO S3

Fig 4.7 (a) shows the rietveld refinement of BVO S3 in which 10% Nd is doped at Bi³⁺ sites. Though K₂SO₄ is present, formation of tetragonal zircon type BVO phase is confirmed by the unmatched Bragg reflections at 24.5, 33.5 and 48.5 degrees which are matched with the Bragg reflections of pure tetragonal zircon type BVO phase shown in fig 4.7 (b). No unmatched reflections have been found.

So, it is confirmed that after 10% Nd doping, % tetragonal phase has been increased. The effect of doping will be discussed later in this chapter.

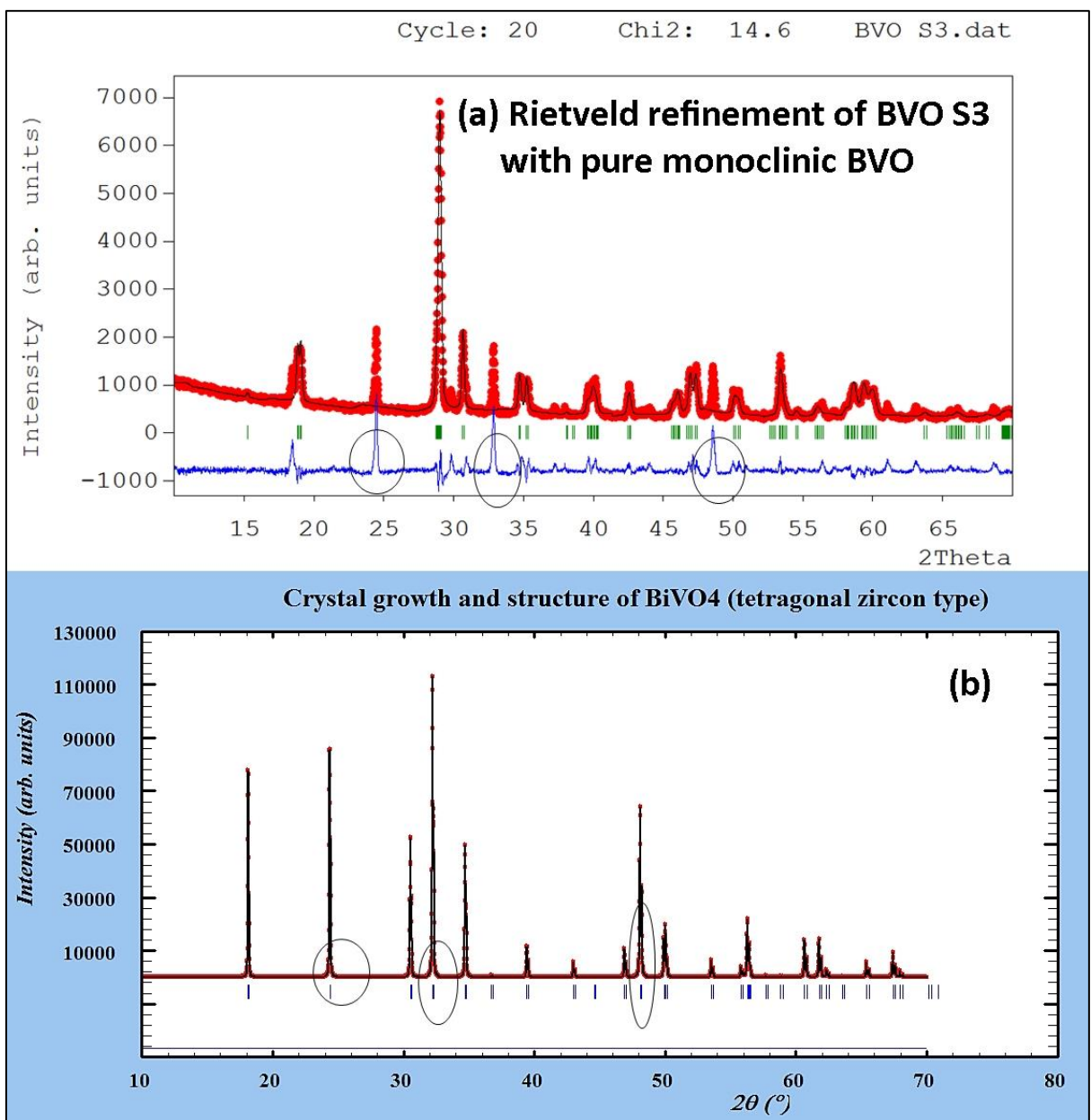


Fig 4.7: (a) Rietveld refinement of BVO S3 with pure monoclinic BVO pattern (Green circles are the unmatched Bragg reflections) (b) PXRD pattern of pure tetragonal zircon type BVO (Green circles show the unmatched reflections match with tetragonal zircon type BVO)

6. Rietveld refinement of BVO S4

Fig 4.8 (a) shows the rietveld refinement of BVO S4 with pure monoclinic BVO phase in which 10% Mn is doped at V⁵⁺ sites. **The actual PXRD pattern of BVO S4 has noisy background due to improper centrifugation after the synthesis.** For that reason, refinement for BVO S4 was quite difficult to perform and there's an indication at Bragg reflection at 17.5 – 18.5 degrees in fig 4.8 (a) which shows strong divergence. If centrifugation was done properly the splitting of the Bragg reflection at 18.5 would be clear and this splitting is a confirmation of the presence of monoclinic BVO phase in

BVO S4. No strong reflections of tetragonal BVO phases are present but improper splitting indicates the presence of a slight % of tetragonal BVO phase in the sample.

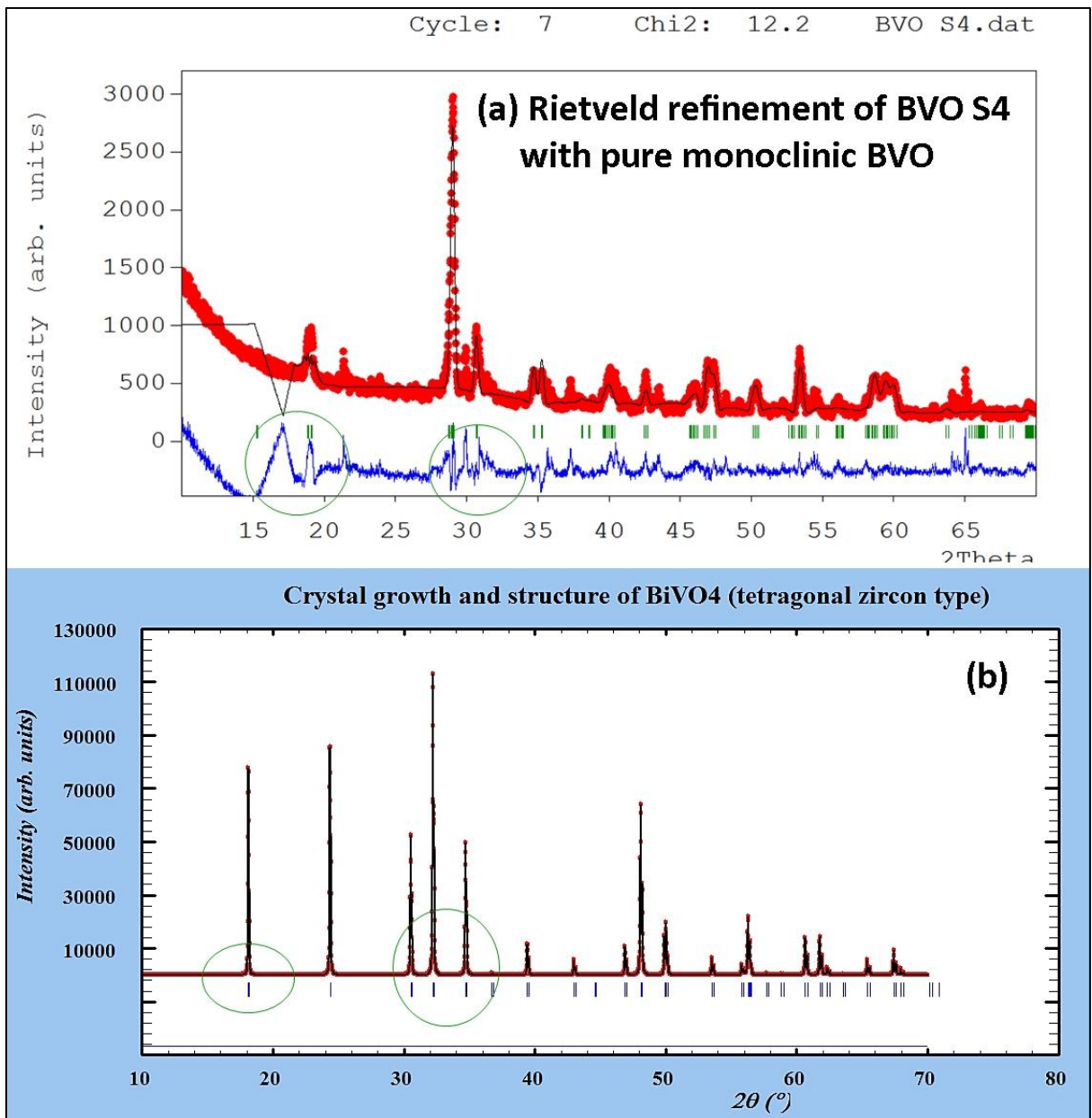


Fig 4.8: (a) Rietveld refinement of BVO S4 with pure monoclinic BVO (Green circles show unmatched Bragg reflection) (b) PXRD pattern of pure tetragonal zircon type BVO

Table 1 shows the refinement parameters of four samples. Theoretically for the best refinement, χ^2 value will be zero but it is quite impossible to reach that value in practical case. The values we have found in our analysis are nearly acceptable as we have only performed the refinement for pure monoclinic BVO phase. The difference could be reduced if tetragonal phase had been added in background during refinement. But, as the % tetragonal phase formation is not significantly dominant in any of the four samples, the cell parameters found after refinement can be taken as acceptable.

Table 3 Rietveld Refinement Outputs

Sample ID	R _p	R _{exp}	R _{wp}	R	χ^2
BVO S1	46.6	10.66	43.5	10.5	16.6
BVO S2	17.7	4.59	18.4	6.33	16
BVO S3	42.9	10.79	41.3	9.44	14.6
BVO S4	150	18.17	63.5	12.3	12.2

It is previously explained that % tetragonal phase in BVO S1 is more prominent than in any other samples. The K₂SO₄ addition has increased the cell volume in BVO S2. Since in monoclinic BVO phase lattice distortion happens, the bond lengths for the samples have been shown in table 3.

Table 4 Cell Parameters Obtained by refinement

Sample ID	Phase	Cell parameters (Å° or degrees)	Cell volume (Å°) ³	Density (g/cm ³)
BVO S1	Monoclinic	a = 5.187, b = 5.0892, c = 11.6891, $\alpha=\beta=90^\circ$, $\gamma=90.367^\circ$	308.5595	6.973
BVO S2	Monoclinic	a = 5.1799, b = 5.1046, c = 11.7003, $\alpha=\beta=90^\circ$, $\gamma=90.278^\circ$	309.3710	6.955
BVO S3	Monoclinic	a = 5.1811, b = 5.1087, c = 11.6973, $\alpha=\beta=90^\circ$, $\gamma=90.285^\circ$	309.6091	6.949
BVO S4	Monoclinic	a = 5.1843, b = 5.1062, c = 11.7704, $\alpha=\beta=90^\circ$, $\gamma=90.258^\circ$	309.7353	6.946

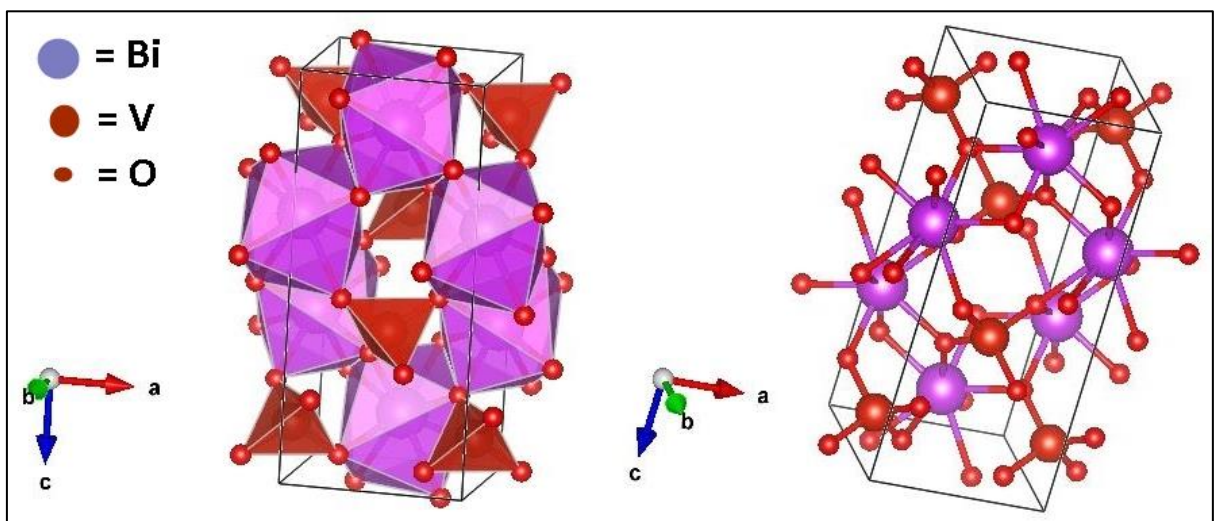


Fig 4.9: Crystal structure of pure monoclinic BVO

Table 5 Bond Lengths Obtained after Refinement

Sample ID	Dodecahedral (A°)				Tetrahedral (A°)		O1 – O2
	Bi – O1	Bi – O2	Bi – O1	Bi – O2	V – O1	V – O2	
Pure m - BVO	2.372	2.628	2.516	2.354	1.770	1.691	3.118
BVO S1	2.353	2.515	2.370	2.626	1.766	1.690	2.747
BVO S2	2.372	2.630	2.517	2.355	1.770	1.689	2.954
BVO S3	2.372	2.627	2.518	2.355	1.771	1.689	3.118
BVO S4	2.375	2.639	2.519	2.364	1.774	1.694	3.743

7. Effect of doping

For BVO S3, 10% Nd doped BVO, the cell parameters are accurately matched with pure monoclinic BVO cell parameters. The second best match has been found for BVO S2. But, for BVO S4, the most distorted lattice parameters have been obtained. The reason for longer distance between O1 – O2 is the $6s^2$ lone pair of Bi^{3+} . From the crystal structure we know that the 2p orbital of Oxygen and 6s orbital of Bismuth are antibonding in nature and so the stronger repulsion will take place between them, the larger distorted lattice structure will be found. The more repulsion takes place between Bismuth and Oxygen orbital, the easier electron transfer can be done. So, for BVO S4, lowest bandgap should be found among these four samples.

10% doping of Nd at Bismuth sites should not alter bandgap compared to the pure m – BVO and so bandgap of BVO S2 and BVO S3 should be around 2.5 eV theoretically. In our UV – Vis spectroscopy analysis we have found exactly this expected bandgap for BVO S2 and BVO S3 which will be discussed later in UV – Vis analysis section. Though atomic radius of Nd (245 pm) is higher than Bi (230 pm), for an instance it may seem replacement of Bi by Nd will create a significant distortion but it does not. The reason is Bi is well surrounded by the oxygen atoms in a dodecahedra structure. The void in that dodecahedral is quite larger for which replacement of 10% Bi by Nd should not cause a significant distortion as well as significant reduction of bandgap should not be happened theoretically. In our UV – Vis analysis, this assumption has been found correct.

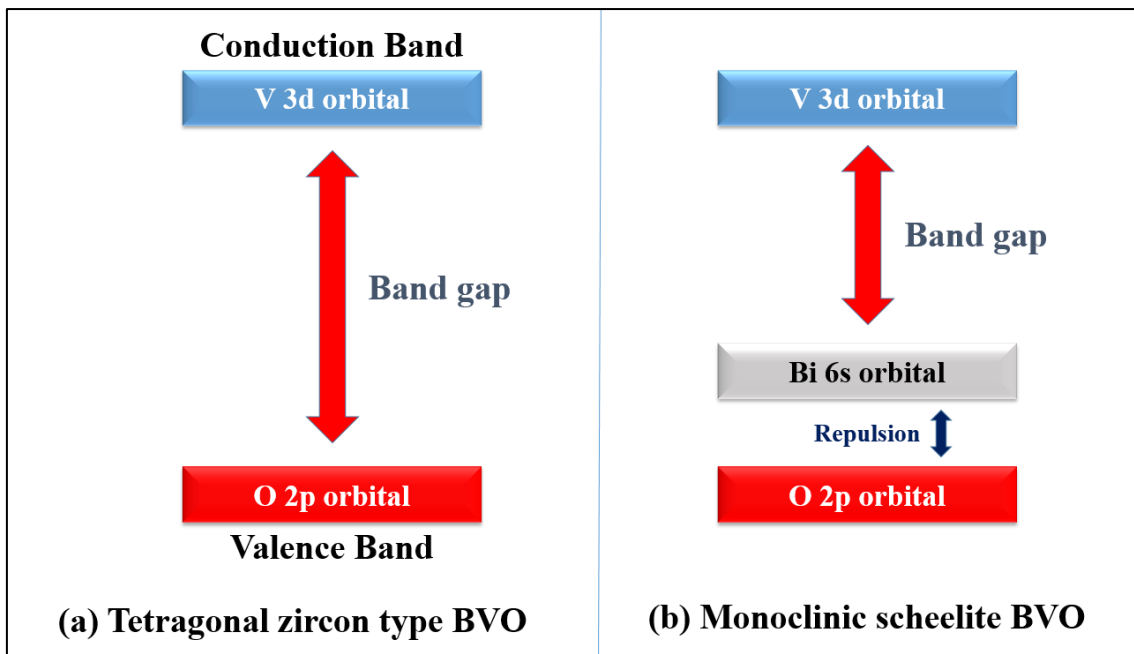


Fig 4.10: Schematic diagram explaining the bandgap reduction in m - BVO

But, on the other hand, 10% doping of Mn at V sites create a different scenario. Because both V and Mn have almost equal atomic radius (205 pm) and most importantly V is well surrounded by four oxygen atoms in a tetrahedral structure. The void occupied in tetrahedral is not larger as dodecahedra. Mn has multi valence states and for this reason the interaction between Mn and Oxygen will be higher than V – O interaction. So, O₁ – O₂ bond distance will be more stretched which will lead the rising of Bi 6s lone pair more close to the conduction band. So, theoretically band gap should be decreased with the doping of Mn at V sites. In our UV – Vis this assumption has been found correct.

3. Microstructure Study

Crystallographic structure is the visual confirmation of X – Ray Diffraction analysis of any materials. Fig 4.11 (a) shows a typical crystal of BVO with different facets which indicate the crystallographic planes.

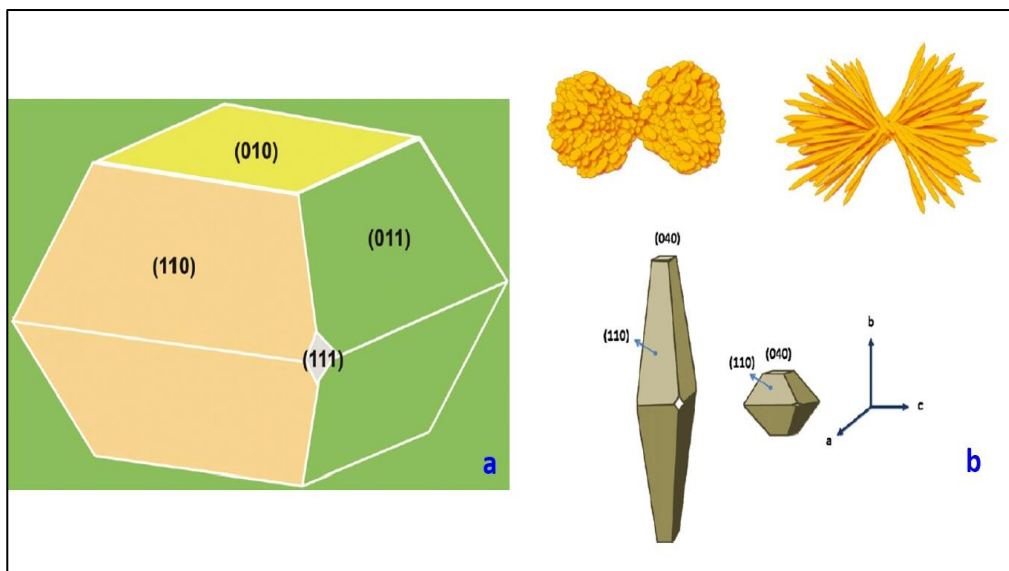


Fig 4.11: (a) Typical crystal of BiVO₄ exposed with the {010}, {110}, {011} and {111} facets (reproduced from ref 12, copyright The Royal Society of Chemistry. 2014). (b) Schematic illustration of different morphologies of BiVO₄ (reproduced from ref 13, copyright Elsevier B.V. 2011)

In BVO S1, % monoclinic BVO phase is not much dominating as in the other three samples. So, in BVO S1, irregular size and non-uniform distribution are expected. Fig 4.12 (a) confirms the irregular size and non-uniformity of the size distribution. In fig 4.12 (b) some small particles are attached with the synthesized BVO particles. Previous studies said that these are the potassium vanadate fibers which has also photocatalytic activity of its own. But the presence of potassium vanadate fibers can be confirmed in phase study as well as XRD analysis. Due to the continuous centrifugation these potassium fibers lost their fiber forms by washing away. In fig 4.13 (b) the lost shape of potassium vanadate fibers can be noticed.

The addition of potassium sulphate helps to synthesize BVO particles having uniform size and shape distribution which can be confirmed by fig 4.14 (a) & (b). Due to the absence of some crystallographic planes which are responsible for the formation of tetragonal zircon type BVO, the particles are formed as in pellet shaped and elongated in one direction.

For 10% Nd doping, the morphology of particle size and shape did not improve rather doping coarsened the particle compared to BVO S2. Needle shaped particles are formed. But for 10% Mn doping at V sites, fibrous BVO particles were formed. The fibrous nano particles will have larger surface area compared to BVO S1 & BVO S2. So, overall performance is supposed to be enhanced of BVO S4.

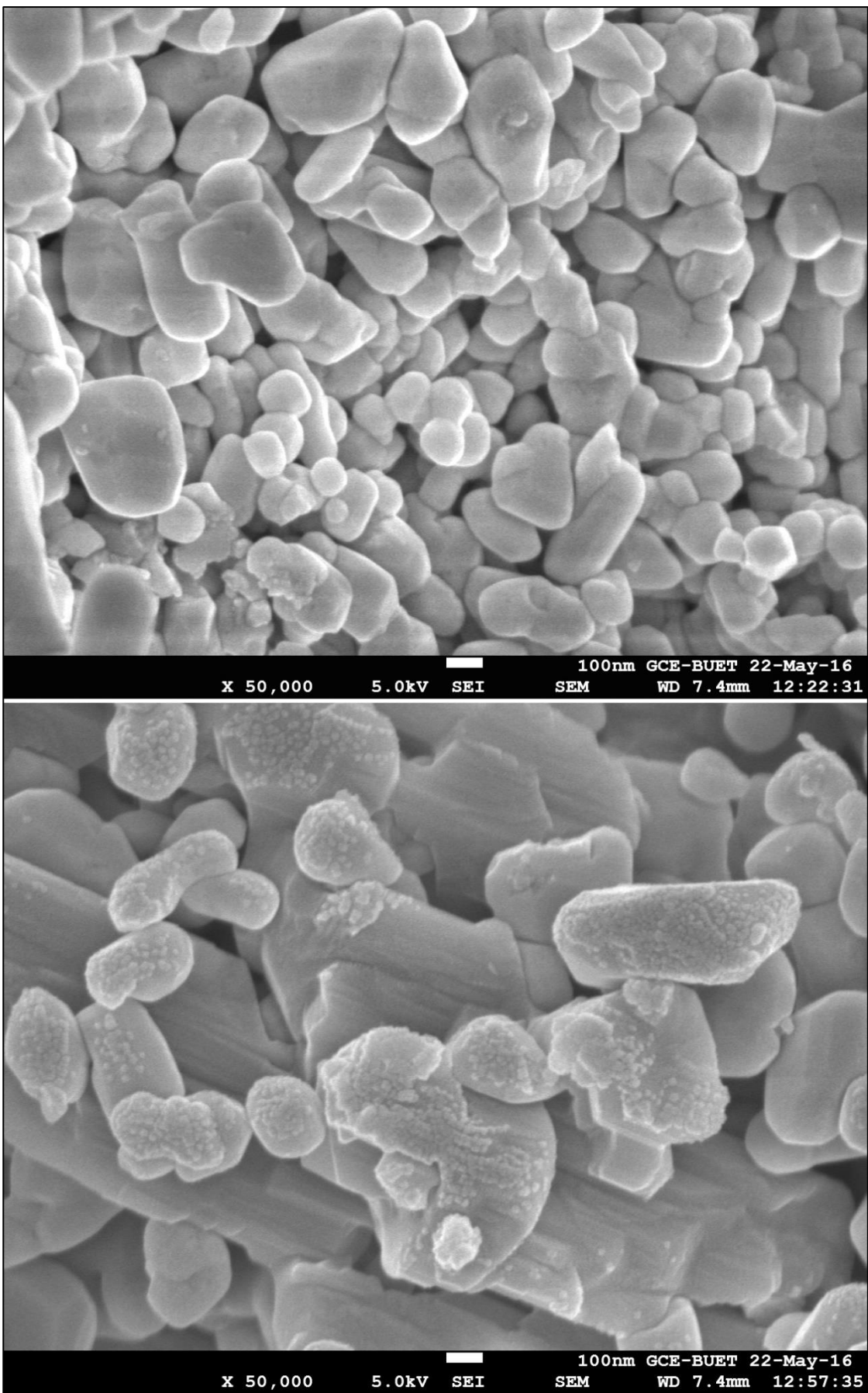


Fig 4.12: FESEM of BVO S1 in (a) & (b) x 50,000

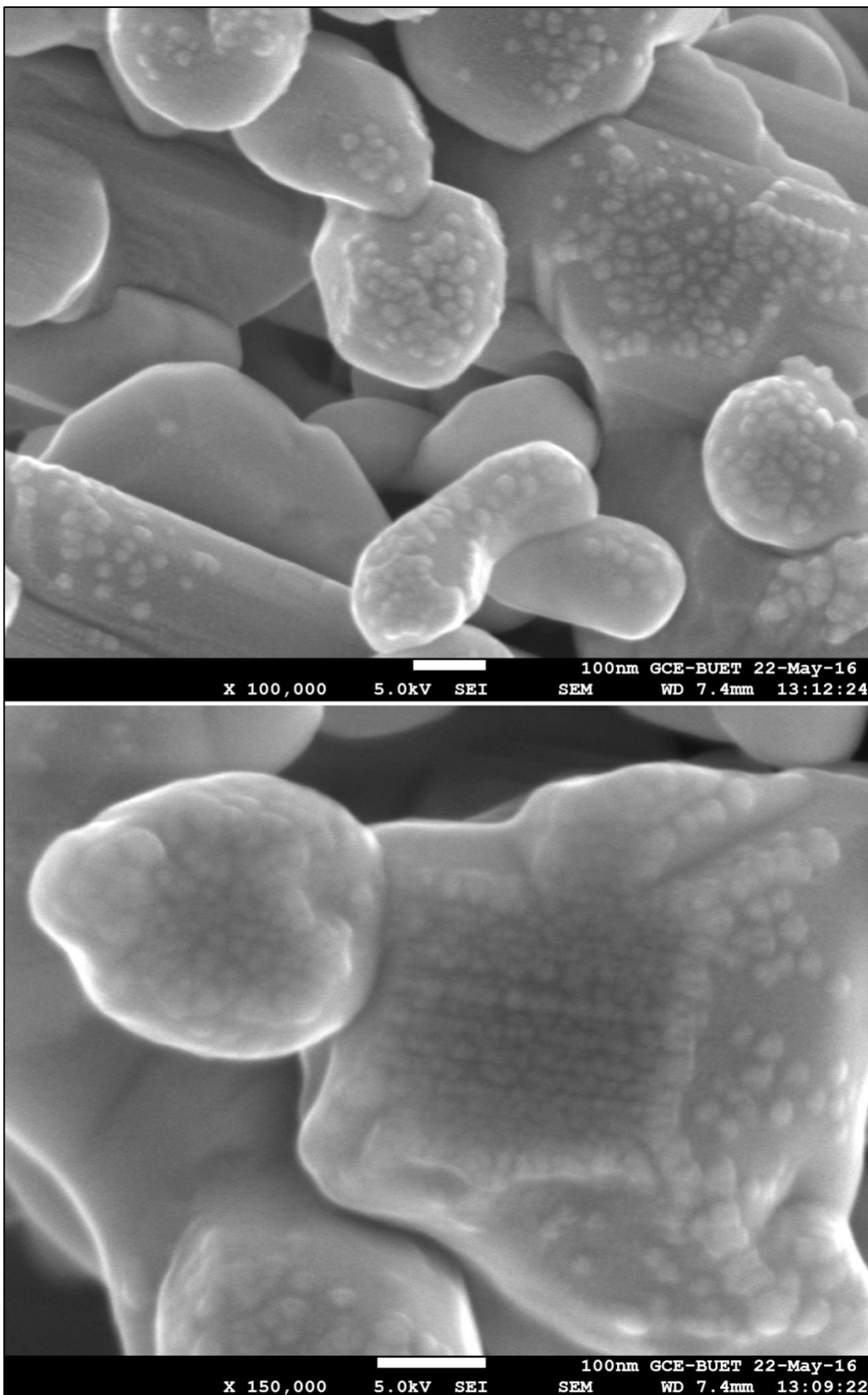
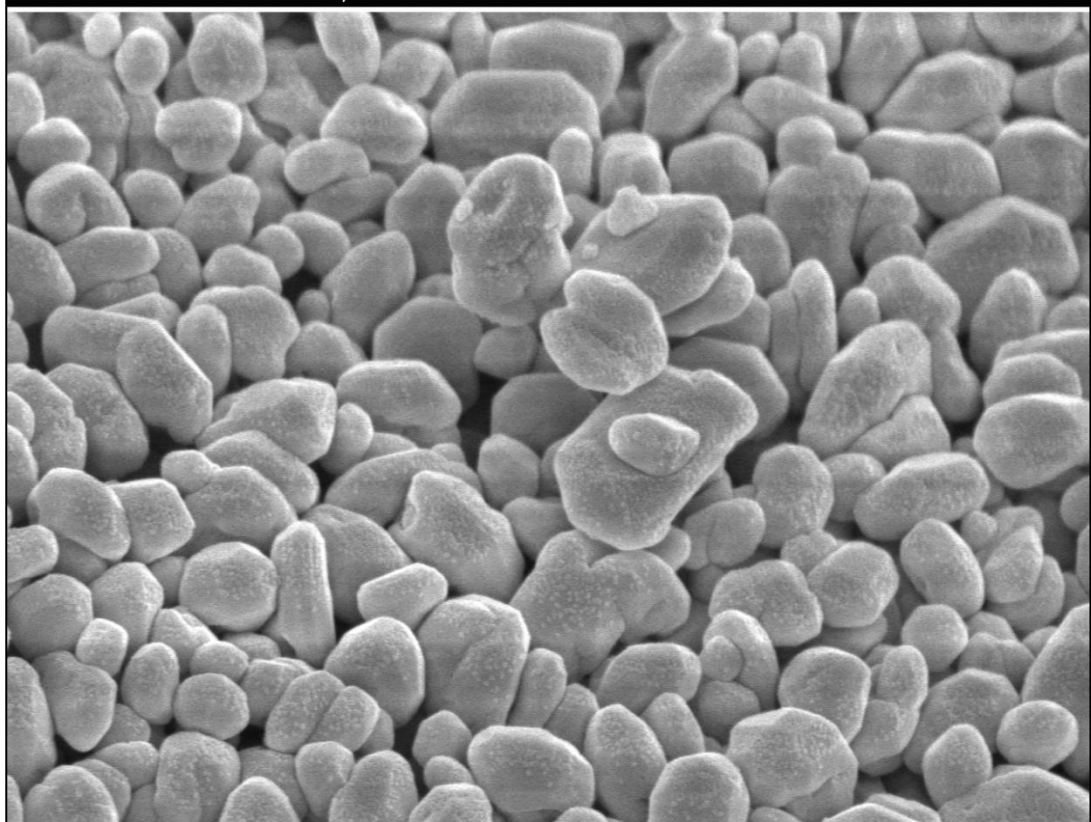


Fig 4.13: FESEM of BVO S1 in (a) $\times 100000$ & (b) $\times 150000$



100nm GCE-BUET 24-May-16
X 30,000 5.0kV SEI SEM WD 7.7mm 11:37:30



100nm GCE-BUET 24-May-16
X 30,000 5.0kV SEI SEM WD 7.6mm 11:41:57

Fig 4.14: FESEM of BVO S2 in (a) & (b) x 30,000

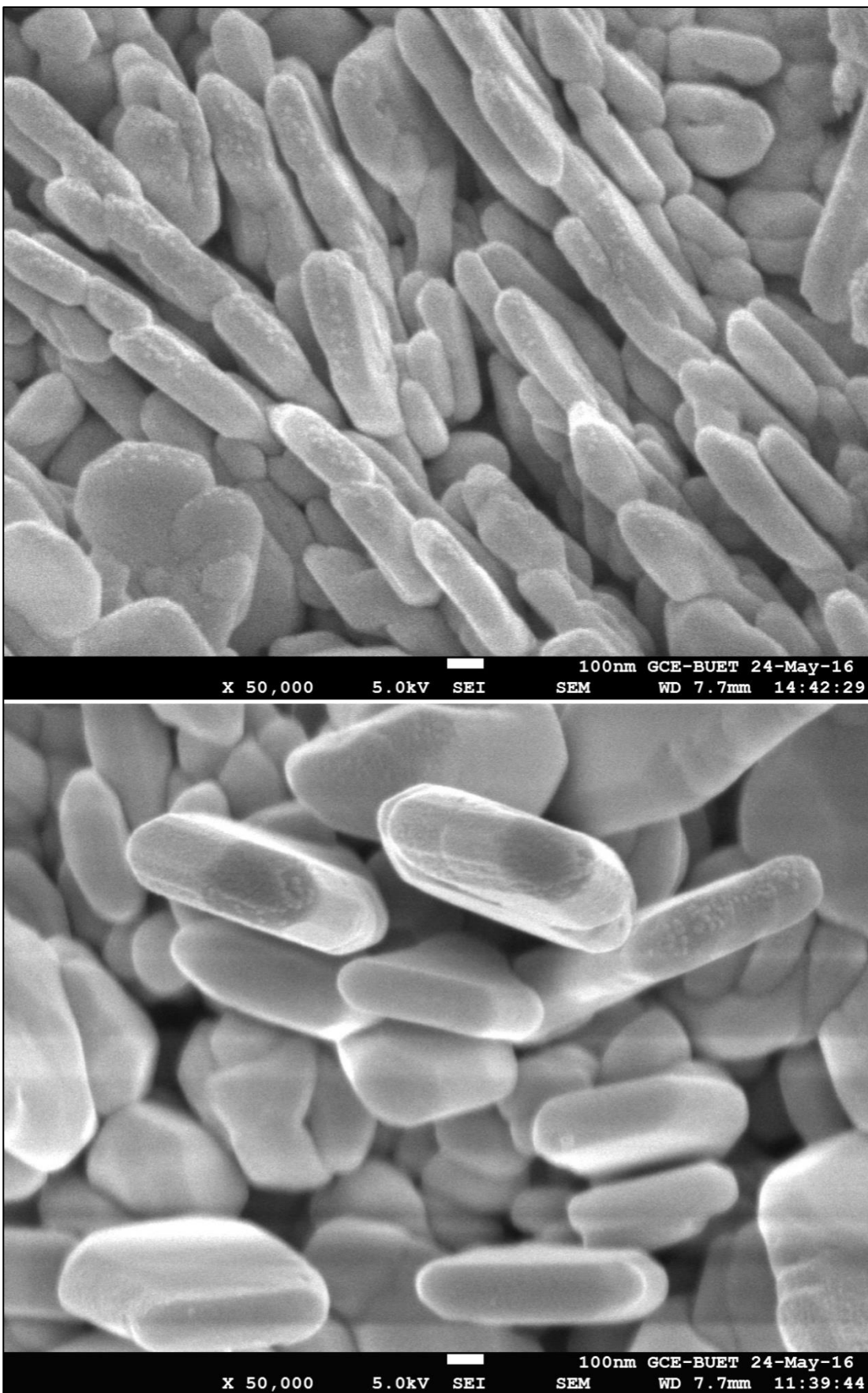


Fig 4.15: FESEM of BVO S2 in (a) & (b) x 50,000

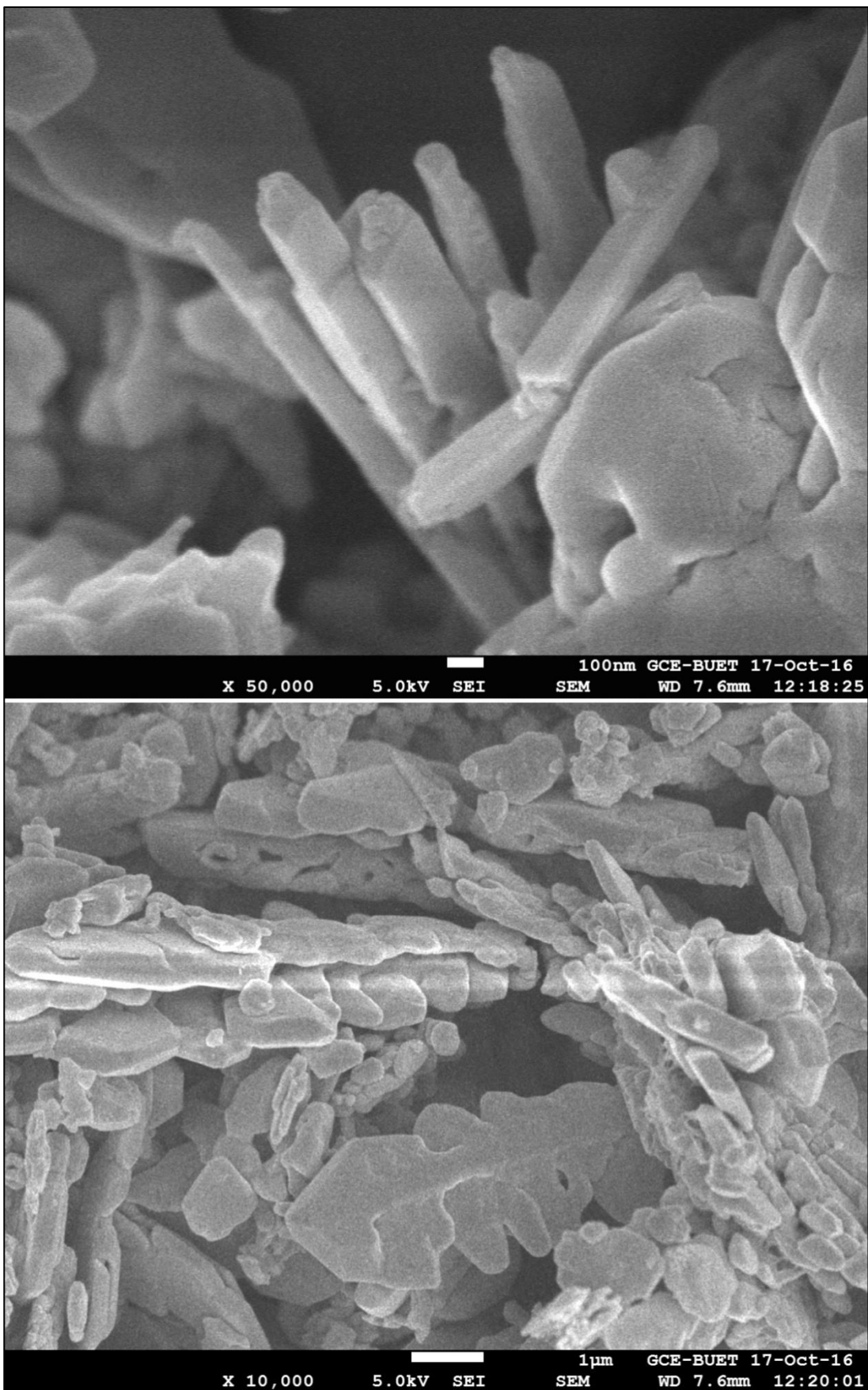


Fig 4.16: FESEM of BVO S3 in (a) x 50,000 & (b) x 10,000

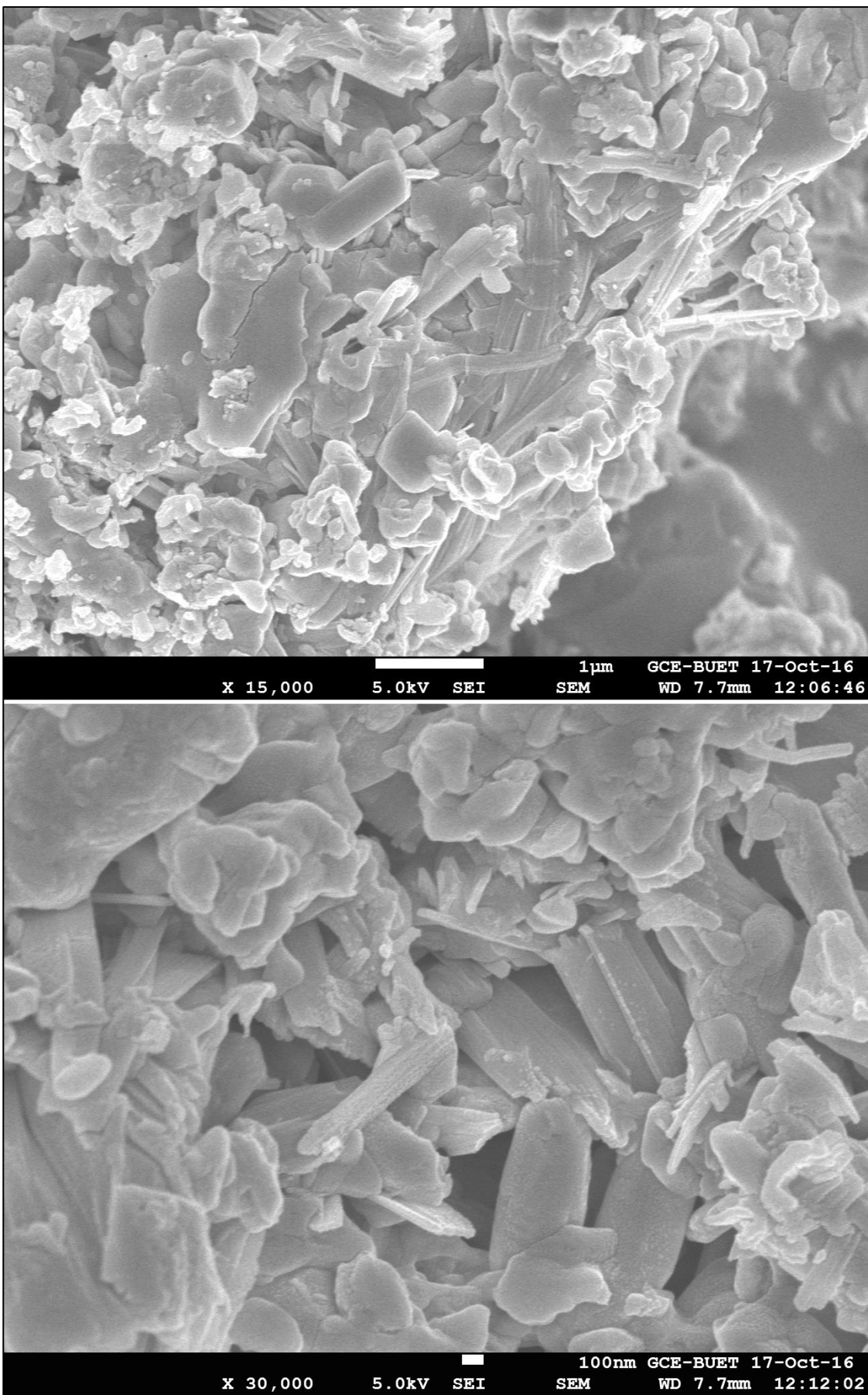


Fig 4.17: FESEM of BVO S4 in (a) x 15,000 & (b) x 30,000

4. UV – Vis Analysis:

Fig 4.18 shows the absorption vs wavelength plot of doped and undoped samples. This diffused reflectance data was converted to Kubelka-Munk function [14] given by

$$F(R) = \frac{(1-R)^2}{2R} \quad (1)$$

(Where R is the diffused reflectance value) to construct $[hvF(R)]^2$ vs photon energy (hv) plots of BiVO_4 samples fig 4.19 & 4.20.

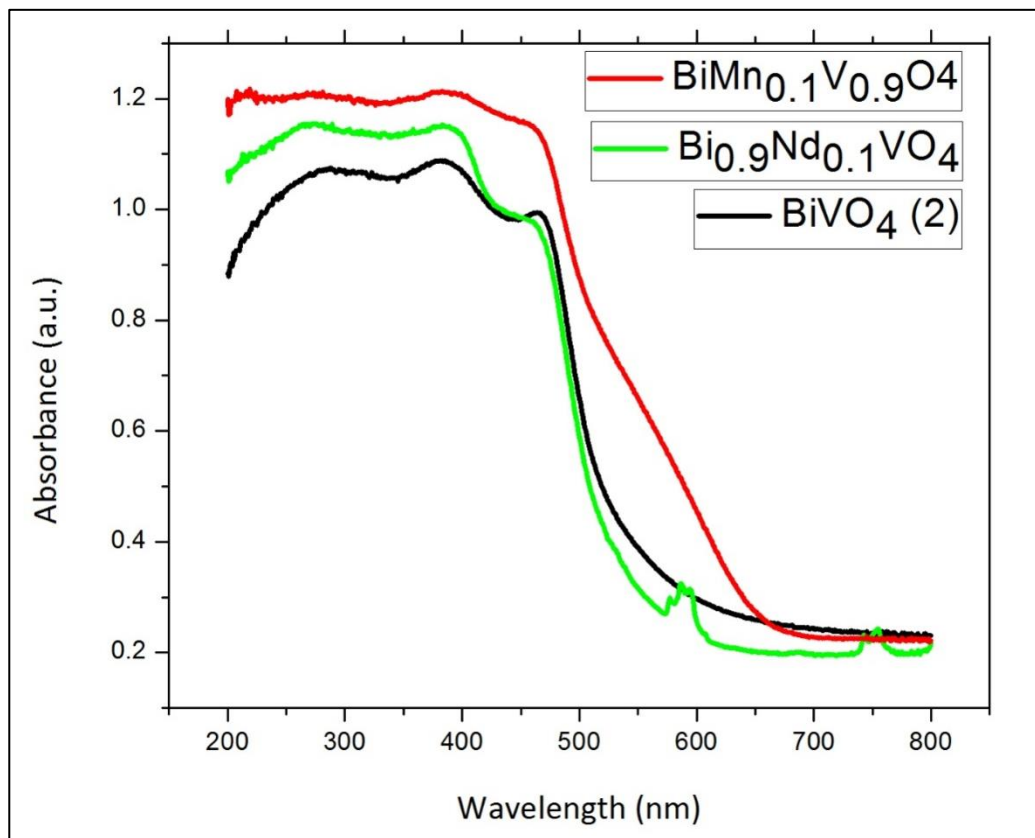


Fig 4.18: UV – Vis absorption spectra of BVO S2, BVO S3 & BVO S4

The intersection of the tangent line with $[hvF(R)]^2 = 0$ represents the optical band gap energy. Fig 4.19 and 4.20 (a) & (b) show that the band gap of sample S2, S3 and S4 are 2.47 eV, 2.5 eV and 2.44 eV respectively.

The fall of the curves within 400 – 500 nm in fig 4.18 indicates that all three synthesized particles will be active in visible range. As the phase study suggested, undoped sample BVO S2 and Nd doped sample BVO S3 have equal bandgap and it is confirmed that

doping with Nd has no effect on bandgap reduction. Rather doping at large dodecahedral void has stabilized the overall distortion in BVO and thus % monoclinic BVO has been slightly reduced and slight % of tetragonal zircon type BVO has been produced. So, it can be concluded that 10% doping of Nd at dodecahedral structure by replacing Bi is quite disappointing and doesn't change anything.

On the other hand, Mn doped sample BVO S4 has the lowest bandgap as the phase study foretold. The interaction between Mn and O plays the vital role by stretching the O1 – O2 which are differently attached with two dodecahedra. Thus the stretching of this O1 – O2 reduces the repulsion between O 2p and Bi 6s lone pair. So, Bi 6s can come forward towards V 3d state and ultimately the overall charge transfer mechanism is enhanced.

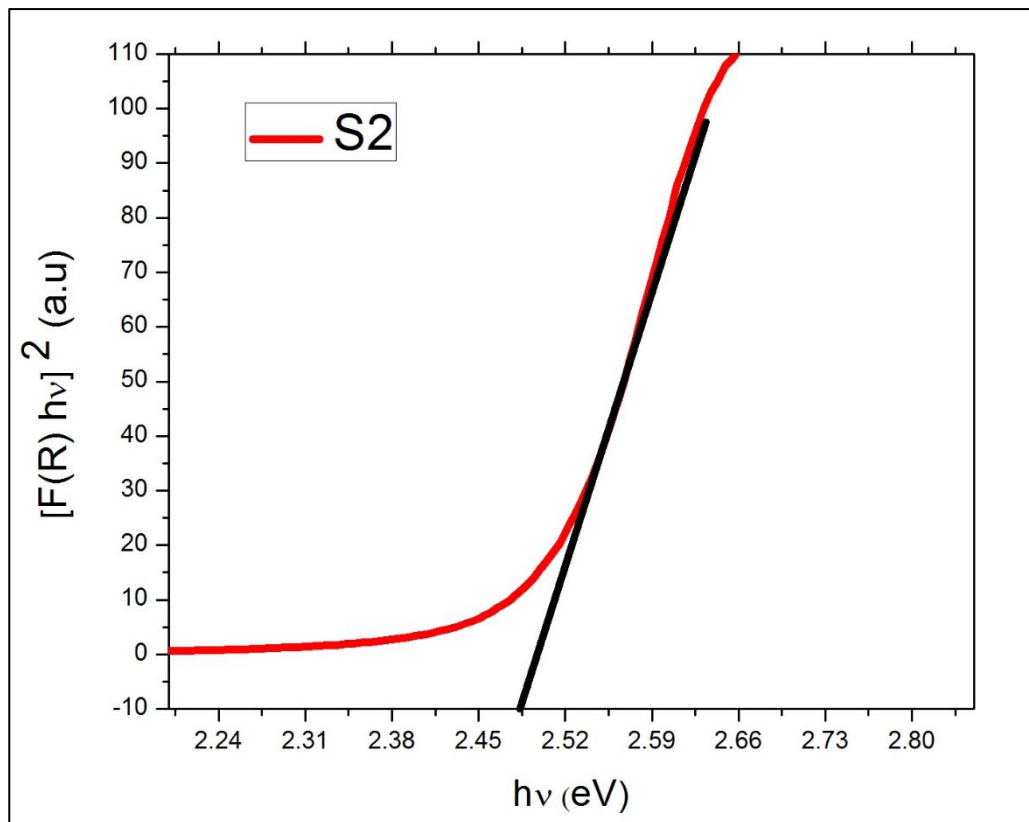


Fig 4.19: $[\text{h}\nu F(\text{R})]^2$ vs photon energy ($\text{h}\nu$) plots to calculate band gap energy of BVO S2

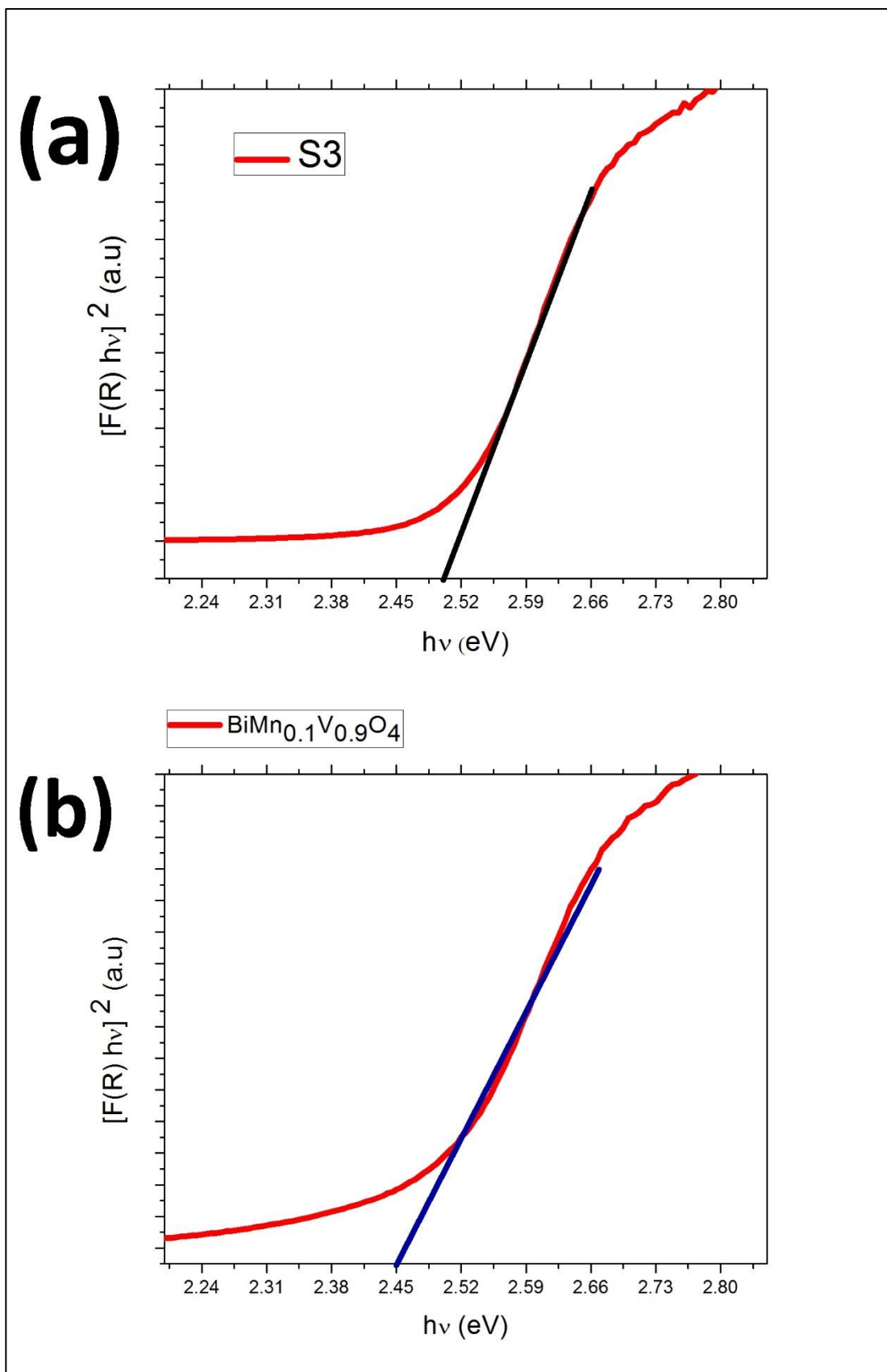


Fig 4.20: $[h\nu F(R)]^2$ vs photon energy ($h\nu$) plots to calculate band gap energy of (a) BVO S3 & (b) BVO S4

Chapter 5 Conclusions

This research work had two objectives, one is to perform a straight forward hydrothermal synthesis to produce monoclinic BiVO₄ and the other one is to investigate the effect of doping on bandgap at Bi³⁺ and V⁵⁺ sites.

In summary, we present an efficient hydrothermal route to produce highly crystalline monoclinic BiVO₄. Firstly, we selected appropriate bismuth and vanadium sources and in the next step, the particle morphology was optimized using K₂SO₄ as a shape-controlling additive in the Bi(NO₃)₃.5H₂O/V₂O₅/K₂SO₄ hydrothermal system. Generally, the use of low-cost and flexible inorganic additives as a template in nanomaterials fabrication is an attractive option for large-scale processes. In the present system, the use of K₂SO₄ considerably increased the % monoclinic phase. Later, doping effect at Bi³⁺ and V⁵⁺ sites by Nd and Mn respectively have also been studied thoroughly.

The most notable findings of this research are:

- ❖ K₂SO₄ addition increases the probability of the formation of impurity free BiVO₄ particles and also slightly increases % monoclinic BiVO₄ phase. The main reason behind this play is the presence of K⁺ ions in the solution which help the quicker formation of VO³⁻ during synthesis. The faster and more amount of VO³⁻ form, the easier of BiVO₄ formation will take place.
- ❖ 10% Nd doping at Bi³⁺ site has no better effect rather this doping suppresses the lattice distortion and helps to increase % tetragonal zircon type BiVO₄. The main reason is the location of Bi³⁺ in BiVO₄. The void in dodecahedral is larger enough to give space Nd ions without creating any kind of distortion.
- ❖ 10% Mn doping at V⁵⁺ site has significant effect on the lattice distortion and reduces the bandgap (2.44 eV) compared to undoped sample BVO S2. The Mn – O interaction plays the vital role to create a stretch between O1 – O2 which creates lattice distortion of BiVO₄.

Chapter 6 Suggestions for future work

Although a fruitful output was achieved in this thesis research yet further work is required to maximize the properties of BVO for practical uses.

Possible recommendations for further work on this topic are listed below:

- 10% doping at tetrahedral site with Mn shows very promising result by lowering the bandgap. So, extensive research on changing the % of Mn doping may give better result in future.
- Photocatalytic experiment needs to carried out to investigate the photocatalytic activities of these four samples
- Investigation of the relation between the increased % Nd doping and formation of monoclinic – tetragonal heterostructured BiVO₄ can be studied.

References:

- [1] A. Fujishima, K. Honda, *Nature* 238 (1972) 37–38.
- [2] M.R. Hoffmann, S.T. Martin, W. Choi, D.W. Bahneman, *Chem. Rev.* 95 (1995) 69–96.
- [3] M. Yan, F. Chen, J. Zhang, M. Anpo, *J. Phys. Chem. B* 109 (2005) 8673–8678.
- [4] A. Walsh, Y.F. Yan, M.N. Huda, M.M. Al-Jassim, S.H. Wei, *Chem. Mater.* 21 (2009) 547–551.
- [5] J. Tang, Z. Zou, J. Ye, *Angew. Chem. Int. Ed.* 43 (2004) 4463–4466.
- [6] L.S. Zhang, W.Z. Wang, L. Zhou, H.L. Xu, *Small* 3 (2007) 1618–1625.
- [7] X.P. Lin, F.Q. Huang, W.D. Wang, K.L. Zhang, *Appl. Catal. A* 307 (2006) 257–262.
- [8] H. Kata, H. Kobayashi, A. Kudo, *J. Phys. Chem. B* 106 (2002) 12441–12447.
- [9] S. Uchida, Y. Fujishiro, A. Watanabe, O. Ito and T. Sato, *J. Chem. Soc. Dalton Trans.* 93, 3229 (1997).
- [10] Z. Zou, J. H. Ye and H. Arakawa, *Chem. Mater.* 13, 1765 (2001).
- [11] G. K. Hyun, W. H. Dong, K. Jindo, G. K. Young and S. L. Jae, *Chem. Commun.* 12, 1077 (1999).
- [12] J. G. Yu, J. F. Xiong, B. Cheng, Y. Yu and J. B. Wang, *J. Solid State Chem.* 178, 1968 (2005).
- [13] S. Baruah, R. F. Ra⁻ que and J. Dutta, *Nano* 3, 399 (2008).
- [14] S. Anandan, Y. Ikuma, K. Kakinuma and K. Niwa, *Nano* 3, 367 (2008).
- [15] Z. Luo, K. K. Hirayama, K. Hirayama, T. Akitsu and H. Kaneko, *Nano* 3, 317 (2008).
- [16] R. Ramachandran, M. Sathiya, K. Ramesha, A. S. Prakash, G. Madras and A. K. Shukla, *J. Chem. Sci.* 123, 517 (2011).
- [17] V. R. Kumar, V. S. Prasad, P. R. S. Warriar and J. Koshy, *Nano* 6, 279 (2011).
- [18] T. Kako and J. Ye, *Mater. Trans.* 46, 2694 (2005).
- [19] A. Kudo, K. Omori, H. Kato, *J. Am. Chem. Soc.* 121 (1999) 11459–11467.
- [20] A.W. Sleight, H.Y. Chen, A. Ferretti, *Mater. Res. Bull.* 14 (1979) 1571–1581.
- [21] D.N. Ke, T.Y. Peng, L. Ma, P. Cai, P. Jiang, *Appl. Catal. A* 350 (2008) 111–117.
- [22] A. Galemebeck, O.L. Alves, *Thin Solid Films* 365 (2000) 90–93.

- [23] L. Zhou, W.Z. Wang, L.S. Zhang, H.L. Xu, W. Zhu, *J. Phys. Chem. C* 111 (2007) 13659–13664.
- [24] D.N. Ke, T.Y. Peng, L. Ma, P. Cai, K. Dai, *Inorg. Chem.* 48 (2009) 4685–4691.
- [25] Y. Park, K. J. McDonald and K.-S. Choi, *Chem. Soc. Rev.*, 2013, 42, 2321.
- [26] M. S. Prévot and K. Sivula, *J. Phys. Chem. C*, 2013, 117, 17879.
- [27] P. Bornoz, F. F. Abdi, S. D. Tilley, B. Dam, R. van de Krol, M. Graetzel and K. Sivula, *J. Phys. Chem. C*, 2014, 118, 16959.
- [28] F. F. Abdi, N. Firet and R. van de Krol, *ChemCatChem*, 2013, 5, 490.
- [29] J. K. Cooper, S. Gul, F. M. Toma, L. Chen, P.-A. Glans, J. Guo, J. W. Ager, J. Yano and I. D. Sharp, *Chem. Mater.*, 2014, 26, 5365.
- [30] K. J. McDonald and K.-S. Choi, *Energy Environ. Sci.*, 2012, 5, 8553.
- [31] Liwu Zhang, Erwin Reisner and Jeremy J. Baumberg., Al-doped ZnO inverse opal networks as efficient electron collectors in BiVO₄ photoanodes for solar water oxidation, *Energy Environ. Sci.*, 2014, 7, 1402.
- [32] Kaining Ding, Bin Chen,aYulu Li, YongfanZhangab and ZhongfangChenc, Comparative density functional theory study on the electronic and optical properties of BiMO₄ (M = V, Nb, Ta). *J. Mater. Chem. A*, 2014, 2, 8294.
- [33] Dong-Dong Qin, Ting Wang, Yu-Min Songa and Chun-Lan Tao, Reduced monoclinic BiVO₄ for improved photo electrochemical oxidation of water under visible light, DOI: 10.1039/c3dt53575d
- [34] WenjunLuo, Jiajia Wang, Xin Zhao, Zongyan Zhao, ZhaoshengLiab and ZhigangZou, Formation energy and photoelectrochemical properties of BiVO₄ after doping at Bi³⁺ or V⁵⁺ sites with higher valence metal ions, *Phys.Chem. Chem. Phys.*, 2013, 15, 1006.
- [35] Jingxiu Yang, Donge Wang, Xin Zhou and Can Li, A Theoretical Study on the Mechanism of Photocatalytic Oxygen Evolution on BiVO₄ in Aqueous Solution, *Chem. Eur. J.*, 2013, 19, 1320 – 1326.
- [36] Saimi Tokunaga, Hideki Kato, and Akihiko Kudo, Selective Preparation of Monoclinic and Tetragonal BiVO₄ with Scheelite Structure and Their Photocatalytic Properties, *Chem. Mater.*, 2001, 13, 4624-4628.
- [37] Sara Usai, Sergio Obregon, Ana Isabel Becerro and Gerardo Colon, Monoclinic–Tetragonal Heterostructured BiVO₄ by Yttrium Doping with Improved Photocatalytic Activity, dx.doi.org/10.1021/jp409170y | *J. Phys. Chem. C* 2013, 117, 24479–24484
- [38] G.P. Nagabhusana, G. Nagaraju and G. T. Chandrappa Synthesis of bismuth vanadate: its application in H₂ evolution and sunlight-driven photodegradation, DOI: 10.1039/c2ta00490a, *J. Mater. Chem. A*, 2013, 1, 388

- [39] Ying Zhou, Kathrin Vuille, Andre Heel, Benjamin Probst, Roman Kontic, Greta R. Patzke An inorganic hydrothermal route to photocatalytically active bismuth vanadate doi:10.1016/j.apcata.2009.12.031, Applied Catalysis A: General 375 (2010) 140–148.
- [40] S. Obregon, A. Caballero, G. Colon. Hydrothermal synthesis of BiVO₄: Structural and morphological influence on the photocatalytic activity, Applied Catalysis B: Environmental 117– 118 (2012) 59– 66.
- [41] A. J. E. Rettie, H. C. Lee, L. G. Marshall, J.-F. Lin, C. Capan, J. Lindemuth, J. S. McCloy, J. Zhou, A. J. Bard and C. B. Mullins, J. Am. Chem. Soc., 2013, 135, 11389.
- [42] N. Aiga, Q. Jia, K. Watanabe, A. Kudo, T. Sugimoto and Y. Matsumoto, J. Phys. Chem. C, 2013, 117, 9881.
- [43] K. P. S. Parmar, H. J. Kang, A. Bist, P. Dua, J. S. Jang and J. S. Lee, ChemSusChem, 2012, 5, 1926.
- [44] A. Nell, A. B. Getsoian, S. Werner, L. Kiwi-Minsker and A. T. Bell, Langmuir, 2014, 30, 873.
- [45] P. Kwolek, K. Pilarczyk, T. Tokarski, K. Lewandowska and K. Szacilowski, Nanoscale, 2014, 6, 2244.
- [46] G. Wang, Y. Ling, X. Lu, F. Qian, Y. Tong, J. Z. Zhang, V. Lordi, C. Rocha Leao and Y. Li, J. Phys. Chem. C, 2013, 117, 10957.
- [47] W. Luo, Z. Yang, Z. Li, J. Zhang, J. Liu, Z. Zhao, Z. Wang, S. Yan, T. Yu and Z. Zou, Energy Environ. Sci., 2011, 4, 4046.
- [48] S. K. Cho, H. S. Park, H. C. Lee, K. M. Nam and A. J. Bard, J. Phys. Chem. C, 2013, 117, 23048.
- [49] W. Luo, Z. Li, T. Yu and Z. Zou, J. Phys. Chem. C, 2012, 116, 5076.
- [50] W. J. Jo, J.-W. Jang, K.-j. Kong, H. J. Kang, J. Y. Kim, H. Jun, K. P. S. Parmar and J. S. Lee, Angew. Chem., Int. Ed., 2012, 51, 3147.
- [51] S. Obregón and G. Colón, Appl. Catal., B, 2014, 152–153, 328.
- [52] S. Huang, N. Zhu, Z. Lou, L. Gu, C. Miao, H. Yuan and A. Shan, Nanoscale, 2014, 6, 1362. [53] G. Liu, J. C. Yu, G. Q. Lu and H.-M. Cheng, Chem. Commun., 2011, 47, 6763.
- [54] G. Xi and J. Ye, Chem. Commun., 2010, 46, 1893.
- [55] D. Wang, H. Jiang, X. Zong, Q. Xu, Y. Ma, G. Li and C. Li, Chem. – Eur. J., 2011, 17, 1275.
- [56] J. Yang, D. Wang, X. Zhou and C. Li, Chem. – Eur. J., 2013, 19, 1320.
- [57] J. Pan, G. Liu, G. Q. Lu and H.-M. Cheng, Angew. Chem., Int. Ed., 2011, 50, 2133.
- [58] R. Li, F. Zhang, D. Wang, J. Yang, M. Li, J. Zhu, X. Zhou, H. Han and C. Li, Nat. Commun., 2013, 4, 1432.

- [59] R. Li, H. Han, F. Zhang, D. Wang and C. Li, *Energy Environ. Sci.*, 2014, 7, 1369.
- [60] H. Tong, S. Ouyang, Y. Bi, N. Umezawa, M. Oshikiri and J. Ye, *Adv. Mater.*, 2012, 24, 229.
- [61] H. L. Zhou, Y. Q. Qu, T. Zeid and X. F. Duan, *Energy Environ. Sci.*, 2012, 5, 6732.
- [62] Y. Ma, X. Wang, Y. Jia, X. Chen, H. Han and C. Li, *Chem. Rev.*, 2014, 114, 9987.
- [63] A. Kubacka, M. Fernandez-Garcia and G. Colon, *Chem. Rev.*, 2011, 112, 1555.
- [64] S.-i. Eda, M. Fujishima and H. Tada, *Appl. Catal., B*, 2012, 125, 288.
- [65] H. He, S. P. Berglund, A. J. E. Rettie, W. D. Chemelewski, P. Xiao, Y. Zhang and C. B. Mullins, *J. Mater. Chem. A*, 2014, 2, 9371.
- [66] W. Wang, Y. Yu, T. An, G. Li, H. Y. Yip, J. C. Yu and P. K. Wong, *Environ. Sci. Technol.*, 2012, 46, 4599.
- [67] Y. Sun, Y. Xie, C. Wu, S. Zhang and S. Jiang, *Nano Res.*, 2010, 3, 620.
- [68] X. Chen, J. Liu, H. Wang, Y. Ding, Y. Sun and H. Yan, *J. Mater. Chem. A*, 2013, 1, 877. [69] J. Sun, G. Chen, J. Wu, H. Dong and G. Xiong, *Appl. Catal., B*, 2013, 132, 304.
- [70] Y. Sun, C. Wu, R. Long, Y. Cui, S. Zhang and Y. Xie, *Chem. Commun.*, 2009, 4542. 44 Y. Zhao, Y. Xie, X. Zhu, S. Yan and S. Wang, *Chem. – Eur. J.*, 2008, 14, 1601.
- [71] G. Li, D. Zhang and J. C. Yu, *Chem. Mater.*, 2008, 20, 3983.
- [72] Y. Park, K. J. McDonald and K.-S. Choi, *Chem. Soc. Rev.*, 2013, 42, 2321.
- [73] F. F. Abdi, N. Firet and R. van de Krol, *ChemCatChem*, 2013, 5, 490.
- [74] K. J. McDonald and K.-S. Choi, *Energy Environ. Sci.*, 2012, 5, 8553.
- [75] E. S. Kwak, W. Lee, N.-G. Park, J. Kim and H. Lee, *Adv. Funct. Mater.*, 2009, 19, 1093.
- [76] M. Zhou, H. B. Wu, J. Bao, L. Liang, X. W. Lou and Y. Xie, *Angew. Chem., Int. Ed.*, 2013, 52, 8579.
- [77] G. Wang, Y. Ling, X. Lu, F. Qian, Y. Tong, J. Z. Zhang, V. Lordi, C. Rocha Leao and Y. Li, *J. Phys. Chem. C*, 2013, 117, 10957.
- [78] J. Sun, G. Chen, J. Wu, H. Dong and G. Xiong, *Appl. Catal., B*, 2013, 132, 304.
- [79] Y. Zhao, Y. Xie, X. Zhu, S. Yan and S. Wang, *Chem. – Eur. J.*, 2008, 14, 1601.
- [80] M. Zhou, H. B. Wu, J. Bao, L. Liang, X. W. Lou and Y. Xie, *Angew. Chem., Int. Ed.*, 2013, 52, 8579.
- [81] G. Li, D. Zhang and J. C. Yu, *Chem. Mater.*, 2008, 20, 3983.
- [82] Crystallographic Open Database, <http://www.crystallography.net/cod/search.html>
[Last Accessed 13 Feb, 2017]

